THE DISSERTATION COMMITTEE FOR ZEXI LIANG CERTIFIES THAT THIS IS THE APPROVED VERSION OF THE FOLLOWING DISSERTATION:

LIGHT MODULATION OF ELECTRIC FIELD DRIVEN SEMICONDUCTOR MICROMOTORS

Committee:

Donglei Fan, Supervisor

Arumugam Manthiram

Edward Yu

Ray Chen

LIGHT MODULATION OF ELECTRIC FIELD DRIVEN SEMICONDUCTOR MICROMOTORS

by

ZEXI LIANG

DISSERTATION

Presented to the Faculty of the Graduate School of

The University of Texas at Austin

in Partial Fulfillment

of the Requirements

for the Degree of

DOCTOR OF PHILOSOPHY

THE UNIVERSITY OF TEXAS AT AUSTIN

AUGUST 2021

Acknowledgements

Completing this thesis would be a mission impossible without many people's help, support, and contribution. First of all, I would like to thank my advisor, Professor Donglei Fan, for her support, advice, and guidance over the past six years. The confidence she showed in me encouraged me and strengthened my faith to pursue a career in academia. She sets an excellent example to me about the key characters that a researcher should have: perseverance, patience, curiosity, and passion. Her mentoring affects me from many perspectives. In addition, I want to acknowledge the contributions of my dissertation committee members: Professor Arumugam Manthiram, Professor Edward Yu, and Professor Ray Chen. I am lucky to have their advice based on their expertise from different fields. I am also very grateful for their support for my career development.

My colleagues and friends have always been very supportive and understanding. To my colleagues: Dr. Chao Liu, Dr. Jianhe Guo, Dr. Kwanoh Kim, Dr. Weigu Li, Yun Huang, Daniel Teal, Hyungmok Joh, Huaizhi Li, Yifei Liu, and Mohammad Alsoraya – I have learned so much from you, and I enjoyed the time working with you in such a great atmosphere. Special thanks to my friend Nan Xue for the companionship over thirteen years. I would also like to thank many of my volleyball teammates over the years. We shared so many unforgettable moments on the court including three times of championship.

Finally, I would like to thank my family for their constant support. My parents and grandparents always have faith in me, and they are the source of my strength. I also have to mention my previous teammate Rui, who now becomes my fiancée. I am lucky enough to meet her here in UT, and we together have been through all the highs and lows.

ABSTRACT

LIGHT MODULATION OF ELECTRIC FIELD DRIVEN SEMICONDUCTOR MICROMOTORS

Zexi Liang, Ph.D.

The University of Texas at Austin, 2021

Supervisor: Donglei Fan

The future micro/nanorobots require high degrees of freedom in motion control to perform complex tasks by individuals or by a swarm. It remains a great challenge to control the motions of an individual nanomachine amidst many, to switch the operation modes facilely, and it is even more difficult to actuate several components of a nanomachine coordinately for purposed actions. This high degree of versatility is essential for the future micro/nanorobots and requires investigation of innovative actuation mechanisms. In this dissertation, we report our recent finding about a new approach combining two types of stimulation to achieve such goal. The micromotors being studied are made of semiconductor silicon nanowires. Mechanical motion of the motors is driven by several types of AC electric field. Meanwhile, the electrical property of the nanowires can be locally and instantaneously modulated by visible light illumination in a reversible manner. We demonstrate that visible light is able to change the electric polarization of semiconductor nanowires under AC electric field, and reflected by the dramatic change of mechanical motions with very rich configurations. Under a rotating electric field, the rotation speed of semiconductor Si nanowires in electric fields can instantly increase,

decrease, and even reverse the orientation by light illumination in the visible to infrared regime at various AC E-field frequencies. Under a linear AC electric field, instantaneous change of alignment direction and speed of semiconductor nanowires is observed under visible-light exposure. With theoretical analysis and simulation, the working principle can be attributed to the optically tuned imaginary-part (out-phase) and real-part (in-phase) electrical polarization of a semiconductor nanowire in aqueous suspension. Based on the understanding of this system, we further propose a new approach to control the semiconductor micromotor via light tunable dielectrophoresis. Localized control of collective behavior in a highly density silicon nanowire suspension is also investigated. Finally, we demonstrated how to utilize the mechanical motion at microscale for practical application of biosensing.

Table of Contents

List of Tables

List of Figures

Chapter 1: Introduction of Micro/Nanorobotics

The concept of miniaturizing surgical machines into ultrasmall counterparts that can be swallowed for medical treatment was envisioned by Richard Feynman in his seminal lecture "There's Plenty of Room at the Bottom" in 1959. However, fabricating and operating robots with miniatured size and multifunction are not simply a job to scale back the counterpart of a macroscale robots to microscale with the same design. A huge barrier hinders the realization of such micro/nanomachines from both aspects of fundamentals and methodology. New set of technology of fabrication, manipulation, and energy supply is in demand because of the very different fundamental physics governing the motion in micro/nanoscale. Until recent decades, we have witnessed the rapid development of ultrasmall motors and machines from molecular to micrometer scales. Progress has been made in all aspects, including propulsion mechanisms, fabrication-assembly strategies, performance optimization, and applications. However, these significant advances have not resulted in a breakthrough that has allowed us to miniaturize directly complex macroscopic machines. This task remains challenging owing to the small size and sophisticated design of traditional machines. Rather, myriad ultrasmall machines that mirror their macroscopic counterpart have been created by exploring the distinct physics and chemistry at small scales, which dominate interaction and locomotion of all small objects with surroundings. In the following, we discuss the challenges remaining, and introduce an array of integrated powering schemes utilized by various ultrasmall motors that exist in nature ubiquitously or are made artificially.

1.1. Challenges in the Manipulation of Micromotors

Energy efficiency, also termed as thermodynamic efficiency, is defined as the ratio between the mechanical work done by the machine (related to the certain task) against the total energy input from the power source. The thermodynamic efficiency of motors greatly depends on their working principles. For a heat engine, the second law of thermodynamics sets the upper limit of efficiency theoretically. A state-of-the-art internal combustion engine can barely reach 50% of energy efficiency. While an electric motor can be as efficient as 98%. For micromotors, the energy efficiency varies a lot from as low as the order of 10^{-13} to as high as almost unity depending on the working mechanisms and operating conditions. It is hard to imagine how a motor can be useful with efficiency of 10^{-13} at macroscale. However, it is a different story when the motor size is extremely small. The energy consumption to move a small object is also greatly reduced as the dimension shrinks. Thus, even a very small amount of energy input can generate considerable mechanical outcomes at microscale. Meanwhile, the miniaturization also limits the amount of energy that can be harvested from the power sources. Traditional tethered robots can have unlimited power supply, and untethered robots usually contain portable energy storage system, i.e. batteries, or wirelessly powered by electromagnetic field. Nonetheless, neither of the above-mentioned approaches can be applied to power small motors of micrometer size or even smaller. Alternative approaches of powering small machines have been discovered from the small motors that already existed in nature for billions of years, as well as newly invented by scientists in the past few decades.

Another challenge remains at micro/nanoscale comes from the interaction from surrounding liquid medium. Specifically, as the size of machines miniaturized into micrometers, the surrounding medium becomes sticky that viscous force gradually dominates over inertial and gravitational forces. Reynolds number is the dimensionless

quantity representing that ratio of inertial forces to viscous forces defined as $\mathrm{Re} = \frac{\rho u l}{\mu}$, where ρ is the density of the fluid, u is the flow speed, l is the characteristic dimension of the system, and μ is the dynamic viscosity of the liquid. For a man swimming in the pool, the Reynolds number is around 10^4, while for bacteria swimming in water, the Reynolds number is around 10^{-4} to 10^{-5}. For machines that we are going to discuss, they will operate in a similar scenario as that of swimming bacteria with extremely low Reynolds number, and as a result, a series of hydrodynamic features should be taken into consideration. For soft actuators operating in low Reynolds number regime at micro/nanoscale, we want to emphasize again that the viscous forces dominate over inertia and gravity. For example, moving a cargo at macroscale requires that the actuator is powerful enough to overcome the gravity and frictions, if the actuator has insufficient work density, it will become a mission impossible. However, as for the same mission at low Reynolds numbers and small scales, the major load turns into viscous forces, which is a function of velocity. Even a weak actuator can still accomplish the mission of cargo transport at the cost of longer time consumption. The mode of thinking in developing soft actuators for micro/nanorobotics may need to be adjusted according to the feature of low Reynolds number hydrodynamics.

Brownian motion is another influential phenomenon that becomes vital at microscale. It refers to the random motion of a particles suspended in a liquid medium as a result of the collision between particle and molecules from surrounding medium. The phenomenon is universal but only becomes prominent when the particle size is small, and for extremely small particles that is close to the size of surrounding molecules, the Brownian motion can be furious. Thus, smaller the machine, stronger the Brownian motion it will go through. From the perspective of motion control, Brownian is harmful because of the randomized disturbance in both position and orientation. Strategies of steering and

guiding the propulsion of micromotors has been developed in order to counter the disturbance. From energy perspective, however, Brownian motion is the result of thermal energy, and it is of great importance in most physical, chemical and biological phenomena of energy conversion from molecular level to microscopic level or even larger scale.

1.2. Types of Micro/Nano and Molecular Motors

In the following, we will briefly introduce various approaches of powering small machines in a sequence from small to large (molecular to microscale), from biological to artificial, and from the manner of self-propelled to externally manipulated.

1.2.1. Motor Proteins

Nature had created extremely small machines that were highly efficient before the emergence of human beings on Earth. Motor proteins are molecular motors that convert chemical energy into mechanical energy to accomplish essential biological functions, including transporting cargos and generating mechanical propulsion.[1] They are essential to life and can be found in all organisms.[2-4] Below, we examine the powering mechanisms of two representative molecular motors, *i.e.*, the kinesin-1and the bacteria flagellar that can transport and rotate, respectively.

Kinesin-1 motors belong to a family of microtubular protein motors. They are powered by adenosine-triphosphate (ATP) hydrolysis to support intracellular transport processes along microtubule cytoskeletons in cells.[2,5] A kinesin walks forward along the microtubules in a hand-over-hand stepping with a constant step size of 8 nm per ATP

hydrolysis.[6-8] The stall force is ~6 pN, the maximum speed with an adequate ATP supply is ~800 nm s^{-1}, and the efficiency of energy conversion can reach 50%.[2,9]

Bacteria flagellar motors are a type of molecular machine that can reversibly rotate helical filaments to propel the locomotion of bacteria cells.[4] The motors operate by harnessing free energy released from ions transported across cytoplasmic membranes with a downhill electrochemical gradient. They can rotate up to a speed of ~300 r.p.s. and 1700 r.p.s. when driven by a gradient of hydrogen and sodium ions, respectively.[10] The energy-conversion efficiency is estimated to be near unity, *i.e.*, ~ 90%.[11]

1.2.2. Artificial Molecular Motors

Over the last few decades, numerous organic molecular motors have been synthetized, either by learning from nature or by mimicking simple macroscopic machines.[12-15] In 2016, the Nobel Prize in Chemistry was awarded to Jean-Pierre Sauvage, Sir J. Fraser Stoddart, and Bernard L. Feringa for their original contributions to artificial molecular machines. Comprehensive reviews have been given by the main contributors. Here, a few representative works are selected for discussion. Stoddart *et al.* reported a rotaxane molecular shuttle made of macrocycle molecules threaded in an axle molecular track that can operate between two binding sites with equivalent distribution possibilities. It is the energy from thermal fluctuation that drives the mechanical transition.[16] Later, the transition can select a preferred binding end with an external stimulus, such as pH.[17] The first rotary synthetic molecular motor was reported by Feringa *et al.* in 1999; it could carry out cyclic unidirectional rotation by energy from UV irradiation.[18] The motor is made of the overcrowded alkene with two identical groups connected by a carbon-carbon double bond. A 360° rotation can be accomplished by transforming the molecule into four

different isomers sequentially. This light-fueled rotary motor has a quantum efficiency of ~2%, limited by the cis-trans-photoisomerization step.[19]

1.2.3. Biological and Bioinspired Micro/Nanopropellers

In the range of micro/nanometers, self-propelling motors/machines also prevail in nature. Biological motors, such as flagella and motile cilia, are essential in locomotion of microorganisms to seek for food and light.[20,21] The directional propulsion of microorganisms arises from the interaction of the mechanical motion of the biological propellers with their surrounding medium. Two actuation modes are commonly observed, *i.e.*, corkscrew rotation and flexible filament beating.

E. coli bacterial cells with a dimension of several micrometers in length and 0.5 μm in diameter are widely found in natural water. An E-coli cell's propeller is made of several helical flagellum bundles (usually made of four) attached to flagellar motors that rotate counterclockwise and drive the helical bundle into corkscrew rotation. The corkscrew rotation interacts intimately with the surrounding suspension due to viscous drag, resulting in the conversion of rotary motion into linear propulsion of the cells. Both experimental and theoretical studies indicate that the efficiency, defined by the ratio between the net energy used for propulsion and the total energy input from the chemical conversion, is around 2%. This relatively low efficiency can be attributed to the dissipation due to the viscous force on both the rotating filament bundles and the cell.[22-24] The natural corkscrew structures and powering mechanism inspired the creation of several exquisite artificial helical micro/nanopropellers with defined structures and compositions on a large scale.[25,26] In a classical example, to mimic the swimming manner of the bacterial flagella, a ferromagnetic segment is integrated as a tiny handle that can rotate a helical structure

around its long axis by using energy from a uniform rotating magnetic field. The speed is up to hundreds of rounds per second. Catalytic reactions were also introduced to drive a helical structure that can spin and transport.[27]

Planar beating of flagella is another useful propulsion strategy adopted by spermatozoa and many other Eukaryotes.[28] The beating of the flexible flagellar generates a non-reciprocal motion that propels the linked head forward. The propulsion mechanism has been systematically studied,[29-32] and further has inspired the design of several innovative artificial motors made of flexible bodies powered by harnessing energy from external magnetic, optical, and acoustic fields. The propulsion efficiency resides at around 1% or less.[33]

1.2.4. Powering Micro/Nanoswimmers by Designing Broken Symmetry

At the micro/nanoscale, physical principles that govern a moving object differ from those in the macroscopic world. When an ultrasmall object swims in water, the viscous drag overwhelms its inertia, which can be shown by the Reynolds number (Re). For a bacteria cell and a similar-sized artificial propeller, the Reynolds number is at around 10^{-4} to 10^{-5}, 8 to 9 orders of magnitude lower than that of a human swimming in water. It has been shown that in such an extremely-low-Reynolds-number region, no object can make any net movement in a Newtonian medium if exerting a time-symmetric propulsion (scallop theorem).[34] A net propulsion at a low-Reynolds-number region requires broken symmetry. With this understanding, a series of innovative artificial micro/nanoscale motors have been designed and sculptured by breaking their symmetries in physical fields or chemical reactions, or exploiting asymmetrical properties of their suspension medium.[35,36]

Elegant examples have been demonstrated by breaking the symmetry of ionic distribution in the vicinity of a micro/nanomotor. A well-known work was reported on a Pt/Au micromotor, which can propel in a hydroperoxide (H_2O_2) solution by the electric field generated from different ions produced on the respective Pt and Au segments in the catalytic reaction. This working mechanism is the so-called self-electrophoresis that has received immense interest owing to its essential role in converting chemical energy into mechanical propulsion in an artificial system.[37,38] However, the efficiency is usually low, on the order of $10^{-8}\sim10^{-9}$. The majority of the chemical energy is dissipated by heat, side reactions, viscous drag, and liquid flows induced in the reaction.[39]

Artificial micro/nanomotors also propel by the so-called self-diffusiophoresis due to the directional flows from asymmetric distribution of chemical species, either ionic or neutron.[40-42] The detailed mechanism can be ascribed to electrophoretic interaction, chemiphoresis pressure,[42,43] and steric effect (non-electrolyte diffusiophoresis)[44] depending on the charges of the chemical species. The efficiency is around 10^{-9}. Here, to generate the asymmetric chemical reaction, light has been widely used as the driving power to create a one-side reaction or distinct reactions on Janus semiconductor micro/nanomotors in aqueous suspension.[42]

Micro/nanoscale motors also self-propel via generating non-uniform local heat distribution, namely the self-thermophoresis. A simple motor of this kind can be made of a silica microsphere with half-coated gold.[45,46] Upon illumination by a 1064 nm laser, the gold coating effectively adsorbs the light and generates a much greater amount of heat than that of the Si hemisphere, which leads to a localized temperature gradient. The motor is thus propelled with speed proportional to the temperature gradient (∇T) and thermodiffusion coefficient (D_T), given by $v = -D_T \nabla T$. The energy efficiency of $10^{-13}$is among the lowest.

Direct bubble propulsion is another power source that requires a rapid chemical reaction to generate gas-phased products distributing asymmetrically near a motor.[47,48] A representative bubble motor is made of a conical tube that consists of a catalytic layer of Pt at the inner surface that decomposes H_2O_2 fuel into oxygen molecules. When the oxygen molecules enrich into a bubble of a threshold size, it departs from the motor with a strong and instant thrust that propels the motor.[49] The energy efficiency is estimated to be around 10^{-9}.

In addition, several other notable mechanisms have been demonstrated to introduce asymmetry to a micro/nanomotor, including propelling near a solid wall,[50-52] generating asymmetric body deformation with dynamic light patterning,[53] and actuation in non-Newtonian liquid.[54]

1.2.5. Powering by Energy from an External Tweezing Field

Unlike the self-propelled motors that generate local thrusts for actuation, another class of motors is propelled via directly interacting and transferring propulsion momentum from an external physical field. These manipulations are more commonly termed as tweezing techniques, including optical,[55] electric,[56] magnetic,[57] and acoustic tweezers.[58]

Optical tweezers are powerful tools in manipulating objects around or below several microns. They utilize a highly focused laser beam to generate an optical trap (or barrier) for manipulating micro/nanoparticles near the focal plane by optical gradient forces.[55] Holographic beams allow not only trapping, but also the individual or simultaneous movement of multiple particles via independent manipulation of optical traps.[59] The electric manipulations are able to exert a net force and an alignment torque upon a particle by applying a combined AC and DC electric field. The force is generated

by electrophoresis/electroosmosis for a charged particle; the torque is created by the interaction between the AC field and the polarized particle. Optoelectric tweezers utilize dielectrophoretic (DEP) forces from a localized field gradient patterned by light on an electrically powered light-sensitive substrate.[60] Furthermore, rotational torques can be generated from an electric field, *i.e.*, electro-rotation and electro-orientation in a high-frequency AC electric field.[61] Acoustic manipulations leverage the acoustic radiation force induced by either standing waves or traveling waves to manipulate particles.[58] Standing-wave acoustic tweezers generate ordered arrays of pressure nodes in the field where many particles can be trapped into ordered arrays.[62] Traveling-wave acoustic tweezers, *i.e.*, acoustic hologram, can create pressure nodes with arbitrary 3D patterns by modulating the phase of the wave actively or passively.[63,64] Magnetic tweezers exert forces to magnetic micro/nanoobjects in the direction of the local magnetic-field gradient and apply alignment torques in the direction of the local magnetic field.[57]

To accommodate manipulations with high versatility and/or in complex suspension medium, hybrid powers have recently been exploited, including light-modulated multimode reconfigurable micromotors in electric fields,[65,66] sperm-powered biohybrid motors steered by magnetic fields,[67] and dual chemical/light-powered motors and chemical/electric-field powered motors with tunable speeds.[68,69] Research in hybrid-powering mechanisms has enabled the control of different components within a nanorobot for sophisticated operations and the manipulation of individual nanorobots in a swarm for a collaborative action.

Chapter 2: Background of Electrokinetics

In this Chapter, a brief background introduction about the electrokinetics will be provided. The major references of this chapter are two textbooks: ***Electromechanics of particles*** (TB Jones 2005)[61] and ***Electrokinetic and Colloid Transport Phenomena*** (JH Masliyah and S Bhattacharjee 2006).[70] The electrokinetics describes the phenomena associated with the movement of objects and flow of the fluid under the influence of an electric field. As the electrical driven motors described in this dissertation are all working in aqueous environment, the transport of ions in the surrounding medium play an important role under the influence of the electrical field. A rigorous treatment of electrokinetic phenomena requires understanding of a complex system coupling fluid mechanics, colloidal phenomena, electrostatics, mass transfer etc. However, this chapter will only introduce necessary fundamentals of the electrokinetics and try to avoid too much mathematical description as the focus of this dissertation is the engineering and application perspectives of the phenomena. In the following, the concepts of electrical double layer, electrophoresis, and three induced dipole related electromechanical phenomena will be introduced sequentially.

2.1. Electrical Double Layers

Electrical double layers (EDL) are well-known phenomena associated with mobile ions and their spatial redistribution under the influence of a charged surface or applied electrical field. The presence of charged surface such as charged particle, solid surface, emulsion droplet etc., induces local electric field that either attracts or repels the ions from the surface depending on the sign of the charges. An equilibrium is established when the redistribution of free ions balances the surface charge. Such distribution of free ions in the

solution together with the surface charge together compromise what are known as electric double layers.

When electrolytes are present in aqueous solution, without the disturbance of any field or charged objects, the electroneutrality is always satisfied everywhere. However, when a charged surface is presented in the solution, i.e. a negatively charged polystyrene particle, ions of opposite charge called counterions, will be attracted toward the surface, and ions with common charge will be repelled from the surface. As a result, the electroneutrality is no longer valid near the vicinity of the surface, yet at the locations sufficiently far away from the surface, the electroneutrality is still satisfied. In general, the electrical double layer consists of two layers, one is the charged surface, and the other the layer where ions redistributed in the vicinity of the surface.

The Gouy-Chapman model introduces a diffuse double layer considering the thermal motion caused spreading of the ions under concentration gradient. A qualitative prediction is available from the model for a low surface potential (~0.025 V) with moderate electrolyte concentration. The model assumes a boltzmann distribution of ionic conentration due to the electric potential, and leads to the well-known governing equation called Poisson-Boltzmann equation:

$$\varepsilon \frac{d^2\psi}{dx^2} = -\sum_{i=1}^{N} z_i e n_{i\infty} \exp\left(-\frac{z_i e \psi}{k_B T}\right) \tag{2.1}$$

where ε is the permittivity of the medium, ψ is the electrical potential, z_i is the valence of the ion, e is the elementary charge, $n_{i\infty}$ is the ion concentration in the bulk solution, k_B is the Boltzmann constant, and T is the temperature.

For a symmetric electrolyte with only one composition, such as NaCl, where $z_+ = -z_- = z$, equation (1) can be written as

$$\varepsilon \frac{d^2\psi}{dx^2} = 2zen_\infty \sinh\left(\frac{ze\psi}{k_B T}\right) \tag{2.2}$$

where $n_{+\infty} = n_{-\infty} = n_\infty$ as the bulk concentration of the electrolyte. With the following boundary conditions:

$$\begin{aligned} \psi &= \psi_s \quad x = 0 \\ \psi &= 0 \quad x \to \infty \end{aligned} \tag{2.3}$$

where ψ_s is the surface potential, governed by the surface charge density. The solution of equation(2) under the boundary conditions is:

$$\Psi = 2\ln\left[\frac{1 + \exp(-\kappa x)\tanh\left(\frac{\Psi_s}{4}\right)}{1 - \exp(-\kappa x)\tanh\left(\frac{\Psi_s}{4}\right)}\right] \tag{2.4}$$

where $\Psi = \frac{ze\psi}{k_b T}$ and $\Psi_s = \frac{ze\psi_s}{k_B T}$ are the dimensionless potential, and κ^{-1} is called the Debye length, which is defined as:

$$\kappa^{-1} = \left(\frac{\varepsilon k_B T}{2e^2 z^2 n_\infty}\right)^{\frac{1}{2}} \tag{2.5}$$

Furthermore, when the surface potential is small ($\psi_s \ll 0.025\ V$) , the following approximation can be applied to equation (2.2):

$$\sinh\left(\frac{ze\psi}{k_B T}\right) \approx \frac{ze\psi}{k_B T} \quad \text{when} \frac{ze\psi}{k_B T} \ll 1 \tag{2.6}$$

Adopting the same boundary condition from equation (2.3), the solution can be given by:

$$\psi = \psi_s \exp(-\kappa x) \tag{2.7}$$

The above approximate solution of the electric potential is called Debye-Hückel solution, which clearly shows that the electric potential decays as the distance from the surface increases, and the Debye length defined as equation (2.5) is the characteristic length of the double layer.

To be noticed, the low surface potential condition may not be valid for many practical systems, however, the solution from such approximation, called Debye-Hückel

approximate solution, can still provide a fairly reasonable prediction of the electric potential.

For most of the experiments that are going to be discussed in this thesis, the solution is deionized water (DI water) with a measured conductivity of 4 $\mu S/cm$ unless specifically noticed. Although we used deionized water that is processed by deionization, there are residual ions such as H+, OH-, as well as HCO3- due to CO2 dissolution, resulting in a finite electric conductivity (4 $\mu S/cm$). We are not able to determine the exact concentration of each type of ions in the DI water, but we can still provide a reasonable estimation from the measured conductivity with some reasonable assumptions. Assuming that the dominating ions in the DI water are H+, OH- and HCO3- with respective mobilities of $3.623 \times 10^{-7}, 2.064 \times 10^{-7}$ and 7.46×10^{-8} $m^2\ S^{-1}\ V^{-1}$. From these values and the measured electric conductivity of DI water, we can estimate the total concentration of ions that contribute to the EDL as $1 \times 10^{-5} \sim 5 \times 10^{-5}$ M and calculate the estimated Debye length as 50 ~ 100 nm. The estimation of Debye length is essential as it will be discussed later.

2.2. Electrophoresis

When nanoparticles are suspended in aqueous solutions, in most cases, a certain type of charge are distributed on their surfaces depending on the chemical ions in the suspension and dangling bonds on their surfaces. When a static (or DC) electric (E)-field is applied, assuming the particle has a net charge of q, then a net force $\boldsymbol{F} = \boldsymbol{E} \cdot q$ will exert on the particle and result in linear motions in the direction of the force. However, a more accurate understanding of electrophoresis must take account of the presence of electrical double layers next to the surface of the nanoparticles.

As previously discussed, in the diffusion layer, the electroneutrality is not satisfied, and a non-zero volumetric charge density exists. When an external electric field applies, the electrostatic force exerted on the ions will result in a non-zero body force that move the fluid within the diffuse layer. The resulting fluid flow is known as electro-osmosis flow, which slips in the outer area of the interface between the charged particle and electrolyte. In the limit of thin-double-layer, the electro-osmosis flow has a slip velocity given by the Helmholtz-Smoluchowski formula in a wide range of conditions:

$$\boldsymbol{u_s} = -\frac{-\epsilon_w \zeta}{\eta}\, \boldsymbol{E}_{||} \equiv \boldsymbol{\mu_e} \boldsymbol{E}_{\|}, \quad (4) \tag{2.8}$$

where ϵ_w is the dielectric constant of the solvent, ζ is the zeta-potential, $E_{\|}$ is the applied E-field, and $\mu_e = \epsilon_w \zeta / \eta \propto q$ is the electrophoretic mobility of the particle. The zeta-potential (ζ) indicates the electrostatic potential drop through the screening layer. The surface electro-osmosis flow in one direction will give rise to motion of the particle in the opposite direction, the so-called electrophoresis. Therefore, electrophoretic velocity is still proportional to external E-field and particle surface charge, which accord with the intuition that E-field directly act on the charged particle, but with a constant multiplied, due to its microscopic electrokinetic mechanism. Since most nanoparticles in suspension are surface charged, by simply applying a DC E-field, the electrophoretic force will drive the particles to transport along or opposite to the E-field direction depending on the sign of surface charges.

2.3. Dipole Interactions

When an electric field is applied to the solution with particles in dispersion, the field will drive the drifting motion of charge carriers or reorient the internal dipoles within particles and resulting in induced dipole moments. The interaction between the induced

dipole moment of the particle and the electric field can a series of mechanical motions in addition to the previously discussed electrophoresis phenomenon.

2.3.1. Electric Polarization of Colloidal Particles

When a particle is subjected to an electric field, an electrical polarization is induced. The dipole moment is given by $\boldsymbol{p} = \alpha \boldsymbol{E}$, where α is the polarizability tensor of the particle. When the field becomes alternative, the polarizability becomes a function of frequency. The frequency-dependent electric polarization of dielectric materials is known as the dispersion. In optical frequencies, the Lorentz model can well explain the dispersion relation of dielectric materials originate from multiple relaxation mechanisms. In most dielectrophoresis experiments, however, the frequency range of the alternating electric field is much lower and falls in the range of kHz to MHz, where the relaxation processes of atomic dipole, ionic polarization and electronic polarization are not observed.[71] The only possible relaxation mechanism in these frequencies is the interface relaxation, also known as the Maxwell-Wagner interfacial polarization, which is originated from the discontinuity of the electrical properties at the interface between two mediums.

For ellipsoid particles with a, b, c as half the length of the principal axes for two reasons: 1) an analytical solution exists for ellipsoid particles when it is subjected to a uniform electric field along the principal axes. 2) a model of ellipsoid particles can predict the behavior of microparticles of interest with shapes ranging from spheres, disks to rods, which are often made and used. In terms of the boundary value problem of an ellipsoid particle suspended in a uniform medium and a uniform electric field, an analytical solution exists. Suppose that the a, b, c axes of the ellipsoid particle are aligned along x, y, z axes

of the coordinate system, respectively, the x component of the particle's electric polarization for example, can be expressed as:

$$p_x = \frac{4\pi abc}{3}\varepsilon_1 \frac{\underline{\varepsilon_2} - \underline{\varepsilon_1}}{\underline{\varepsilon_1} + \left(\underline{\varepsilon_2} - \underline{\varepsilon_1}\right) L_x} E_x = \alpha_x E_x \tag{2.9}$$

where ε_1 is the real permittivity of the medium, $\underline{\varepsilon_1}, \underline{\varepsilon_2}$ are the complex permittivity of the medium and the particle, respectively, given by $\underline{\varepsilon_i} = \varepsilon_i - \frac{i\sigma_i}{\omega}$, and L_x is the depolarization factor defined by the following elliptical integral:

$$L_x = \frac{abc}{2}\int_0^\infty \frac{ds}{(s+a^2)\sqrt{(s+a^2)(s+b^2)(s+c^2)}}. \tag{2.10}$$

Similarly, the expression for $p_y \; and \; p_z$ can be obtained by the substitution of L_x and E_x in Equation (2.9) with the corresponding terms for the respective direction. The Clausius-Mossotti factor K is defined as:

$$\mathrm{K} \equiv \frac{\underline{\varepsilon_2} - \underline{\varepsilon_1}}{3\underline{\varepsilon_1} + 3\left(\underline{\varepsilon_2} - \underline{\varepsilon_1}\right) L_x} \tag{2.11}$$

which governs both the frequency dependence and the geometry dependence of the polarization.

2.3.2. Electro-Rotation

When a rotating AC E-field is applied via the quadruple electrodes, an electric torque is exerted on the induced dipole moment of the particle, a nanowire for example, and compels its rotation. A rotating AC E-field is generated by applying four AC voltages with 90° sequential phase shift on the quadruple electrodes. The E-field can be given by $\boldsymbol{E}(\mathbf{t}) = E_0 \mathrm{Re}\left[(\hat{\mathbf{x}} - \boldsymbol{i}\hat{\boldsymbol{y}})e^{i\omega t}\right]$, for the counterclockwise rotation. The particle is polarized with a total dipole moment ($\underline{\boldsymbol{p}}$), expressed as $\underline{\boldsymbol{p}} = \underline{\alpha_x}\,\underline{\boldsymbol{E_x}} + \underline{\alpha_y}\,\underline{\boldsymbol{E_y}} = \underline{\boldsymbol{p_x}} + \underline{\boldsymbol{p_y}}$, where $\underline{\alpha_x}$ and $\underline{\alpha_y}$ are the complex polarizability along the two in-plane axes orthogonal to each

other. The underbars denote the complex variables with phasor. Since the angular frequency of the AC E-field is much higher than that of the rotation speed of the nanowire, in the frequency region that we are studying, we can assume that the nanowire remains still while the AC E-field oscillating one cycle, and then the time-averaged electrical torque can be readily written as:

$$\boldsymbol{\tau}_{rotation} = \frac{\mathbf{1}}{\mathbf{2}}\mathrm{Re}\left[\underline{\boldsymbol{p}}(\boldsymbol{t}) \times \underline{\boldsymbol{E}}^{*}(\boldsymbol{t})\right] = -\frac{\mathbf{1}}{\mathbf{2}}E_0^2\,\mathrm{Im}\left[\underline{\alpha_x} + \underline{\alpha_y}\right]\hat{\mathbf{z}}. \tag{2.12}$$

Owing to the low dimensions, a nanowire is in an extremely low Reynolds number regime, where viscous force dominants motion and the drag torque is proportional to the rotation speed. The driving electric torque on the nanowire is balanced by the liquid drag torque essentially instantly, given by $\tau_e = -\tau_{drag} = \gamma\dot{\theta}$, where γ is the rotational drag coefficient of a nanowire in deionized water.

2.3.3. Electro-Alignment

If the particle is non-spherical with anisotropy in the electric polarizability, an alignment torque is exerted on the particles, which is termed electro-alignment. When the dipole moment is directed at an arbitrary angle to the electric field, an electric torque, given by $\boldsymbol{\tau} = \boldsymbol{p} \times \boldsymbol{E}$, exerts on the nanowire and orients it until the electrostatic energy is minimized. For simplicity, we consider only a 2D case, where the motions and the involved forces are both in-plane with the microelectrodes. We can express the electric field along the x-axis with $\boldsymbol{E} = \mathrm{Re}[E_0\hat{\boldsymbol{x}}\exp(i\omega t)] = \mathrm{Re}[\underline{\boldsymbol{E}}\exp(i\omega t)]$, where $\underline{\boldsymbol{E}} = E_0\,\hat{\boldsymbol{x}}$ is the phasor of electric field, E_0, ω, and t are the amplitude of electric field, angular frequency of the electric field, and time, respectively. The dipole moment ($\boldsymbol{p}$) of the nanowire can be decomposed into two components that are parallel and perpendicular to the long direction of the nanowire, given by $\underline{\boldsymbol{p}_{\parallel}} = \alpha_{\parallel}\underline{\boldsymbol{E}_{\parallel}}$ and $\underline{\boldsymbol{p}_{\perp}} = \alpha_{\perp}\underline{\boldsymbol{E}_{\perp}}$, respectively. Here $\underline{\boldsymbol{p}_{\boldsymbol{i}}}, \alpha_i, \underline{\boldsymbol{E}_{\boldsymbol{i}}}$ ($i =$

$\parallel$ or $\perp$) are the phasor of dipole moment, complex polarizability, and the phasor of the electric field along the respective directions. Since the frequency of the AC electric field employed in our experiments is much higher than that of the rotational motion during nanowire alignment, the time-averaged torque ($\boldsymbol{\tau}$) exerted on a nanowire results in the observed alignment, which can be expressed as:

$$\boldsymbol{\tau}_{alignment} = \frac{1}{2}\mathrm{Re}\left[\underline{\boldsymbol{p}} \times \underline{\boldsymbol{E}}^{*}\right] = -\frac{1}{2}E_0^2\mathrm{Re}(\alpha_{\parallel} - \alpha_{\perp})\sin\theta\cos\theta\,\hat{\mathbf{z}} \tag{2.13}$$

where θ is the angle between the long axis of the nanowire and the electric field, and $\underline{\boldsymbol{E}}^{*}$ denotes the complex conjugation of the electric field phasor. As a result, the rotation speed of a nanowire during an electro-alignment depends on the instantaneous angle (θ) between the long axis of the nanowire and the electric field, and is given by:

$$\dot{\theta} = -\mathrm{A}\sin\theta\cos\theta \tag{2.14}$$

where $A = \frac{E_0^2}{2\gamma}\mathrm{Re}(\alpha_{\parallel} - \alpha_{\perp})$ is defined as the alignment rate, which can be calculated from the experimental data as:

$$A = \frac{-1}{t_2 - t_1}\int_{\theta_1}^{\theta_2}\frac{d\theta}{\sin\theta\cos\theta} \tag{2.15}$$

Note that as the nanowire approaches $\theta = 0$ and $\pi/2$, the rotation speed approaches zero and equation (2.15) has non-integrable singularities. Also, Brownian motion dominates, adding noise to measurements. So, to ensure accuracy in our calculation of A, we restrict data analysis to $|\theta_1 - \pi/4| < 0.5$ and $|\theta_2 - \pi/4| < 0.5$. We also require $|\theta_1 - \theta_2| > 0.5$ to avoid errors from the calculation based on data set with too few data points.

Note that equation (2.14) implies the nanowire rotation speed is zero at angles $\theta = 0$ or $\pi/2$ and half of A when $\theta = \pi/4$. The alignment rate (A) can be experimentally determined by equation (2.15). Furthermore, since A is linearly proportional to $\mathrm{Re}(\alpha_{\parallel} - \alpha_{\perp})$, one can readily determine the real part of the anisotropy of polarizability of a nanowire

at a given electric field strength (E_0) and viscous drag coefficient (γ). A positive alignment rate (A>0) indicates $\mathrm{Re}(\alpha_{\parallel} - \alpha_{\perp})>0$, where the real part of electric polarization along the parallel direction of a nanowire is greater than that along the transverse direction, $\mathrm{Re}(\alpha_{\parallel}) > \mathrm{Re}(\alpha_{\perp})$. Vice versa, a negative alignment rate (A<0) corresponding to $\mathrm{Re}(\alpha_{\parallel} - \alpha_{\perp}) < 0$ or $\mathrm{Re}(\alpha_{\parallel}) < \mathrm{Re}(\alpha_{\perp})$.

2.3.4. Dielectrophoresis

If the field is slightly non-uniform where a gradient exists, a force termed as dielectrophoretic force is exerted on the particle, given by $\boldsymbol{F}_{DEP}(t) = \boldsymbol{p}(t) \cdot \nabla \mathbf{E}(t)$. For an AC electric field with a general expression of $\boldsymbol{E}(\boldsymbol{r}, t) = \boldsymbol{E}_0(\boldsymbol{r}, t) \cdot \exp(i\omega t)$, the DEP force is calculated as:[61]

$$\boldsymbol{F}_{DEP}(t) = \mathrm{Re}\left[\underline{\boldsymbol{p}} \exp(i\omega t)\right] \cdot \nabla \mathrm{Re}[\underline{\boldsymbol{E}_0} \exp(\mathrm{i}\omega \mathrm{t})] \tag{2.16}$$

where $\underline{\boldsymbol{p}}$ and $\underline{\mathbf{E}_0}$ are the phasor of the dipole moment and electric field, respectively. Since the AC electric field period is generally much shorter than the time scale of the particle movement, what can be observed is the time-averaged force exerted on a particle as follows:

$$\boldsymbol{F}_{DEP}(t) = \frac{1}{2}\mathrm{Re}\left[\underline{\boldsymbol{p}} \cdot \nabla \underline{\boldsymbol{E}_0^*}\right] = \frac{1}{2}\mathrm{Re}(\underline{\alpha})\nabla \mathrm{E}_{\mathrm{rms}}^2 \tag{2.17}$$

where the asterisk refers to complex conjugation, $\underline{\alpha}$ is the complex polarizability tensor of the particle, and $\mathrm{E}_{\mathrm{rms}}$ is the root mean square of the electric field intensity. A positive DEP force (pDEP), which requires a positive real part of polarizability along the direction of the electrical field gradient, drags the particle towards the high-electric-field region..A negative DEP force (nDEP) occurs with a negative real-part polarizability and repels the particle away from the high electric field region.

2.4. The Effect of EDL on the Induced Dipole

Besides the effect of Maxwell-Wagner polarization that has been calculated in equation (2.9), due to the existence of ions in aqueous solution, once the nanowire is polarized, the ions of opposite charges are spontaneously attracted towards the polarized surface to counter the surface charges and thus form charge electric layers, the so-called electrical double layers (EDL). The behavior of the electrical double layer in an AC electric field could be very complex and several models have been developed in order to predict the electrokinetic phenomena.[72-74] A full electrokinetic model that takes the induced-charge electroosmosis (ICEO) into consideration has been developed for particles with specific shapes.[75,76]

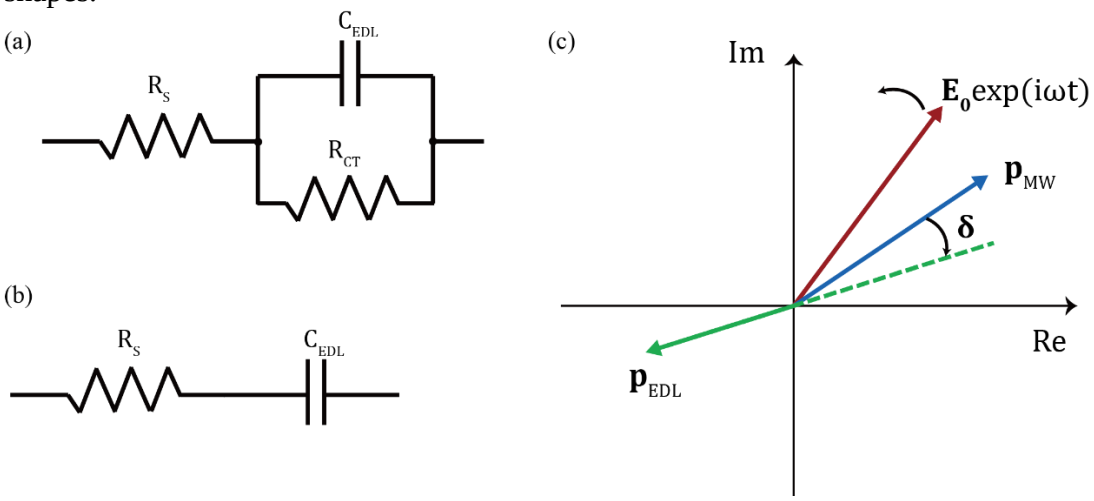

Figure 2.1. Equivalent circuit at the interface of a polarized particle and the geometric representation of phase relation of dipole moments in the complex plane. (a) The Randles circuit model describes the processes at the electrochemical interface, where R_S is the ionic resistance, C_{EDL} is the double layer capacitance and R_{CT} is the charge transfer resistance. (b) Simplified circuit when there is no faradaic reaction happens at the interface. (c) Geometric representation of the phase relation among electric field, and dipole moments from Maxwell-Wagner polarization and EDL.

Here we utilize a simplified effective dipole moment model to represent the EDL effect, governed by an RC model[22] qualitative analysis. The effective dipole from EDL is generally opposite to the dipole from Maxwell-Wagner relaxation with a certain phase lag, and can be described by a Randles circuit as shown in Fig. 2.1a. The equivalent circuit describes the electrokinetic process at the electrically polarized interfaces of the particle, where the EDL is forming to counter the surface charge from the polarized particle. The ionic resistance R_S connects in series with the double layer capacitance C_{EDL} and charge transfer resistance R_{CT} in parallel with C_{EDL}. However, in our discussion, the potential drop across the particle is insufficient for electrolysis, so that no faradaic reaction takes place, indicating an infinitely large R_{CT}. Thus, the circuit can be further simplified as an RC series circuit shown in Fig. 2.1b, with a time constant τ_{RC}. The phase relation between the local electric field, dipole moment from Maxwell-Wagner polarization and EDL are illustrated as Fig. 2.1c, where the electric field is rotating counterclockwise with frequency ω, the dipole moment from Maxwell-Wagner polarization ($\mathbf{p}_{MW}$) falls behind, and the dipole moment from EDL ($\mathbf{p}_{EDL}$) is further behind the $\mathbf{p}_{MW}$ with a phase lag of δ in the opposite direction. The effective dipole from the induced electrical double layer can be expressed as[65]:

$$\mathrm{Im}(\mathrm{P_{EDL}}) = -\frac{[\mathrm{Re}(\mathrm{P_{MW}})\sin\delta + \mathrm{Im}(\mathrm{P_{MW}})\cos\delta]}{\sqrt{\omega^2\tau_{RC}^2 + 1}} \tag{2.188}$$

$$\mathrm{Re}(\mathrm{P_{EDL}}) = -\frac{[\mathrm{Re}(\mathrm{P_{MW}})\cos\delta - \mathrm{Im}(\mathrm{P_{MW}})\sin\delta]}{\sqrt{\omega^2\tau_{RC}^2 + 1}} \tag{2.19}$$

where τ_{RC} is the time constant for EDL charging and $\tan\delta = -\omega\tau_{RC}$ as the dielectric loss tangent (here the minus sign shows that the phase of EDL falls behind the Maxwell-Wagner polarization). The value of τ_{RC} $(2 \times 10^{-5}\ \mathrm{s})$ is obtained from the fitting result of the previous experimental study in electro-rotation of silicon nanowires in the same deionized (DI) water medium.[65] We note that DI water has a finite conductivity

of $4\ \mu S/cm$, indicating the existence of trace amount of ionic charges, so that the EDL can still form in such medium. On the other hand, this simplified RC model for the EDL has several restrictions. The currently adopted value of τ_{RC} is obtained from experiments of silicon nanowires of 500 nm diameter in DI water of $4\ \mu S/cm$, where the thickness of the double layer is much smaller than the diameter of the nanowires, so that the system lies in the thin double layer limit. The same limitation is required for our model. In the following, we discuss and calculate micrometer scale particles and in DI water.

Both the Maxwell-Wagner polarization and the electrical double layer contribute to the total electric dipole moment of the particles. Both the real and imaginary parts of the total dipole moment can be calculated accordingly. In this study, we select silicon as the material of the particle and deionized water as the suspension medium. Silicon is chosen due to the earthly abundance, high photoconductivity, and relevance to various practical applications. To understand the effect of light on the modulation of the DEP forces on Si microparticles via the tuning of their electric conductivities, we systematically sweep the electrical conductivity from 0.001 S/m to 1 S/m in the calculation. The conductivity range is selected with the lower limit for the intrinsic silicon conductivity at room temperature which can have a range depending on the fabrication process, and the upper limit for an estimated magnitude of photoconductivity of microparticles under $1\ W/cm^2$ visible-light illumination.[65]

Chapter 3: Methodology

3.1. Silicon Nanowire Fabrication

We fabricate silicon nanowires via the well-known metal-assisted chemical etching (MACE) methods as previously discussed[65] with a slight modification. In brief, a dispersed monolayer of 500 nm diameter polystyrene nanospheres is assembled on a cleaned undoped silicon wafer. A catalytic metal thin film of 25 nm Ag and 5 nm Au is deposited by electron beam evaporation on the top such that the polystyrene nanospheres act as a mask for the following fabrication. A scotch tape is used to remove the nanospheres, leaving a metal film with circular nanoholes on the wafer. Immersing the sample into the etchant composed of 4.7 M hydrofluoric acid and 0.3 M hydrogen peroxide dissolves the silicon underneath the metal film to leave arrays of nanowires. Finally, we use silver and gold etchants to remove the catalytic metal layer, followed by sonication in DI water to break the nanowires off the substrate. All the nanowires used in our experiments are approximately 10 μm in length, 500 nm in diameter, and composed of undoped silicon. The nanowires are stored in DI water and used in a few days after preparation. A surface oxide layer develops in a few days.

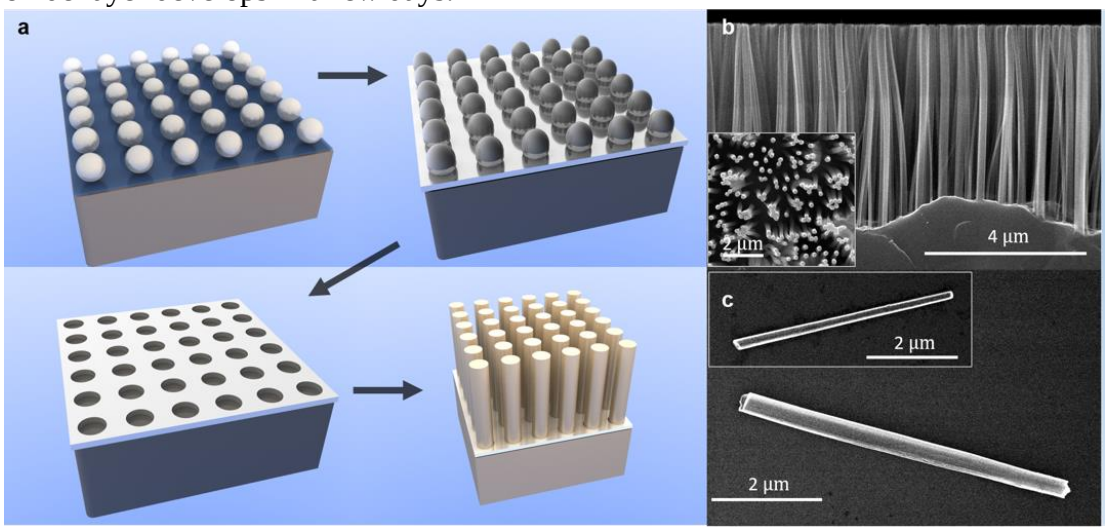

Figure 3.1. Fabrication process of Silicon nanowires and experimental setup. (a) Schematic of silicon nanowire fabrication via nanosphere lithography based on metal assisted chemical etching. (b-c) Scanning Electron Microscopy images of silicon nanowires. (b) Cross-section view of arrays of silicon nanowires of 200 nm in diameter made from n-type 560-840 Ω cm silicon wafers. (inset: top-view) (c) A nanowire of 500 nm in diameter. (inset: a nanowire of 200 nm in diameter)

The silicon nanowires used in this work were fabricated via two similar methods depending on the diameter. For nanowires diameter greater than 100 nm, nanosphere lithography masked metal-assisted chemical etching (MACE) is used.[77] First, all silicon wafers of various doping density from intrinsic (>5000 Ω cm) to highly doped (0.001~0.005 Ω cm) are rinsed and sonicated in acetone, isopropanel (IPA) and DI water each for 5 minutes sequentially. After drying in nitrogen gas flow, the wafers were immersed in Poly(diallyldimethylammonium chloride) (PDDA) (2%wt), Poly(sodium 4-styrenesulfonate) (PSS) (2%wt) and Aluminum Chlorohydrate (ACH) (5%wt) each for 30 seconds that the surface can be modified with positive/negative/positive charge layers. Next, after immersing the wafer into a PS sphere suspension for 2 minutes, a monodispersed layer of negatively charged polystyrene nanospheres is formed on the wafer. Subsequently, a reactive ion etching process was carried out to slightly reduce the size of PS spheres as well as to remove the charged polyelectrolyte layers. Then a thin silver film of 50 nm in thickness was deposited on the wafer by electron-beam evaporation. Next, we sonicated the wafer in toluene to remove the PS spheres, leaving arrays of nanoholes on the silver film. The etching was conducted in the mixture of 4.7 M HF and 0.3 M H2O2. Finally, silver was removed by nitric acid and nanowires were sonicated off the wafer in DI water. For nanowires with diameter less than 100 nm, one step synthesis was adopted by directly immersing the cleaned wafer into the mixture of 4.7 M HF and

0.02 M AgNO3.[78] After the etching, we treated the wafer with nitric acid to remove the silver dendrite and then sonicated nanowires off the wafer in DI water.

3.2. Electrode Fabrication

We also make two types of electrodes, “parallel” and “quadrupole”, for measurement of nanowire-to-E-field alignment rate and nanowire micromotor control, respectively. The electrodes are made of 5nm Cr and 100 nm Au thin film deposited via electron beam evaporation in one of two patterns (via standard photolithography), shown in Fig. 3.2, on to a glass microscope slide. The parallel electrodes are two large rectangular pads separated by a long 125 um gap, while the quadrupole electrodes are four rectangular pads surrounding a square area 500 um on a side. The parallel electrodes are used for measuring nanowire-to-E-field alignment rates because the electrode configuration creates a spatially uniform electric field in the center, thereby minimizes dielectrophoretic effects, while the quadrupole electrodes are used to change the angle of the electric field to create nanowire micromotors. The parallel and quadrupole electrodes are attached via silver epoxy to an Agilent 33250A function generator (capable of 5 kHz to 4MHz signals up to 15 Vpp) and a customized computer-controlled four-output function generator (capable of arbitrary waveforms up to 2 MHz and 30 Vpp), respectively. All reported voltages assume voltage drops in the nanowire suspension between electrodes. The electric field strength is the division of the voltage by the electrode separation distance.

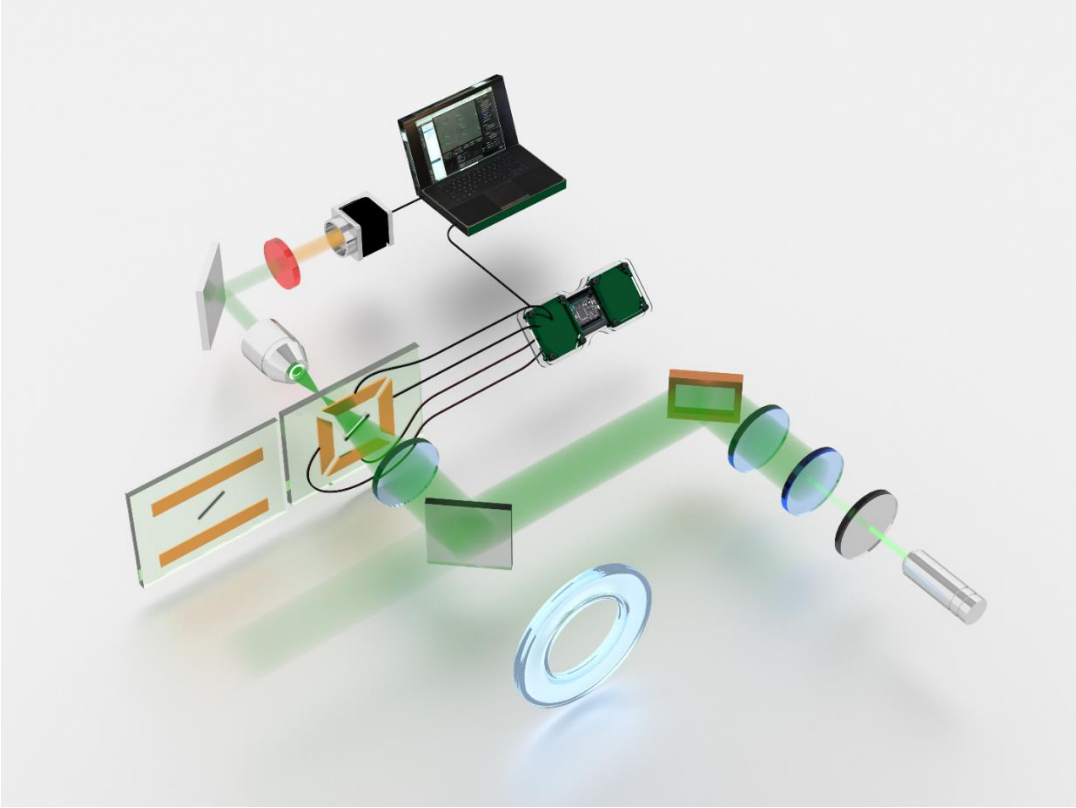

Figure 3.2. Schematic of experimental setup for switchable alignment of nanowires and rotation phase of microscale stepper motors (relative position of each component is shown; the microelectrodes faces upward in the actual setup).

3.3. Implementation of the Electric Tweezers

In each experiment, nanowires in suspension of ~20 μL is placed on top of the electrodes (either parallel or quadrupole) inside a PDMS microwell covered by a class slide. Nanowires gradually deposition to the bottom of the setup and stay in plane with the microelectrodes. A 532 nm diode-pumped solid-state laser (Thorlabs) is used for light excitation, which can be toggled off and on at different intensities. In order to reduce the influence of background light, the sample is illuminated with an always-on custom LED white light source of ~500 lx. A Basler acA1300-200um camera captures images of the

electrodes and nanowires. A computer program can track nanowire positions for data analysis via standard computer vision algorithms, and vary the voltage amplitude from the four-output function generator in real time to produce a rotating electric field.

3.4. Image Processing

A camera (Basler acA1300-200um), operating up to 1280×1024 pixels and 1000 frames per second (FPS), images the nanowires from below after the light going through a long pass filter that blocks the laser, which could otherwise damage the camera. A custom software, based on standard computer vision algorithms in C++, tracks the positions and angles of nanowires over time for later data analysis.

The camera continuously feeds images to this program, which uses the OpenCV computer vision library to recognize nanowires. Specifically, it thresholds, blurs, and extracts contours from each 8-bit grayscale image frame. Contours within a manually-set area and aspect ratio limits are set to trace nanowires, so their position and angle can be recorded, along with a unique identification number. Nanowires are tracked between frames by matching contours to their nearest neighbors with some hysteresis to account for blurred frames and other problems. The program saves the movie and records the nanowire locations and angles in real time. The entire camera-computer system regularly achieves 1000 FPS in a small image area, e.g. 200x200 px, and approximately 200 FPS at a full resolution of 1280x1024.

3.5. Digital Light Projection

We use an Olympus IX70 inverted microscope to carry out the experiments. We customized a ring-shipped LED light source to provide the background illumination and to allow the laser to pass through and equipped it on the microscope. A 532 nm laser diode from Thorlabs is employed as the laser source. The LED illuminance is measured by Dr. Meter LX1330B. Laser power is measured by Newport 1917-R power meter. The laser is reflected off a digital light projection (DLP) system using a digital micromirror device (DMD) (specifically, a DLi 4130 high-speed development kit using Texas Instrument's DLP7000 DMD chip) in order to modulate the beam before getting in the microscope optics. This allows the laser to be toggled programmatically, as utilized in the demonstration of Morse code light stimuli, and even to be masked into multiple, individually controlled spots, allowing rotation of singled-out nanowires.

Chapter 4: Light Controllable Reconfigurable Rotary Motor

In this section, we will introduce the light-controlled electro-rotation of silicon nanowires. We achieved multifold mechanical reconfigurability of nanomechanical devices, *i.e.* rotary nanomotors, in an efficient, versatile, and potentially widely applicable manner. The investigation is based on exploitation of the underlying interactions of electrokinetics around semiconductor Si nanowires, optically controlled interfacial polarization of Si nanowires in an aqueous suspension and applied high-frequency electric fields. Reconfigurable mechanical rotation of nanowires, including acceleration, deceleration, stop, and reversal of orientation are all realized by controlling illumination of visible light. The working mechanism is understood by both theoretical modeling and numerical simulations. With this newly discovered opto-mechanical effect, we demonstrate efficient non-contact differentiation of mixed metallic (Au) and semiconductor (Si) nanowires. This work could open new opportunities in identification and separation of nanoparticles and live entities. It also inspires innovative approaches to equip nanomaterials and devices with multifold light-controlled mechanical reconfigurability for the emerging nanorobotics.

4.1. Experimental Results

By applying four AC voltages with a sequential 90° phase shift and at a frequency in the range of 2.5 kHz to 2 MHz on the quadruple electrodes, a rotating AC electric field can be readily created to rotate the nanowires, an effect termed as electrorotation. The distinct rotation characterizations with and without laser illumination versus AC frequencies from 5 kHz to 2 MHz at 20 Vpp is shown in Fig. 4.1a.

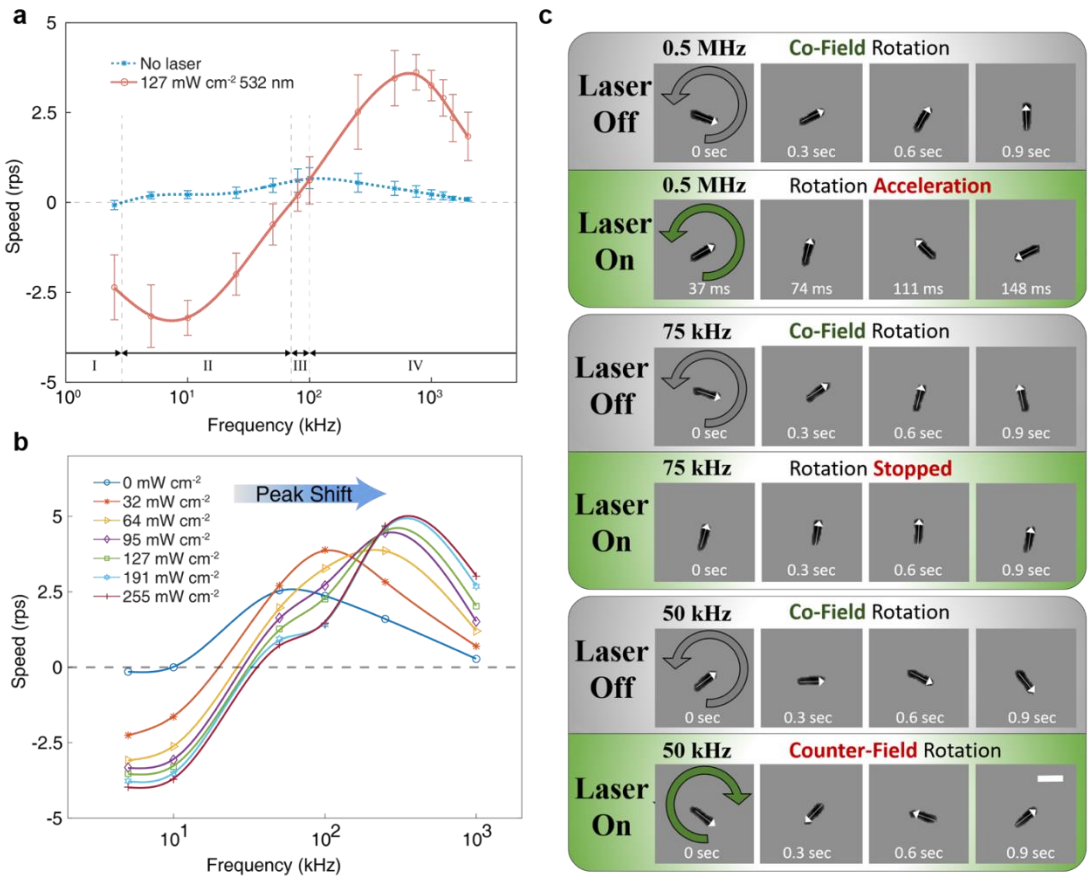

Figure 4.1. Rotation of silicon nanowires and the reconfiguration by laser illuminance in electric fields. (a) Rotation speed versus AC frequency of silicon nanowires (n-type 560-840 Ω cm, 5 μm length and 500 nm diameter) in dim environment and under 532 nm laser illumination (127 mW cm^{-2}). (b) Rotation versus AC frequency of silicon nanowires illuminated at different laser intensities. (20 Vpp at all frequencies unless stated otherwise. The eye-guiding lines are obtained with cubic spline interpolation.) (c) Snapshots of rotation of single silicon nanowires in AC frequencies of 50 kHz-0.5 MHz, showing three distinct optical responses. Scale bar, 5 μm.

In the following, we name the blue and red curves with and without laser stimuli as the bright and dim spectrum, respectively. The positive and negative signs of the rotation indicate the co-field and counter-field rotation of the nanowires to that of the external

electric fields, respectively. The dim spectrum in Fig. 4.1a, obtained at low intensity of light (~500 Lux), shows consistent co-field rotation in AC electric fields from 5 kHz to 2 MHz with a peak near 100 kHz. At low frequencies, *e.g.* 2.5 kHz, some nanowires in suspension exhibit counter-field rotation. The differences from the rotation spectra reported previously,[79] could be attributed to the differences in size, materials, and light conditions. However, under high-intensity illumination, the reversal of the rotation orientation is clearly observed at frequencies less than 50 kHz as shown in the bright spectrum (red curve) in Fig. 4.1a. Besides the reversal of the rotation orientation, laser illumination substantially increases the absolute rotation speeds of the nanowires across the entire frequency region except around the transition frequency at ~80 kHz. Two rotation peaks can be found at 10 kHz and 750 kHz, corresponding to the maximum counter-field and co-field rotation, respectively. Overall, the effect of laser to the rotation spectra can be divided into four frequency regions: Region I: low AC frequencies, below 5 kHz, increased rotation speed in the counter-field direction; Region II: from 5kHz to 80 kHz, reversed rotation orientation from co-field to counter-field; Region III: from 80 kHz to 100 kHz, lowered rotation speed in the original co-field direction; Region IV: from 100 kHz to 2 MHz, increased rotation speed in the original co-field direction.

After discovering the dramatic reconfigurable rotation of Si nanowires with optical illumination, we systematically investigated the effect of laser intensity on rotation spectra by tracking a single nanowire through all intensity conditions and frequencies (Fig. 4.1b). Obviously, the increase of the laser power from 0 to $255\ \mathrm{mW\ cm^{-2}}$ enhances the rotation speed at both high and low frequencies, while the peak positions of the co-field rotation blue shift from ~50 kHz to above 300 kHz monotonically.

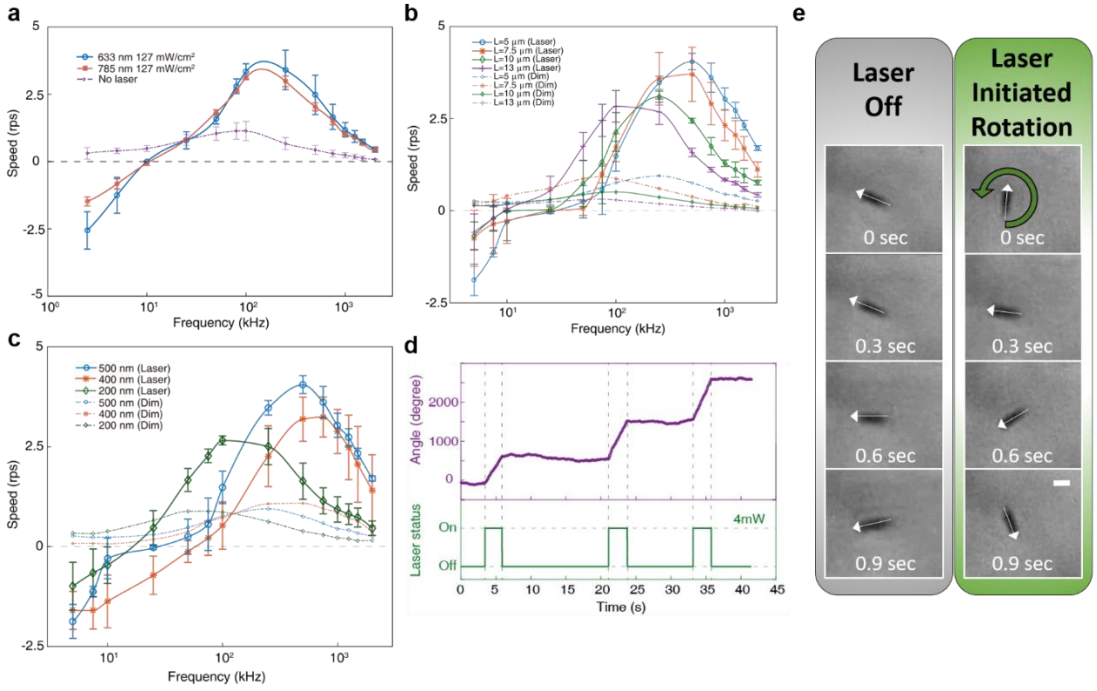

Figure 4.2. Reconfigurable rotation of Si nanowires under different laser illumination and with different geometric dimensions in an AC electric field. (a) Rotation spectra of silicon nanowires under illumination of 633 nm and 785 nm lasers. (b) Rotation spectra of intrinsic silicon nanowires of 500 nm in diameter and lengths ranging from 5 μm to 13 μm. (c) Rotation spectra of intrinsic silicon nanowires of 5 μm in length and various diameters ranging from 200 nm to 500 nm. (d) Rotation angle versus time showing optically initiated rotation of nanowires of sub-100 nm in diameter. (0.5 MHz, 20 Vpp) (e) Snapshots of laser induced rotation of a nanowire of sub-100 nm in diameter. Scale bar 2 μm.

A similar opto-responsive rotation is observed with laser illumination at 633 nm and 785 nm ($127\ \mathrm{mW\,cm^{-2}}$) as shown in Fig. 4.2a. How the mechanical rotation of nanowires responding to light of different wavelengths is determined by their material properties as well as the geometries, which will be further investigated in a separation effort. In this work, we found the versatile reconfiguration of Si nanowires is widely attainable with a light source from the visible to near infrared regime, which is desirable for a variety of applications.

The above strong light sensitivity in electro-rotation is obtained from Silicon nanowires of 500 nm in diameter. It is interesting to know if such an optical reconfigurable effect can be obtained from nanowires of different dimensions. To investigate the size effect, we selected intrinsic Si nanowires to remove possible experimental uncertainties due to dopant variations if using n/p type nanowires. A series of experiments are carried out. At a fixed diameter of 500 nm, we tested nanowires with four different lengths of 5 μm, 7.5 μm, 10μm and 13μm. The aforediscussed opto-reconfigurable effect exists strongly in all of them as shown in Fig. 4.2b. We found light stimulation always blue-shifts the rotation spectra with significantly enhanced magnitude of peak speeds for both co-field and counter-field rotation. Furthermore, for conditions with or without light, with the increase of length of nanowires, the peak frequencies for co-field monotonically shift to lower frequencies. The peak magnitude also systematically decreases as the length of nanowires increases, which agrees with the modeling to be discussed later.

We also tested nanowires of different diameters of 500 nm, 400 nm 200 nm with a same length of ~ 5 μm as shown in Fig. 4.2c. Ultra-fine nanowires with sub-100 nm diameters are also fabricated. All nanowires exhibit the opto-reconfigurable responses, including the ultrafine wires of sub-100 nm in diameter. For larger-diameter nanowires of 400 nm- 500 nm, it can be found that the peak frequencies of co-field rotation are located fairly closely between 500 to 750 kHz. Such a peak frequency clearly red-shifts to ~100 kHz when the diameter is decreased to 200 nm. It is also observed that the magnitude of the peak speed of co-field rotation decreases with the reduced diameter of 200 nm. These results agree with the simulation to be discussed later. Here we note that the peak frequencies of nanowires with 400 nm and 500 nm diameters are located closely with that of the 400 nm nanowires slightly positioned on the left. This can be attributed to the similar aspect ratios of 10-12.5 of these nanowires as well as the dimensional distribution from the

fabrication process that can generate much errors in the rotation-spectrum tests. Although the movement of ultrafine nanowires due to Brownian motions is much stronger compared to other nanowires, we still observed the dramatic change of rotation speed when turning the laser on and off (Fig. 4.2d). With the 532 nm laser on ($127\ \mathrm{mW\ cm^{-2}}$), the nanowire instantly switches to continuous rotation from random Brownian movement at an AC field of 0.5 MHz, as shown in the snap shots in Fig. 4.2e. Overall, the experimental results of both the length and diameter-dependence tests under laser illumination show expected and understandable trends.

These experimental studies demonstrate that the manner of reconfiguration of the nanowires, including acceleration, deceleration and reversal of rotation chirality, depends on factors including AC frequency, laser power, and dimensions of silicon nanowires. The optical response of electrorotation is applicable to Si nanowires with wide range of sizes as well as various resistivity from intrinsic (>5000 Ω cm) to moderately n-doped silicon (0.6-0.75 Ω cm), while the highly n-doped degenerate silicon nanowire (0.001-0.005 Ω cm) does not response to the light, which will be discussed later. The same effect is also observed in p-type silicon nanowires, and can be applicable to other types of photosensitive semiconductors and polymers. To understand these complex phenomena, we conducted both theoretical analysis and numerical simulations.

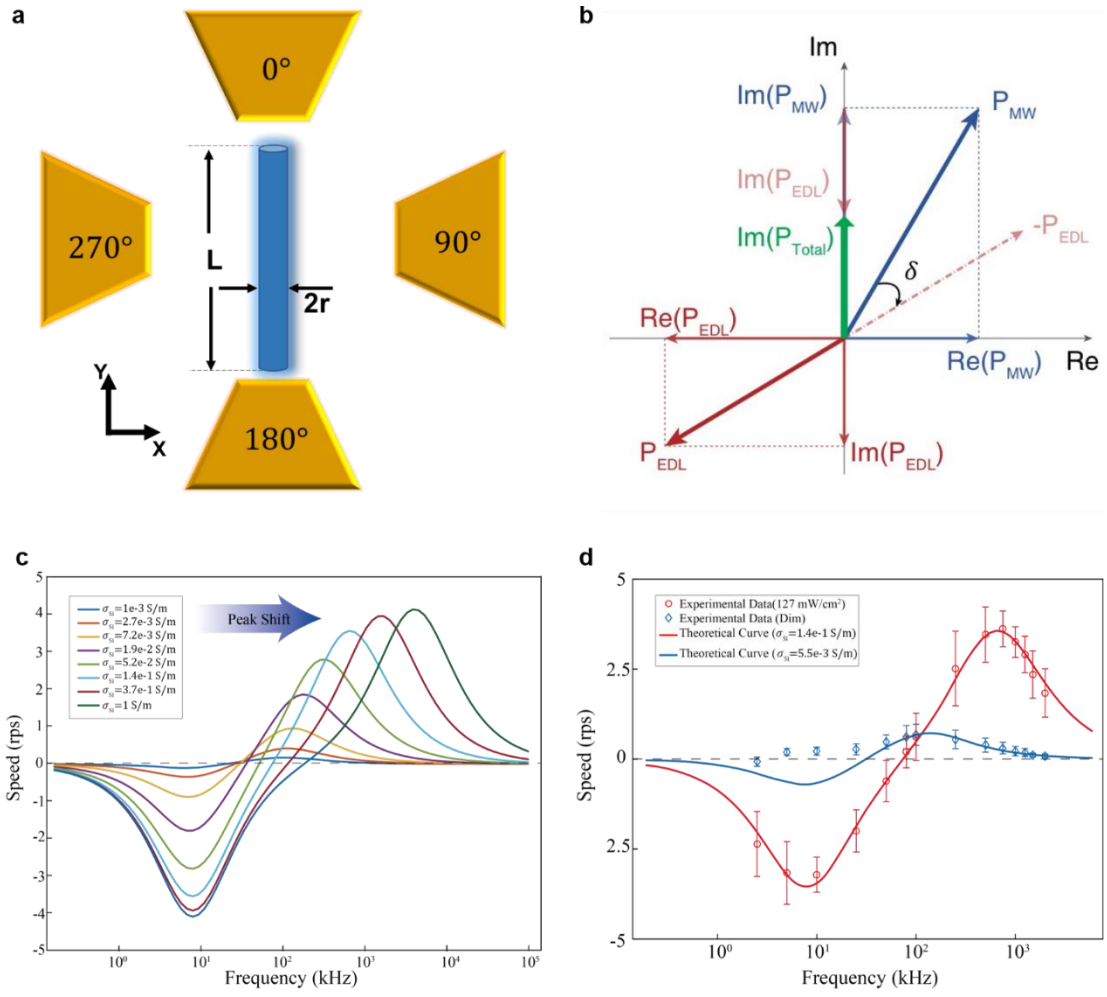

Figure 4.3. Modeling of nanowire polarization and theoretical calculation of rotation speed versus AC frequency of silicon nanowires of L = 5 μm and r = 250 nm. (a) Model of a Silicon nanowire as a cylinder with length L and radius r. (b) Schematic of the real and imaginary dipole moment components induced by the Maxwell-Wagner relaxation and electrical double layer effect. (c) Theoretical calculation of the rotation of nanowires of different electric conductivities versus AC frequency. (d) Theory compared to the experimental results. The two particular electrical conductivities are obtained from fitting at the dim and bright conditions.

4.2. Theoretical Modelling and Analysis

In a low frequency limit, the charges due to the Maxwell-Wagner polarization on the nanowire can be fully screened by the EDL, resulting in $\boldsymbol{p_{EDL}} \approx -\boldsymbol{p_{MW}}$, where the

total dipole moment essentially cancels out with a negligible negative residue ($0 < \frac{|\mathbf{p_{EDL}}|-|\mathbf{p}_{MW}|}{|\mathbf{p}_{MW}|} \ll 1$) as the thickness of EDL is much smaller compared to the size of the nanowire. In a high AC frequency, given the RC model, the resulted magnitude of dipole moment of EDL can be expressed as $|\boldsymbol{p}_{\mathbf{EDL}}| = |\boldsymbol{p}_{\mathbf{MW}}| \frac{1}{\sqrt{\omega^2\tau_{RC}^2+1}}$. Here, we need to take phasor into consideration due to the phase lag between $-\boldsymbol{p}_{EDL}$ and $\boldsymbol{p}_{\mathbf{MW}}$, the tangent of the phase lag (δ) is calculated as $\tan\delta = -\omega\tau_{RC}$, the negative sign of which indicates a phase delay as shown in Fig. 4.3b. Therefore, the Imaginary part of EDL induced dipole moment $\mathrm{Im}(\boldsymbol{p}_{\mathbf{EDL}})$ is calculated as previously mentioned in equation (2.19)

The total electric dipole moment of the nanowire system ($\boldsymbol{p}_{\mathbf{total}}$) includes both the Maxwell-Wagner relaxation process ($\mathbf{p}_{\mathbf{MW}}$) and the EDL component ($\mathbf{p}_{\mathbf{EDL}}$). The imaginary component of $\boldsymbol{p}_{\mathbf{total}}$ is given by:

$$\mathrm{Im}(\boldsymbol{p}_{\mathbf{total}}) = \mathrm{Im}(\boldsymbol{p}_{\mathbf{EDL}}) + \mathrm{Im}(\boldsymbol{p}_{\mathbf{MW}}) \tag{4.1}$$

The values of different parameters used in the calculation are listed in Table 1, in which τ_{RC} is chosen to best fit the experimental data of Fig. 4.1a. The electric conductivity of Si is systematically swept from 1×10^{-3} S m^{-1} to 1 S m^{-1}.

Parameters	τ_{RC}	$\varepsilon_p/\varepsilon_0$	$\varepsilon_m/\varepsilon_0$	σ_m
Value	2×10^{-5} s	12	80.2	4 μs cm^{-1}

TABLE 4.1. VALUES OF PARAMETERS OF SI NANOWIRE AND MEDIUM USED IN THE MODELING.

The nanowire suspended in water with maximum rotation speed less than 5 r.p.s. is within the low Reynolds number region ($\mathrm{Re} \ll 1$), and thus the system is in viscous laminar flow limit, free of turbulence with a constant drag coefficient of:[80]

$$\gamma = \frac{\tau_\eta}{\omega} = \frac{\pi\eta l^3}{3(\sigma - 1.14 - 0.2\sigma^{-1} - 16\sigma^{-2} + 63\sigma^{-3} - 62\sigma^{-4})} \quad (4.2)$$

where $\sigma = \ln\frac{L}{r}$. For a nanowire with 500 nm diameter and 5 μm length, the drag coefficient is calculated as 8.3×10^{-20} N m s rad^{-1}. Therefore, the rotation spectrum of Si nanowires versus AC frequencies can be readily calculated theoretically by combining equation (2.10) and (4.2) as shown in Fig. 4.3c.

It is known that for semiconductors, photon excitation can generate additional free charge carriers, resulting in additional electric conductivity, the so-called photoconductivity. Previous studies show Si nanowires have strong photon response,[81,82] where the increase of electric conductivity can reach several orders of magnitude. When we monotonically increase the electric conductivity of Si from 1×10^{-3} S m^{-1} to 1 S m^{-1}, the peaks of both the co-field and counter-field rotations blue shift and the magnitudes of both increase substantially (Fig. 4.3c). These spectrum characteristics obtained from the calculation agrees reasonably well with those obtained in our experiments as shown in Fig. 4.3d. It suggests that the enhanced electric conductivity of Si due to light illumination is the key factor that leads to the observed reconfigurability of rotation of nanowires. The theoretical fitting of the bright spectrum agrees well through the entire frequency range for an electric conductivity of $1.4\text{x}10^{-1}$ S m^{-1}. Here we noticed that this conductivity is close to that of the wafer from which the nanowires are synthesized. However, as shown by previous works, due to the surface depletion effects, the carrier density of Si nanowires is usually much lower than that of the wafer, since surface states at the interface between silicon and natural oxidization layer trap most carriers from dopants (Appendix A).[83,84] With numerical simulation and calculation with consideration of light absorption and recombination rate, we further estimated the photoconductivity of Si nanowires,[85-87] which is on the same order of magnitude of that obtained from the fitting.

It suggests the good feasibility of the modeling. It also indicates that the photon-generated carriers contribute majorly to the effective conductivity of silicon at our light illumination conditions.

The theoretical fitting to dim spectrum agrees in high frequencies while deviates in low frequencies, *e.g.* the counter-field rotation is shown in fitting but not observed in these experiments (Fig. 4.3d). This could be attributed to the simplified consideration of the charge distribution in nanowires that induce EDL when light is weak (dim environment). In reality, when light is dim, the carrier density is low and the Maxwell-Wagner polarization induced net charges not only accumulate at the surface, but also distribute inside the silicon nanowire. Since the EDL is only sensitive to the surface charge, ineffective in responding to charges away from the surface, a weaker EDL compared to that used in the theoretical analysis is expected, which could account for the observed difference between the calculation and experiments at low frequencies.

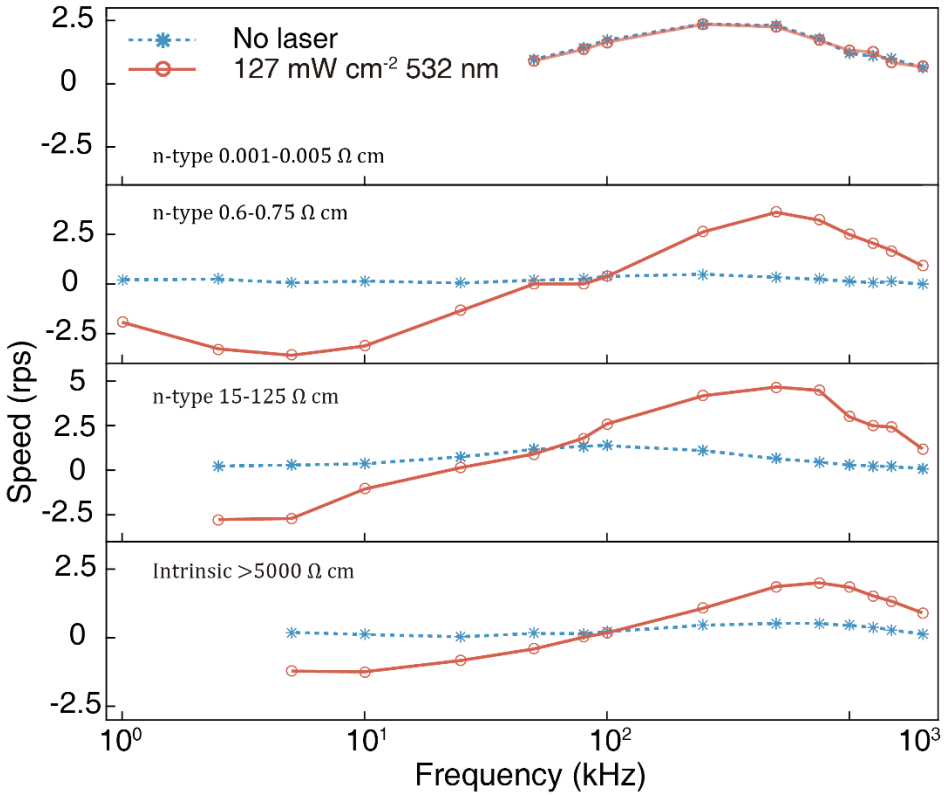

Figure 4.4. Rotation spectra of nanowires made from silicon wafers of various n-doping densities. All nanowires are ~5 μm in length and 500 nm in diameter. 532 nm laser of 127 mW cm^{-2} is adopted as optical stimuli.

Similar reconfigurable behaviors are observed in a wide range of Silicon nanowires made from n-doped wafers of 0.6- 0.75 Ω cm to intrinsic Si of over 5000 Ω cm (Fig. 4.4). For the Si nanowires made from Si wafers of 0.001-0.005 Ω cm with a high doping level of $\sim 10^{19}$ cm^{-3}, the optical stimuli can no longer change the rotation behaviors (Fig. 4.4). It can be attributed to the ultrahigh dopant concentration of 1×10^{19} cm^{-3} of the Si wafer, which corresponds to a carrier concentration 6 orders of magnitude higher than that induced by the laser excitation (1.8×10^{13} cm^{-3}) as shown in the calculation in Appendix A. The results further agree with our understanding that the increase of carrier density from

photoexcitation leads to the responsiveness of the mechanical rotation of nanowires. Overall, the balance between the generation of photoexcited carriers and recombination, as well as the surface depletion effect explain the observation of the general similarity of rotation spectra of nanowires made from silicon wafers with resistivity from 0.6 Ω cm to over 5000 Ω cm, as well as the vanishing of the optical response in highly doped silicon nanowires with a resistivity of 0.001-0.005 Ω cm.

By utilizing the above modeling, we can also understand the dependence of electric rotation spectrum on lengths and diameters of nanowires with laser exposure, as previously shown in Fig. 4.2b-c. Here, the same diameters and lengths of nanowires in experiments are adopted in the modeling. The electric conductivity of nanowires under laser exposure is set as 0.14 S m^{-1} for all lengths, which is obtained from the above fitting. Here, we can consider that the photoconductivity of a nanowire is independent on the length of a nanowire when it is much longer than the wavelength of the laser. In our experiments, the shortest nanowire is 5 μm in length, around 10 times of the excitation light wavelength. Only high order optical coupling modes exist along such nanowires, which has negligible influence on the light absorption. For nanowires with a fixed diameter of 500 nm and varied lengths from 5 μm to 15 μm, the electro-rotation spectra are simulated as shown in Fig. 4.5c. The results clearly show the monotonic red-shift of the peak frequency of co-field rotation with the increase of the length of a nanowire, accompanied with the attenuation of the magnitudes of the peak speeds in both directions, which agrees well with the dependence observed in experiments in Fig. 4.2b.

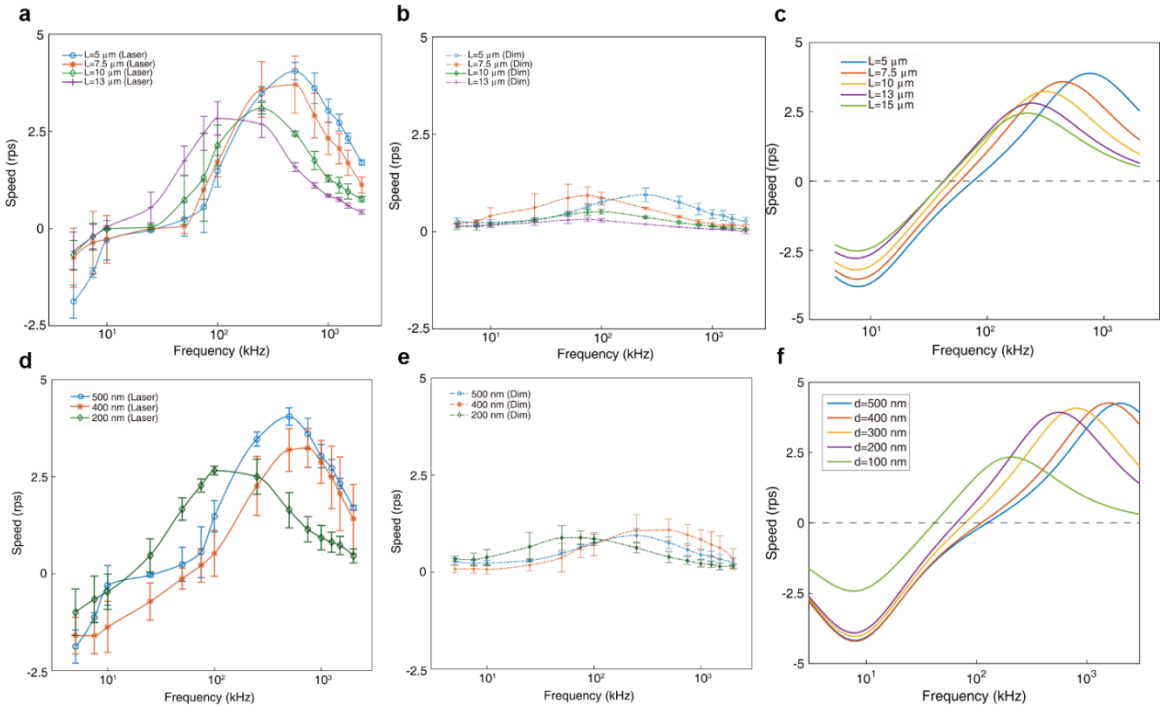

Figure 4.5. Experimental and modeling results of rotation spectra of nanowires with different dimensions in an AC electric field. (a-b) Bright and dim spectra in Fig. 4.2b with full error bars. (c) Theoretical calculation of the rotation spectra of nanowires with a fixed diameter of 500 nm and different lengths from 5 to 15 μm under 127 mW cm^{-2} 532 nm laser exposure. (d-e) Bright and dim spectra in Fig. 4.2c with full error bars. (f) Theoretical calculation of rotation spectra of nanowires with a fixed length of 5 μm and diameters of 100-500 nm under 127 mW cm^{-2} 532 nm laser.

The modeling of the diameter dependence is more complex, since the absorption cross section (ACS) of nanowires exposed to 532 nm laser depends on the diameter in the range of 100 nm to 500 nm. It results in varying photoconductivities among nanowires with different diameters as shown in Table S2. With the consideration of the varying photoconductivity, we can obtain the diameter-dependent simulation as shown in Fig. 4.5f. It shows a general trend that the peak frequency of co-field rotation red-shifts and the magnitude of peak speed decreases with the reduction of the diameter of a nanowire, which

is similar to that observed experimentally in Fig. 4.2c. Considering simulation and experimental results of both the length and diameter dependence, we can find that the aspect ratio of a nanowire plays the key role. Generally, the higher the aspect ratio, the lower the peak frequency and the magnitude of peak speed.

d (nm)	ACS (μm^2)	G (s^{-1} cm^{-3})	Δn (cm^{-3})	σ (S $m^{-1}1$)
500	0.99	3.5×10^{21}	$\sim 1.8 \times 10^{13}$	~ 0.14
400	0.95	5.1×10^{21}	$\sim 2.0 \times 10^{13}$	~ 0.15
300	0.54	5.2×10^{21}	$\sim 1.5 \times 10^{13}$	~ 0.12
200	0.44	9.5×10^{21}	$\sim 1.9 \times 10^{13}$	~ 0.15
100	0.15	1.3×10^{22}	$\sim 1.3 \times 10^{13}$	~ 0.10

TABLE 4.2. OPTICAL AND ELECTRICAL PROPERTIES OF NANOWIRES WITH DIFFERENT DIAMETERS OBTAINED BY SIMULATION AND CALCULATION

In the above analysis, we carefully omitted the light induced heating effect around the Si nanowires, since the change of temperature under 127 mW cm^{-2} laser is less than 10^{-4} K over 100 seconds as shown by the numerical simulation by COMSOL (Appendix A). Thus, it is reasonable to neglect both temperature and viscosity changes in the experiments. Furthermore, it is interesting to note that besides the feasible application in DI water, the opto-reconfigurable effect of nanowires can be applied in low concentration ionic solutions, *e.g.* 1- 10 ppm NaCl solutions, as shown in Fig. 4.6. The nanowire can still rotate and get modulated by light in 1 ppm NaCl solution. The spectra are shown in Fig. 4.6a and are similar to those in DI water, with slight decrement in amplitude. In 10 ppm NaCl, rotation speed is greatly reduced but the laser can still modulate the rotation before the nanowire attaches to the substrate. Here, we successfully accelerated the rotation of

nanowire from 0.20 to 0.71 r.p.s. at 750 kHz when the laser is on (Fig. 4.6 inset). We did not obtain a complete rotation spectrum in 10 ppm or in higher concentration solutions, since nanowires attach to the substrate in a short time at these conditions. The attachment issue can be attributed to the reduction of electrostatic forces between nanowires and substrates in ionic solutions, which is a problem generally exists.

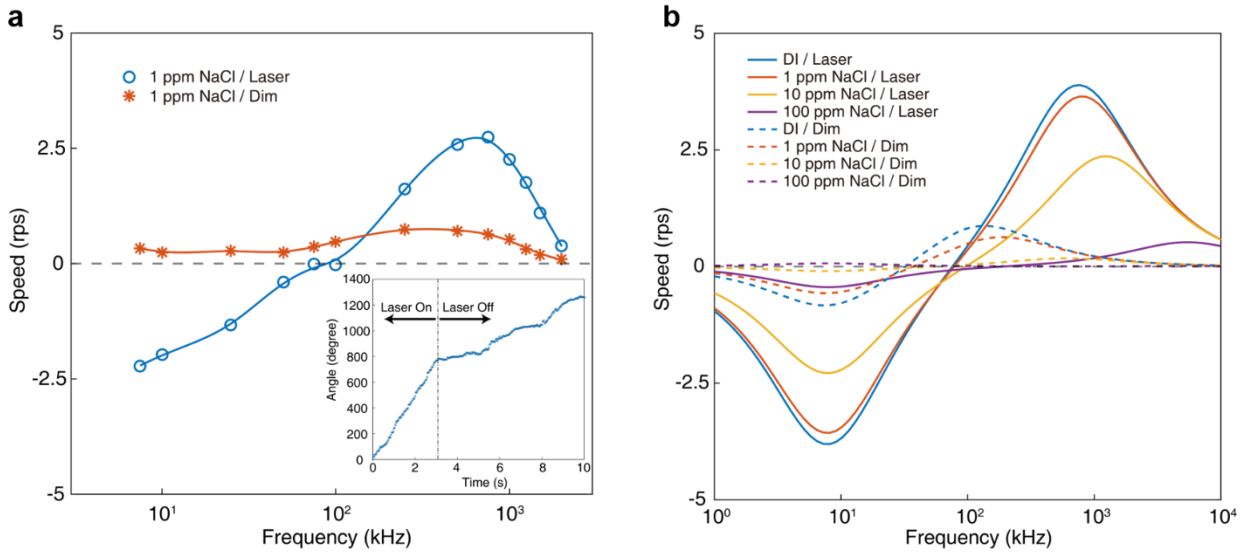

Figure. 4.6. Experimental and simulation results of the bright and dim rotation spectra of intrinsic silicon nanowire (r=500 nm, L= 5 μm) in solutions with various ionic strengths. (a) Experimental results of rotation spectra of nanowires in 1 ppm NaCl solution. Inset: The rotation angle versus time showing optical modulation of the rotation in 10 ppm NaCl solution. (b) Theoretical calculation of the rotation spectra of nanowires in various solutions under 127 mW cm^{-2} 532 nm laser.

The second effect that limits the applications in ionic solution can be understood by the Maxwell-Wagner relaxation. We simulated rotation spectra with different NaCl concentrations, which correspond to different medium conductivities. As the medium conductivity increases, the peak frequency blue-shifts and the peak speed dramatically decreases, when the concentration increases to 100 ppm. In the experimental frequency range of 5 kHz to 2 MHz, the Brownian motions can overwhelm such rotation. The optical

stimulation can greatly increase the manipulation efficiency and reconfigure nanowires on demand when in such ionic mediums compared to those without light.

4.3. Dynamic Reconfigurable Rotation of Si Nanowires Gated by White Light

Silicon has a broad band absorption in the visible light region. Although all the aforementioned reconfigurable rotation of Si nanowires is demonstrated by monochromatic lasers from 532 nm to 785 nm. It may not be necessary to use lasers to induce the desired opto-reconfigurable rotation of Si nanowires. Here we tested the application of white light generated by a computer controlled commercial projector to dynamically reconfigure the rotation of Si nanowires.

We customized an inverted optical microscope by equipping it with a commercial light projector (BenQ MW519) as the light source and a 6.5 mm fisheye lens (Opteka) placed above the microelectrodes for light focusing as shown in Fig. 4.7a. The microelectrodes are placed in the focal plane of the fisheye lens. The commercial projector is operated with a digital light processing (DLP) system with 1280×720 pixel in resolution. We can readily design and project any colors and patterns of light to the nanowires with a resolution of $2\ \mu m \times 2\ \mu m$ per pixel. Here, we simply project a uniform monochromic rectangle, covering the entire central area of the microelectrodes and use a grayscale spectrum from 0 to 255 to adjust the illuminance, where 0 refers to a completely dark image and 255 refers to the maximum illuminance.

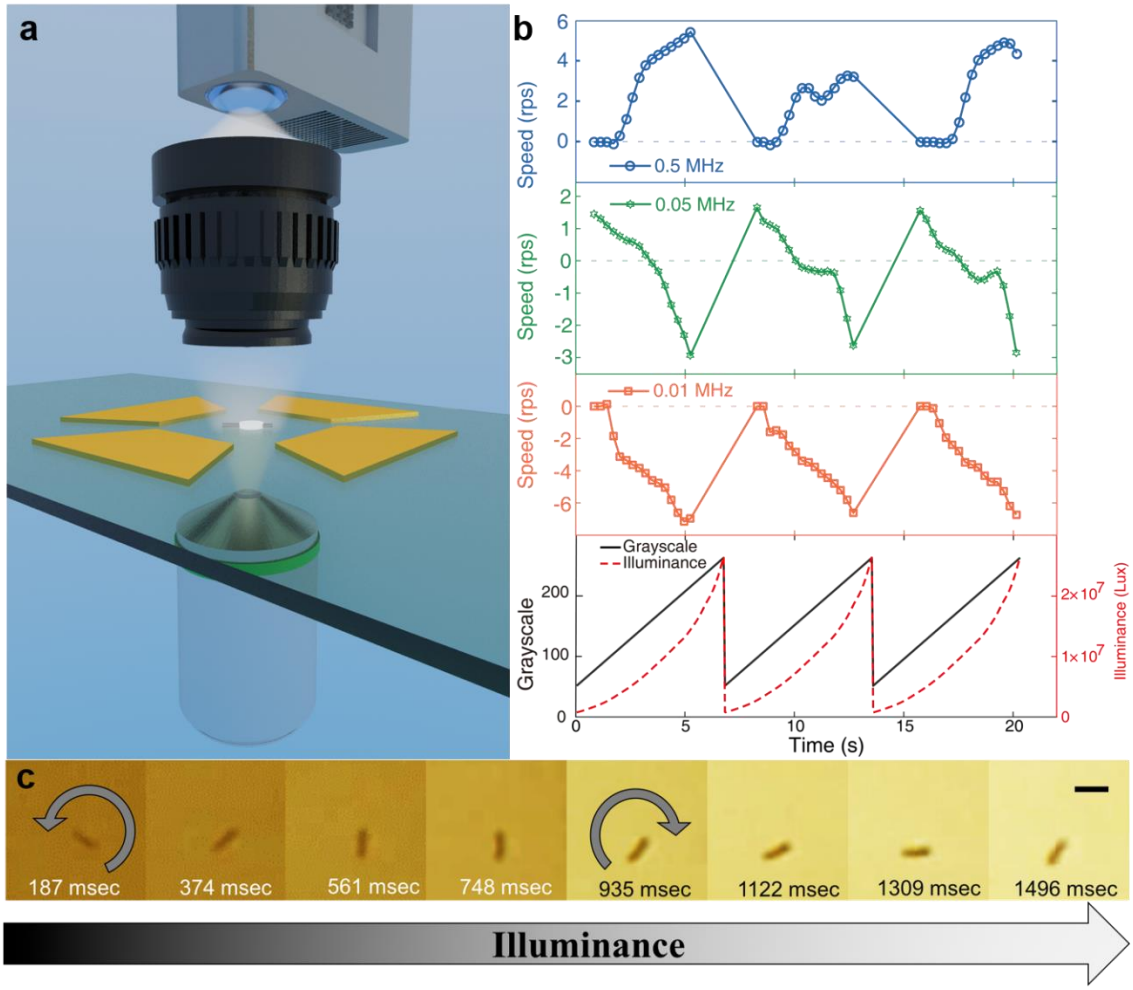

Figure 4.7. Computer programmable white light for reconfiguration of the silicon nanowire rotation. (a) Schematic of the white-light projection system. (b-e) Rotation speed of nanowires versus light illuminance at three different AC frequencies. (b) Acceleration in both co-field and (d) counter-field rotation, (c) reversal of rotation; (e) corresponding illuminance as a function of pixel grayscale set to the projector. (f) Snapshots of rotation reversal with increase of illuminance (green curve in c, 0.05 MHz, 20 Vpp). Scale bar, 5 μm.

We increased the grayscale of the projected image from 50 to 255 at a constant rate of 30 grayscale values per second, repeated, and recorded the rotation behaviors of Si nanowires simultaneously. The illuminance as a function of grayscale is non-linear and shown in Fig. 4.7e. Three different rotating AC fields at 0.5 MHz, 0.05 MHz and 0.01 MHz

are applied. We observed all four types of reconfigurations of rotation of Si nanowires, including acceleration, deceleration, and reversal of chirality of co-field rotation, and acceleration of counter-field rotation as shown in Fig. 4.7b-d. The rotation speed versus the grayscale (illumination) of the light pattern repeated for three cycles is obtained at each AC frequency. At 0.5 MHz, the speed of the co-field rotation gradually increases with the grayscale (illuminance) (Fig.4.7b). At 0.05 MHz, the nanowire begins with a co-field rotation in dark (grayscale 50), decreases to zero in speed, and then reverses the rotation direction when the grayscale (illuminance) further increases (Fig. 4.7c and f). At 0.01 MHz, the nanowire begins with a counter-field rotation in dark (grayscale 50) and increases in speed with the increase of grayscale (illuminance) (Fig. 4.7d). All types of reconfigurable rotations are repeated instantly by cycling the projected light patterns. Thus, plain white light can be used to dynamically reconfigure rotation of Si nanowires.

4.4. Distinguish Metal and Semiconductor Nanowires in a Mixture

Finally, we applied this innovative opto-reconfiguration technique to distinguish metallic and semiconductor nanowires in a non-contact and non-destructive manner. Our experiments and analysis discussed above clearly show that the optical reconfigurable rotation of semiconductor Si nanowires originates from the photoconductive effect in semiconductors. While, for metallic nanoparticles, with much higher density of electrons compare to that in semiconductors, the illumination cannot change their electric conductivity. With this understanding, we demonstrated the application in distinguishing metallic and semiconductor nanowires by a plain optical stimulation in a rotating *E*-field. For a proof of concept, we mixed intrinsic silicon nanowires with gold nanowires in the same suspension in the test. It is difficult to distinguish the metallic and semiconductor

nanowires with bright-field optical microscopic imaging. However, when we subject the nanowires to 5 kHz rotating AC fields and periodic illumination of 532 nm laser at $32\ \mathrm{mW\ cm^{-2}}$, distinct behaviors are found for metallic and semiconductor nanowires. The semiconductor Si nanowires show periodic changes in rotation synchronized with the laser illuminance, and metallic nanowires rotate at constant speeds with no response to the laser as shown in Fig. 4.8a, b. For silicon nanowires, various optical responses can be observed including acceleration, deceleration, reversal rotation as well as stopping depending on the geometries and electrical properties. Though the reconfiguration of the Si nanowires can be different, and some is hard to distinguish from fluctuations caused by Brownian motion, after taking Fourier analysis of the plot of angle versus time, it is straightforward to identify silicon nanowires by the existence of a peak at the illumination frequency (1/6 Hz in Fig. 4.8d). While the spectrum for gold nanowire is flat through all frequencies with no obvious peaks. In this way, we can readily determine the semiconductor Si nanowires and metallic Au nanowires in the same suspension with high accuracy. Based on this working principle and with further technical development, identification of materials with less distinction could be achieved. For instance, semiconductor nanomaterials with different band gaps and absorption spectra could be distinguished by observing and analyzing their rotation behaviors in electric fields under light stimuli of a series wavelengths.

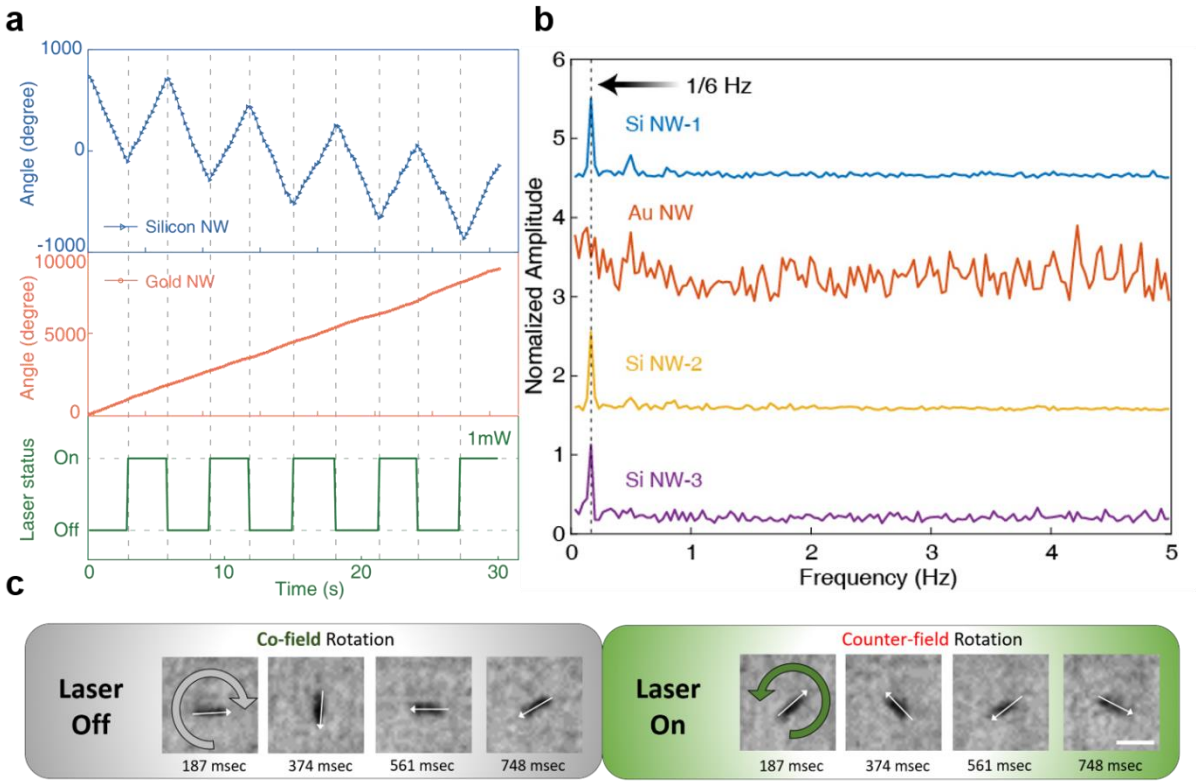

Figure 4.8. Different responses in rotation of semiconductor and metallic nanowire under laser stimuli in electric fields. Angle versus time of (a) silicon and (b) gold nanowires. (c) Laser of 32 mW cm^{-2} 532 nm is on and off periodically. (d) Fourier analysis of rotation angle increment per frame. All amplitudes are normalized. The peaks at 1/6 Hz, same as that of the periodic laser stimuli, are only found in silicon nanowires. (e) Snapshots of a silicon nanowire: distinct rotating behavior when laser is on or off. Scale bar, 5 μm.

4.5. Discussion

In the work, we discovered a new working mechanism that can readily reconfigure mechanical motions of semiconductor nanowires including acceleration, deceleration, stopping, and reversal of rotation merely by controlling the external light intensity in an electric field. This finding can be considered as a mechanical analogy of field-effect transistors gated by light. We understood the working mechanism with both theoretical

analysis and numerical simulations, and successfully demonstrated its application in distinguishing semiconductor from metal nanowires in the same suspension. With this discovery, potentially, various nanoentities, devices, and even biological cells could be equipped with mechanical responsiveness and multifold reconfigurability with functionalized semiconductor elements, changing their motion paradigms from passive to dynamic. Individually controlled micro/nanomachines amidst many could be achievable, which couple and reconfigure their operations instantly. This research could open up many opportunities for interdisciplinary fields, including reconfigurable optical devices, NEMS, nanorobots, nanomachines, communication, tunable molecule release, nanoparticle separation, and microfluidic automation.

Chapter 5: Light Programmable Micro Stepper Motors

The optical tunable real-part (in-phase) polarization broadly impacts multiple distinct and more applicable types of electric manipulations, compared to that governed by the imaginary-part polarization. Implications of changing the real part of the polarizability include refining at least three important manipulation phenomena directly relate to the real part polarization — electro-alignment (studied in this work), dielectrophoresis (transport of particles with electric field gradient), and the chaining effect (particle-particle interactions). Study in this work will prepare a foundation for the improved controllability of these different types of manipulations, which can be exploited for an array of applications, such as light-tunable cargo transport and delivery, position-specific assembly, and collective operations of micro/nanorobots.

Electro-alignment is a type of mechanical alignment motion of longitudinal particles under an AC electric field. Here, we report our study of the light effect on the electro-alignment of silicon nanowires. When illuminated with visible light, a nanowire can be toggled between different alignment speeds and orientations. The switchable manipulation is instant, robust, and programmable, and can be programmed to communicate words in Morse code. Theoretical analysis and numerical simulation are carried out to unveil the underlying physical mechanism, which is attributed to the light tunable in-phase (or real part) electric polarization of semiconductor nanoparticles in suspension. The simulation results agree with experiments qualitatively. With the obtained understanding, we propose and successfully realize the first light switchable functionalized stepper micromotor with great improvement in performance compared with previously reported micro stepper motors[88]. With designed light patterns projected by a digital light processing system (DLP), nanomotors demonstrate independent mechanical operations amidst neighbors in the same electric field.

5.1. Optically Tunable Alignment of Silicon Nanowires in AC Electric Field

When placed in an AC electric field in the range of several kilohertz to megahertz, silicon nanowires can be readily aligned in response to the electric field. This effect has been observed in longitudinal particles and is known as electro-alignment.[61] However, different from previous works, for Si nanowires, which normally align parallel to the applied electric field across a broad range of AC frequencies, we also observe perpendicular alignment to the electric field in a narrow range of frequencies in deionized water. Moreover, when illuminated with laser (532 nm), the alignment torques on silicon nanowires change remarkably, resulting in accelerated alignment speed and even switching between the parallel and perpendicular directions. We have successfully switched the alignment of one single Si nanowire between the two directions for hundreds of times, which, however, is not the limit as long as a wire maintains its position between the electrodes. This switchable manipulation has been observed for the first time. To understand this effect, we carry out a series of experiments, characterize the behaviors, and conduct theoretical analysis with numerical simulation.

By sweeping the AC frequency at an electric field of $1200\ \mathrm{V\ cm^{-1}}$ (15 Vpp), and toggling the laser on and off, we obtain the alignment behaviors of Si nanowires at different frequencies with (red curve) and without laser (blue curve) in Fig. 5.1a. The alignment rate is measured and calculated as previously mentioned in Chapter 2. Here, a minimum LED illumination (white light ~500 lux) is used as background lighting to record motions of nanowires when there is no laser. A 532-nm laser at an intensity of 32 $\mathrm{mW\ cm^{-2}}$ is used to illuminate nanowires together with the dim LED to obtain the laser-induced alignment behaviors in the red curve.

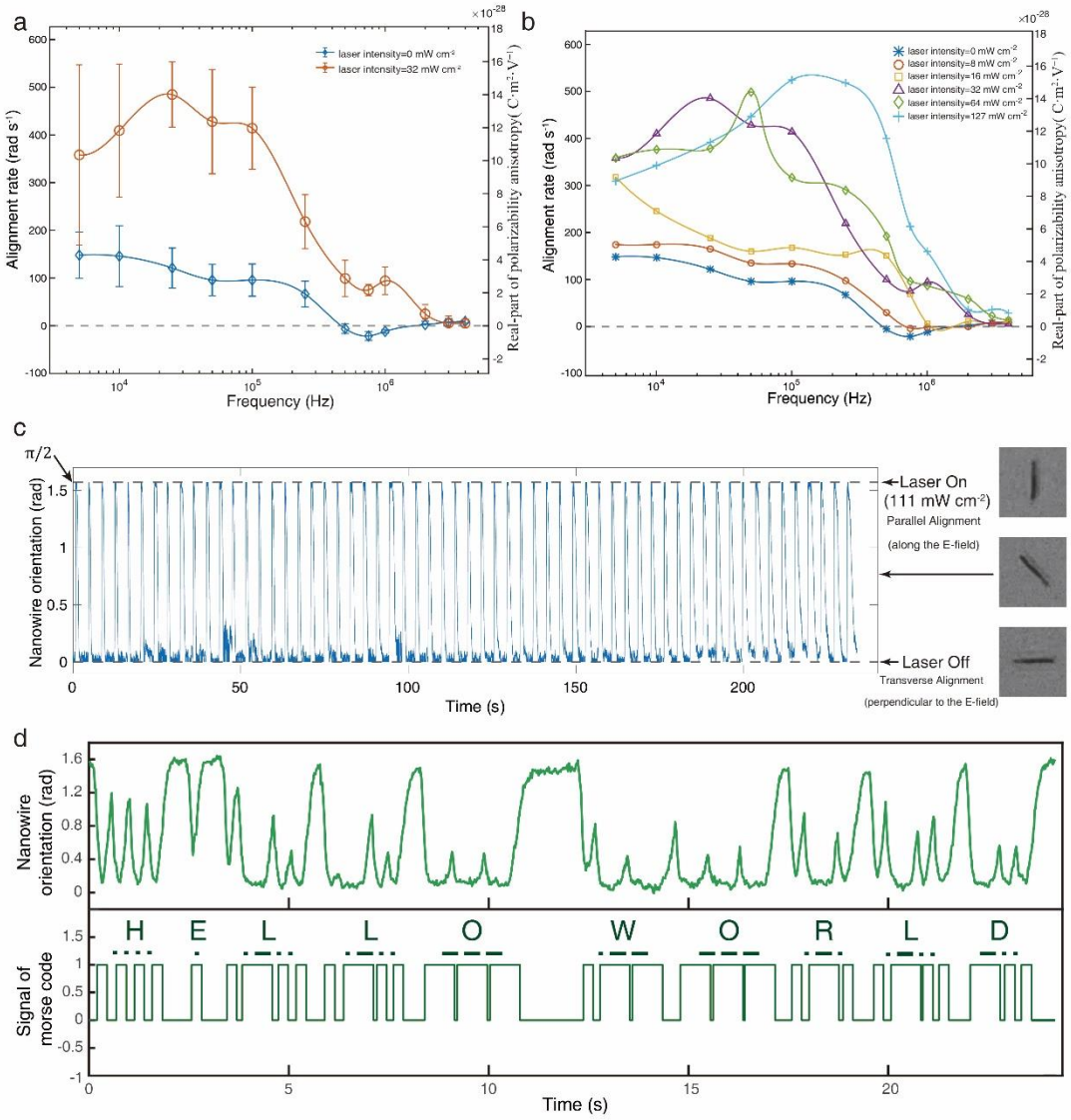

Figure 5.1. Light-responsive alignment of Si nanowires. (a) Alignment rate versus AC frequency of silicon nanowires (undoped; length, 10 μm; diameter, 500 nm) in the dim condition and under 532-nm laser illumination. (error bars are defined as s.d., source data are provided in a Source Data file) (b) Intensity effect of laser on alignment rate versus AC frequency. The corresponding anisotropy of polarizabilities are shown on the right axes, and the eye-guiding lines in (a) and (b) show trends. (c) Cyclic switch between parallel and transverse alignment of a single nanowire with on/off of a 532 nm laser. The electric field direction is defined as $\pi/2$ and its transverse direction is defined as 0. (d) Toggling of a single nanowire in response to a light signal encoded by Morse code (top) and the corresponding interpreted words "HELLO WORLD" from the mechanical motions of the nanowire (bottom).

With the minimum background LED light and no laser exposure, the frequency dependent alignment of a nanowire can be categorized into three regimes: (1) In the low frequency regime from 5 kHz to 500 kHz, nanowires align parallel to the applied electric field with a maximum alignment rate of 150 $\mathrm{rad\,s^{-1}}$ at 5 kHz. The rate gradually decreases with AC frequency with a steep drop at around 100 kHz; (2) In between 500 kHz and 1 MHz, the nanowires are aligned perpendicular to the electric field; 3) When the AC frequency further increases to above 1 MHz, the nanowires return to the parallel alignment at a low rate below 10 $\mathrm{rad\,s^{-1}}$. In contrast, when the 532-nm laser is illuminated on the silicon nanowires, dramatic changes of the alignment behaviors, including acceleration and even switching of direction are observed. For instance, at 5 kHz, light illumination greatly increases the alignment rate by 2.4 folds from 150 $\mathrm{rad\,s^{-1}}$ to 360 $\mathrm{rad\,s^{-1}}$. The maximum alignment rate increases to 487 $\mathrm{rad\,s^{-1}}$ occurring at 25 kHz, which is almost four times that of the same frequency without laser. As the frequency further increases, the alignment rate decreases rapidly at about 250 kHz and verges to zero at 4 MHz. Overall, laser exposure increases the positive alignment rate at all frequencies, blue-shifts the frequency where the highest alignment rate occurs, and changes the transverse alignment to parallel alignment at the tested frequencies.

To further understand the observed light-controlled switching behaviors of Si nanowires, we monotonically vary the laser intensity from 8 $\mathrm{mW\,cm^{-2}}$ to 127 $\mathrm{mW\,cm^{-2}}$ and measure the alignment rate as shown in Fig. 5.1b. For instance, at 5 kHz, the alignment rate increases with laser intensity up to 32 $\mathrm{mW\,cm^{-2}}$, then maintains an approximate plateau to 64 $\mathrm{mW\,cm^{-2}}$, before decreasing at 127 $\mathrm{mW\,cm^{-2}}$. The observed decrease of alignment rate under stronger laser stimulus will be further studied and discussed in the following with simulations. In general, the maximum alignment rate among all tests increases with laser intensity and the corresponding peak frequency exhibits a monotonic

shift from 5 kHz at 0-16 $\mathrm{mW\ cm^{-2}}$ to 100 kHz at 127 $\mathrm{mW\ cm^{-2}}$. The amplitude of the negative alignment rate decreases with laser power up to 16 $\mathrm{mW\ cm^{-2}}$, above which the transverse alignment switches to parallel alignment. In order to provide more insights, we also calculated the corresponding anisotropy of polarizability of nanowires as shown in Fig. 5.1a, b (axes on the right).

5.2. Modeling of the Optically Tunable In-Phase Electric Polarization of Silicon Nanowires

To obtain a more qualitative understanding of the observed optically controlled alignment phenomena, we conduct modeling with a method including both analytical and numerical approaches. Related to this work, modeling of the out-of-phase (imaginary part) polarization of semiconductor nanoparticle, has been reported by using either a numerical method[73] or an analytical approach.[65] Different from previous works, here, we focus on the in-phase electric polarization (real part) and leverage the accuracy of numerical simulation and simplicity of analytical approximation to investigate the system.

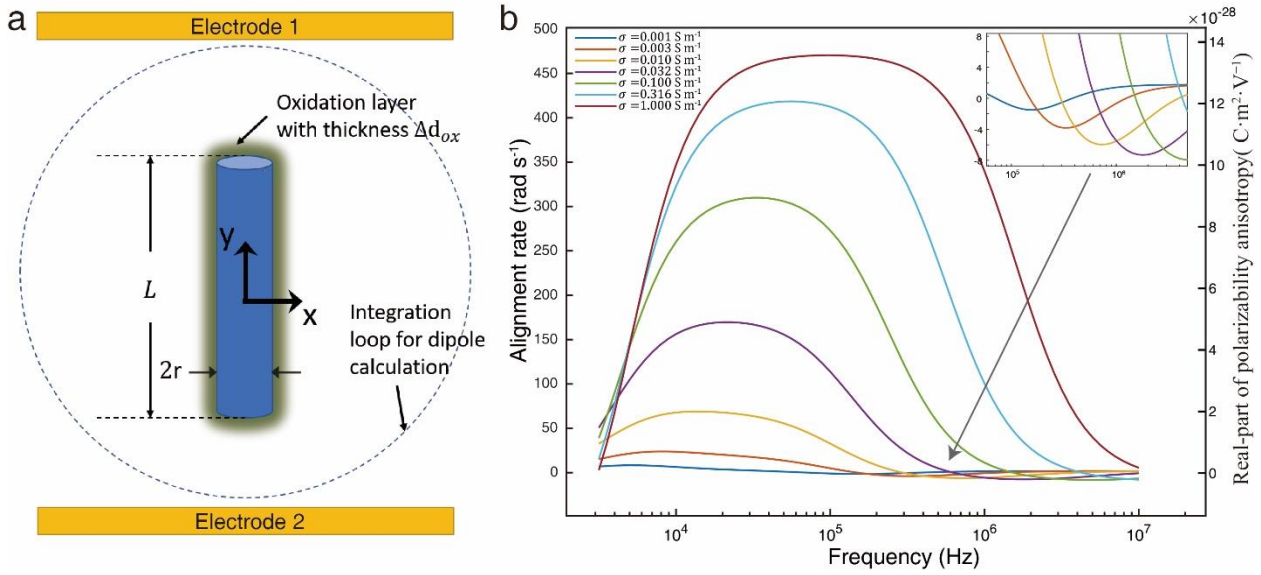

Figure 5.2. Modeling of nanowire polarization and numerical calculation of alignment rate versus AC frequency of a silicon nanowire of $L = 10$ µm and $r = 250$ nm. (a) Model of a silicon nanowire as a cylinder with length L and radius r. An Oxidation shell with thickness $\Delta d_{ox} = 1\ nm$ is considered, shown as the dark shade surrounding the nanowire. (b) Numerical calculation of alignment rate of nanowires of different electrical conductivities versus AC frequency. Inset: Zoom-in image at frequencies with negative alignment rates.

We simulate the alignment rate and the anisotropy of electrical polarizability to compare with the experimental results as shown in Fig. 5.2b. The respective contributions of polarization from Maxwell-Wagner relaxation and electrical double layer are provided in Fig 5.3. In simulation, the maximum alignment rate and peak frequency increase with the electrical conductivity of silicon nanowires, corresponding to the increase of alignment rate with laser intensity in experiments. Importantly, this model also predicts the transverse alignment at ~ 750 kHz when the conductivity of silicon is $1 \times 10^{-2}\mathrm{m}^{-1}$, which agrees with that observed experimentally. As aforementioned, we observed decrease in alignment rate when light intensity increases at low frequencies, *i.e.* 5 kHz. This is also found in the

simulation result: the alignment rate decreases with increase of electrical conductivity in Fig. 5.2b (<5 kHz). We can understand the observed phenomenon with an intuitive physics picture involving the capacitive effect of oxide at low frequencies.

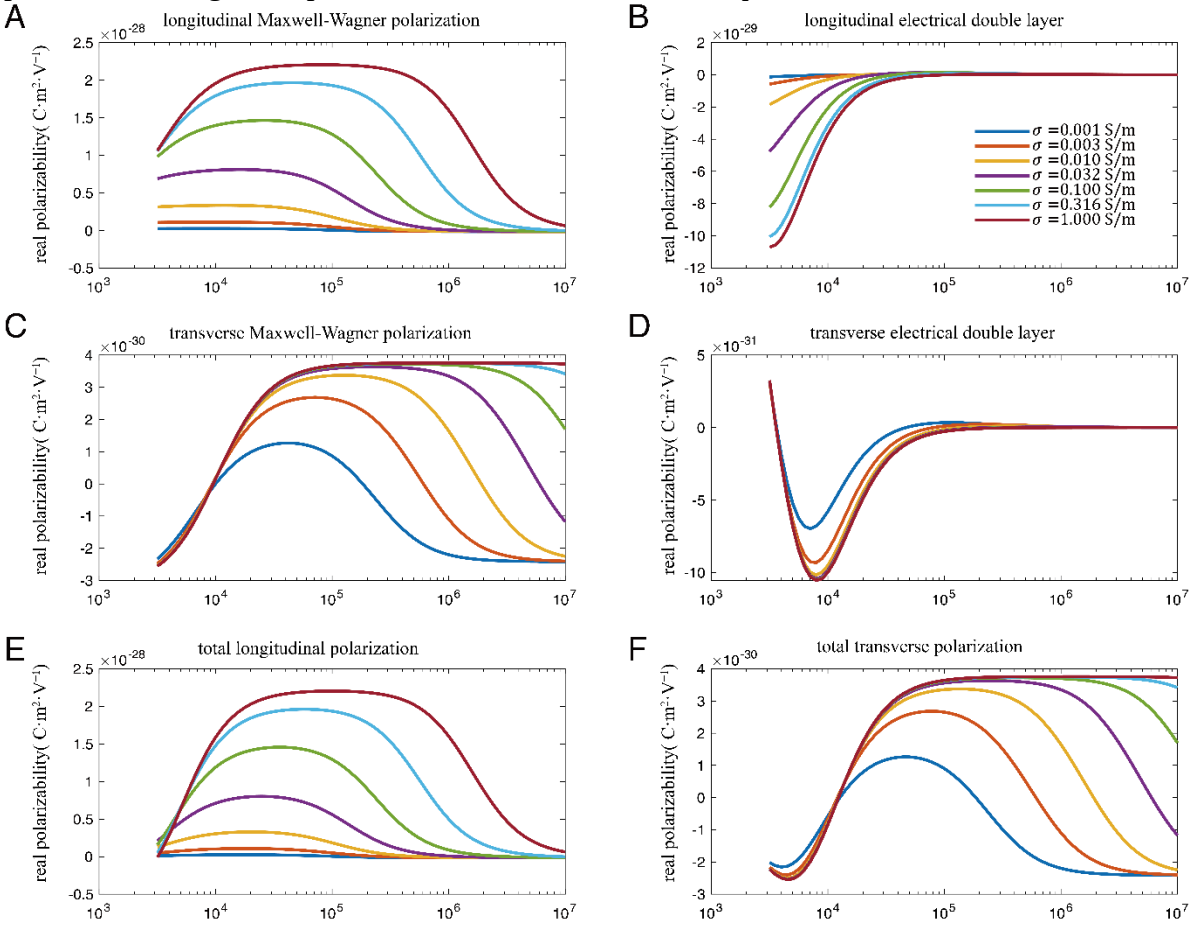

Figure. 5.3. Respective polarizability contribution of the Maxwell-Wagner polarization and the electrical double layer. (A, B) Real part polarizability in longitudinal direction of the nanowire from the Maxwell-Wagner polarization and electrical double layer, respectively. (C, D) Real part polarizability in transverse direction of the nanowire from the Maxwell-Wagner polarization and electrical double layer, respectively. (E, F) Combined real part polarizability from both effects in longitudinal and transverse directions of the nanowire, respectively.

We observed that nanowires stored in water after one day consistently align transversely to a 750 kHz electric field under background light, but there are less wires showing this behavior when tested immediately after being made. This might be due to surface oxidation of the nanowires or other reactions between Si and water. As discussed in our previous work, the surface states generated at the Si-SiO_2 interface change the electrical properties of pure Si nanowires through both depletion and surface recombination processes. The oxidation layer also plays a role with additional capacitance under AC electric field, which would influence the result of Maxwell-Wagner relaxation.

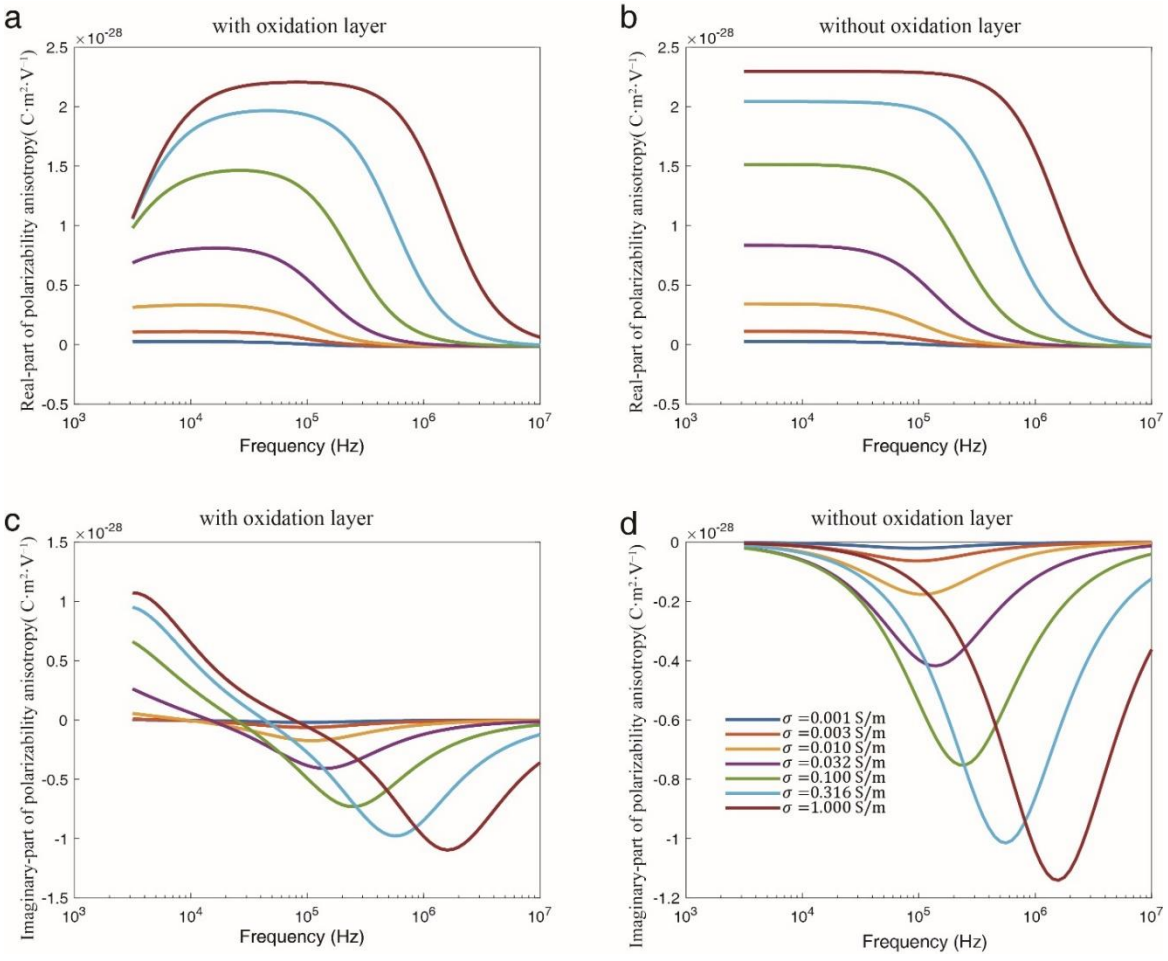

Figure 5.4. Oxidation effect on the Maxwell-Wagner polarization. (A, B) Simulation results of real part polarizability anisotropy from the Maxwell-Wagner polarization with and without considering of a thin oxidation layer on the silicon nanowire surface. (C, D) The simulation results of imaginary part polarizability anisotropy from Maxwell-Wagner polarization with and without considering of a thin oxidation layer on the silicon nanowire surface.

In experiment, we observed decrease in alignment rate when light intensity increases at low frequencies, *i.e.* 5 kHz, and the simulation result also shows decrease in alignment rate with increase of electrical conductivity in Fig. 5.2b (<5 kHz). First, as discussed in the manuscript, the alignment rate is directly proportional to the value of $\mathrm{Re}(\alpha_{\parallel} - \alpha_{\perp})$, at low frequencies, $\alpha_{\perp} \ll \alpha_{\parallel}$, for simplicity, we only consider the polarization in the longitudinal direction of the nanowire ($\alpha_{\parallel}$). As shown in Fig. 5.4, we plot both the real and imaginary parts of the Maxwell-Wagner polarizability of the nanowire. If we model the nanowire made of pure silicon without surface oxidation, then the results are shown in Fig. 5.4B, D. The real part of the polarizability increases as the light intensity increases, and the imaginary part of the polarizability is almost zero at low frequencies. However, once we include a thin oxide layer on the surface of the Si in the model, since Si always has a native oxidation layer, the simulation results as shown in Fig. 5.4A shows a decrease in the real-part polarizability at low frequency (<10 kHz). Meanwhile, the imaginary polarizability increases at low frequencies (Fig. 5.4C). After considering the effect of electrical double layer, the final results show decrease in real polarizability as electrical conductivity increases.

In a more intuitive picture, the thin oxide layer can be regarded as an additional capacitor placed in between the silicon nanowire and the electrical double layer. The dipole moment generated on the silicon nanowire first induces the polarization of the oxide

capacitor, and then induces the EDL polarization. However, the polarization of oxide layer causes additional phase lag, as indicated in Fig 5.4. The norm of the total polarization ($\sqrt{\mathrm{Re(p)}^2 + \mathrm{Im(p)}^2}$) still increases as the light intensity increases, but due to the existence of the oxide capacitance and the resulting additional phase lag, the imaginary part of the polarizability increases greatly, while the real part slightly decreases.

However, there is also discrepancy between simulation and experimental results. With the increase of the electrical conductivity resulted from light illumination, the simulation result shows that transverse alignment exhibits a monotonically increase of alignment rate and a blue-shifted peak frequency. This differs from our experimental results, where the transverse alignment vanishes when the laser intensity is higher than 16 mW cm^{-2}, and requires further investigation.

5.3. Light Programmable Synchronous Stepper Micromotors

With the understanding of the optically tunable electro-alignment of semiconductor nanowires, we propose an innovative light controlled synchronous stepper micromotor. It mimics the macroscopic synchronous stepper motors, which rotates in-phase with an electric field and turn to specific angles on demand. The operation phase of our miniaturized motors can be switched by light. To realize such a micromotor, we generate a high frequency AC electric field ($f_1 = \frac{\omega_1}{2\pi}$) that efficiently aligns a nanowire and rotates this high frequency AC field at a much lower frequency ($f_2 = \frac{\omega_2}{2\pi} \ll f_1$) clockwise, so that the nanowire follows the low-frequency rotating AC field with a continuous synchronous rotation. Such an electric field can be given by:

$$\boldsymbol{E} = \mathrm{E}_0 \cos(\omega_1 \mathrm{t}) \cdot [\cos(\omega_2 t)\, \hat{\boldsymbol{x}} + \sin(\omega_2 t)\, \hat{\mathbf{y}}]. \tag{5.1}$$

We note this driving mechanism of the motor differs from most previous works in which the rotation is a result of the interaction between the high-frequency rotating electric

field and out-of-phase electric polarization of a nanowire.[65,88] Here, an in-phase electro-alignment torque is created and continuously compel the rotation of micromotors[89] with the advantages of precision speed control and angular positioning, synchronism among different motors, and programmable light switching. Specifically, the created stepper micromotor in this report exhibits at least three distinct advantages compared to those in previous works: (1) the time-dependent angular position of a motor can be precisely controlled by the applied E-field, without the use of any imaging feedback. (2) Under proper lighting conditions, all the motors, regardless of their differences in geometry or electrical properties, can be aligned in the same direction synchronously, which makes this mechanism a potential approach to control rotation of arrays of motors at exact same speed under the same field. (3) The alignment field in this work can provide an effective torque to fix the motor's angle when it is stopped, countering the Brownian motion.

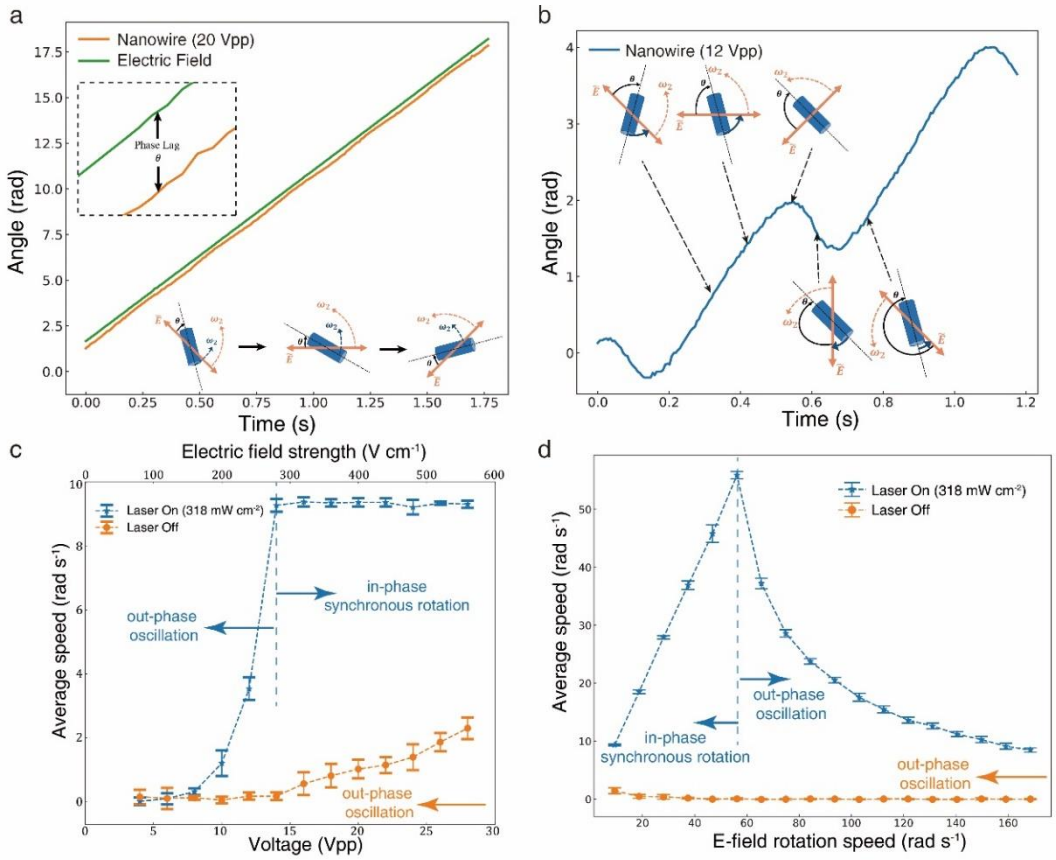

Figure 5.5. Light switchable rotation of a Si nanowire stepper motor. (a, b) Rotation angle versus time of a nanowire at different voltages (or electric field strengths) exposed to 318 mW cm^{-2} 532-nm laser. (a) The electric field rotates at 1.49 Hz (in green). The stepper motor rotates synchronously with the electric field with a phase lag θ, at 20 Vpp (400 V cm^{-1}) (in orange). Inset: The constant phase lag between the driving electric field and the rotating nanowire. (b) It switches to the out-phase oscillation mode at 12 Vpp (240 V cm^{-1}) (more details in Appendix B). Schematics show the relative positions of a rotating nanowire with the electric field at different time. (c) Average rotation speed of a micromotor versus driving voltage/electric field strength with (in blue) and without laser illumination (in orange)The driving electric field is 1.49 Hz, same as that the in-phase rotation of the nanowire. (d) Average rotation speed of a micromotor versus rotation speed of the driving electric field at 30 Vpp (600 V cm^{-1}) with (in blue) and without laser illumination (in orange).

The driving electric field is created by applying four AC voltages as shown in the following equations sequentially on the quadruple microelectrodes in Fig. 3.2:

$$V_{1,3} = \pm V_0 \sin(\omega_1 t)\cos(\omega_2 t)$$
$$V_{2,4} = \pm V_0 sin(\omega_1 t)\sin(\omega_2 t) \quad (5.2)$$

The voltages can be generated via a customized computer-controlled four-channel function generator. In such electric field, we observe that a micromotor always operates in one of two modes, the "in-phase" or "out-phase" modes, depending on whether the alignment torque is enough to overcome the drag. The motor runs in-phase when it rotates at the same rotating speed of ω_2 ("synchronous speed") with the rotating electric field, where the alignment torque satisfies: $\tau_e = -\tau_{drag} = \gamma\omega_2$. As previously discussed, the alignment torque is a function of the angle between the nanowire and the electric field, given by: $\tau_e = -\gamma A \sin\theta \cos\theta$, so the maximum alignment torque τ_e available to drive the motor is $\frac{\gamma A}{2}$, which occurs when the angle between the nanowire long axis and the electric field is $\pi/4$. Therefore, if $\frac{\gamma A}{2} \geq \gamma\omega_2$, the electric field can supply a sufficient torque to power the motor's in-phase rotation as shown in Fig. 5.5a. In particular, the nanowire rotates at an approximately constant angle θ behind the electric field, where θ is termed as the "phase lag" (Fig. 5.5a inset). Otherwise, the alignment torque is insufficient and the nanowire, though rotates, periodically falls behind the electric field resulting in oscillations as shown in Fig. 5.5b. When the motor runs out-phase, it exhibits a net speed, in the same direction but lower than the rotating electric field.

Laser illumination controls the motion of such a micromotor and allows fine control beyond basic electric manipulation. To investigate the optical effect on the rotation of the micromotor, we scan the peak-to-peak voltage from 4 Vpp to 28 Vpp for an electric field rotating at a constant speed of $f_2 = 1.49$ Hz. Without laser exposure, the micromotor always rotates out of phase. While its average speed increases with the voltage, it is always lower than f_2. When excited by a 318 mW cm^{-2} 532-nm laser and the voltage is above

or equal to 14 Vpp, the micromotor switches from the mode of out-phase oscillation to in-phase synchronous rotation at the same speed of the electric field (f_2) (Fig. 5.5c).

We further scan the rotation speed of the electric field (f_2) from 1.49 Hz to 26.82 Hz at a constant voltage of 30 Vpp. Without laser illumination, the micromotor always operates out-of-phase oscillation with nearly zero average speed. With a 318 $\mathrm{mW\,cm^{-2}}$ 532-nm laser stimulation, the motor switches to in-phase synchronous rotation up to 8.94 Hz before losing the synchronism and turning into out-of-phase oscillation (Fig. 5.5d). The characterizations of the performances of the stepper motors in the mode of synchronous operation, such as the pull-out torque and power, are included in the Appendix B. The two operation modes can be switched back and forth with simple control of laser exposure. The performance of the motors is well reproducible (Fig. 5.6) and can be observed for more than a week with gradually increased threshold voltage (Fig. 5.7).

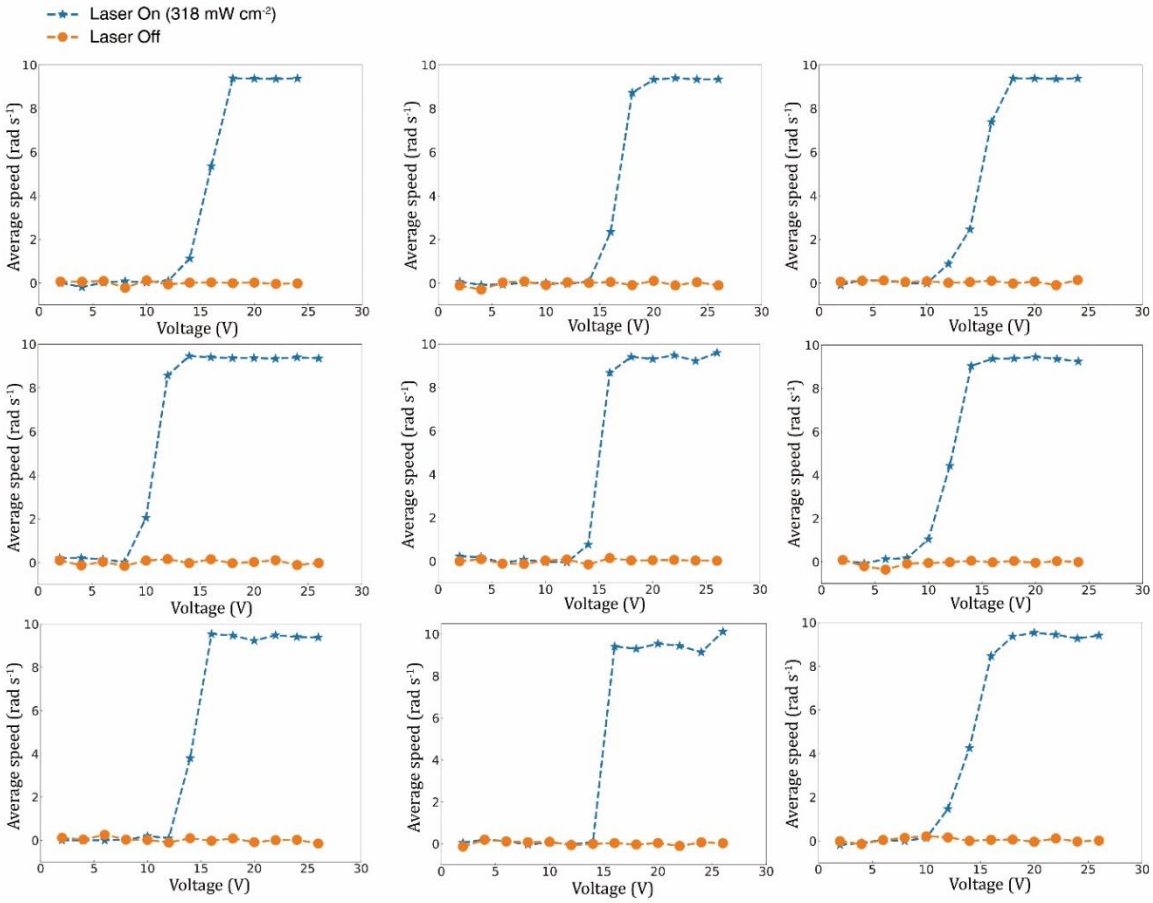

Figure 5.6. Light switchable in-phase and out-phase rotation of a Si nanowire stepper motor. Average rotation speed of a micromotor versus driving voltage with (in blue) and without laser illumination (in orange). The driving electric field is 1.49 Hz, same as that the in-phase rotation of the nanowire.

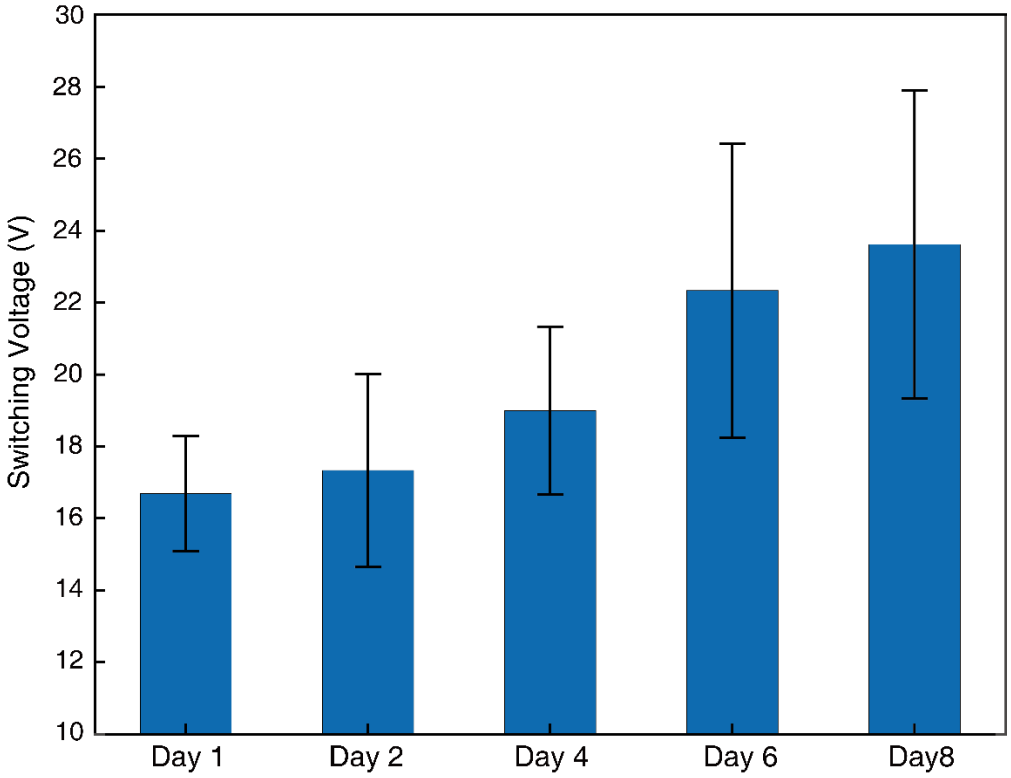

Figure 5.7. Change of switching voltages of nanowires stored in DI water for different days. (error bars represent the standard deviation)

With the unique light responsiveness of the micromotors, we successfully operate micromotors independently and versatilely in the same electric field by projection of localized light spots via a digital light processing (DLP) syste. The DLP system is capable of projecting micro light patterns onto the sample surface with a maximum resolution of 5 μm per pixel. To control two micromotors individually, we programmed two circular laser spots of 70 μm in diameter and each spot covers one of the micromotors without any overlap. A rotating electric field with $f_1 = 100$ kHz, $f_2 = 1.49$ Hz at 13 Vpp is applied as the driving source. When both laser spots are on, both micromotors rotate synchronously at the same speed, as shown in Fig. 5.8a, where the first segments of orange and blue curves

overlap, indicating the synchronous rotation speed of motor 1 and 2. Then the laser spot on motor 1 is turned off. The driving torque on motor 1 is no longer sufficient to maintain the synchronism with the electric field, and the motor 1 steps into out-phase oscillation with a lower average speed (red curve). Next, the laser spot on motor 2 is also turned off; instantly, the motor 2 is switched into out-phase oscillation (purple curve). When both laser spot 1 and 2 are turned on again, both motors restore to synchronous rotation. To the best of our knowledge, this is the first demonstration of microscale stepper motors that can be controlled on individual independently in the same environment. The success is based on modulating the electrical properties of each nanoparticle device instantaneously with external stimuli.

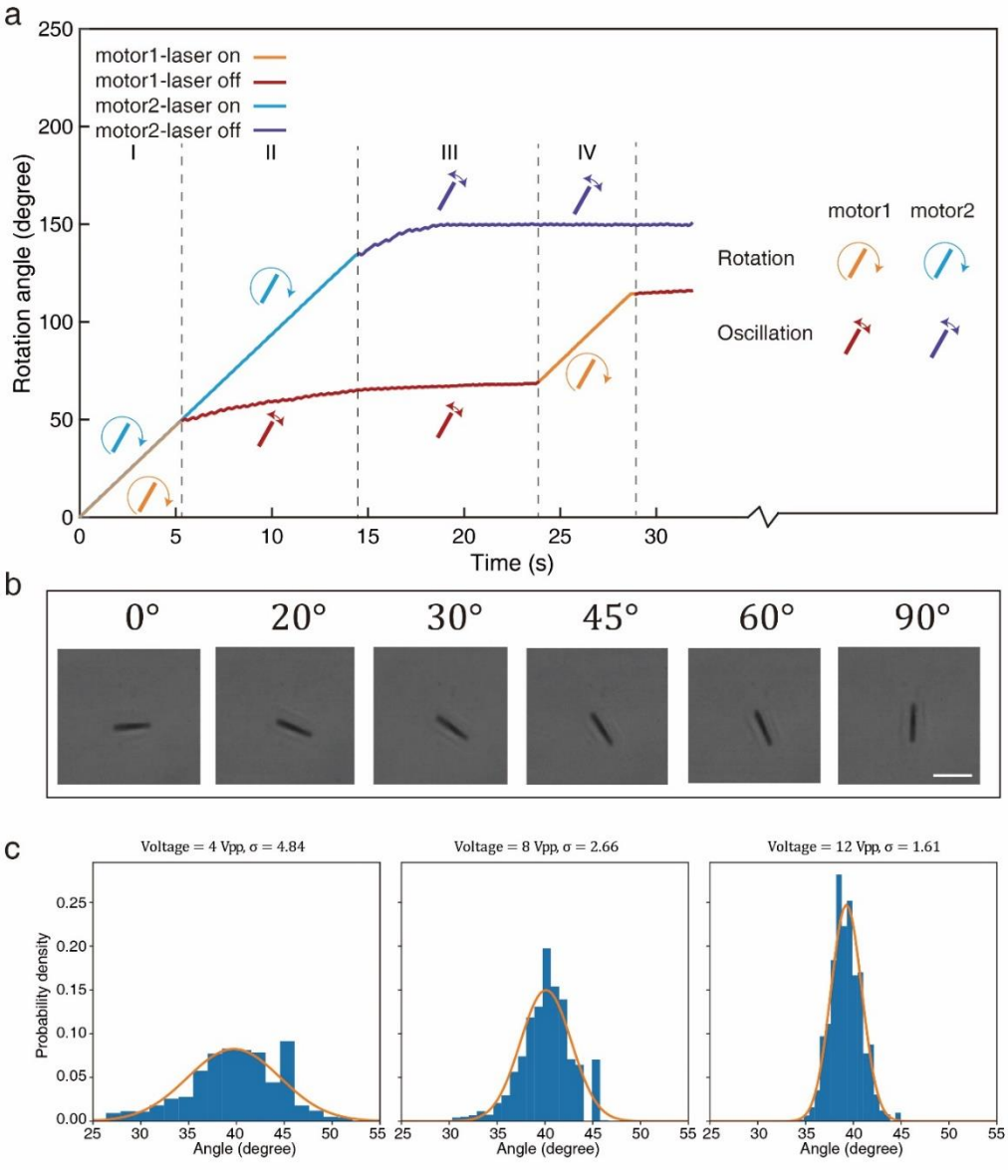
a
motor1-laser on
motor1-laser off
motor2-laser on
motor2-laser off
I
II
III
IV
Rotation angle (degree)
Time (s)
motor1
motor2
Rotation
Oscillation
b
0°
20°
30°
45°
60°
90°
c
Voltage = 4 Vpp, σ = 4.84
Voltage = 8 Vpp, σ = 2.66
Voltage = 12 Vpp, σ = 1.61
Probability density
Angle (degree)

Figure 5.8. (a) Independent control of two stepper micromotors in the same electric field. The micromotors are both driven by a rotating electric field with $f_1 = 100$ kHz and $f_2 = 1.49$ Hz at 13 Vpp. Digital light projecting (DLP) system projects light on each micromotor independently at an intensity of ~50 mW cm^{-2}. (b) Rotation of a micromotor to designated angular positions like a stepper motor by stopping the rotation of the AC electric field at specific angle ($f_1 = 100$ kHz, V = 10 Vpp, laser intensity = 127 mW cm^{-2}), scale bar 10 μm. (c) angle fluctuation around a designated angle at different voltages (frequency = 100 kHz). Probability density is fitted by normal distribution.

Finally, such micromotors can be readily programmed and step to designated angular positions as shown in Fig. 5.8b. Here, the electric field (100 kHz, 10 Vpp, 200 V cm^{-1}) is directed to various angles by continuing its high-frequency component (f_1) but pausing the low-frequency component (f_2) at a designated angle. As shown in equation (2.13), our step motor can provide a restoring force of $\tau_{res} = A(\omega, E_0) \sin\theta \cos\theta$, in which the alignment rate A is a function of AC frequency and the electric field strength. It is obvious that the alignment accuracy increases with the electric field strength and polarizability at an AC frequency. Here we investigate the angle fluctuation of a stepper motor at different voltages as shown in Fig. 5.8c. Under 100 kHz AC E-field, when the voltage increases from 4 Vpp (80 V cm^{-1}) to 12 Vpp (240 V cm^{-1}), the normal distribution of angle of the stepper motor becomes narrower with the standard deviation σ reducing from 4.84 to 1.61 degree.

5.4. Discussion

In summary, we report a versatile working mechanism that can be exploited for developing a new type of efficient visible-light-responsive micro/nanomachines without requirements of chemical fuels, UV light source, or special geometry of nanoparticle building blocks. The electrical property of a semiconductor micromotor can be controlled

solely by intensity of visible light and is exhibited as modulable mechanical alignment in an external electric field. Based on our investigation and understanding, such an effect can be generalized to any types of materials as long as their electrical conductivities can be changed prominently when stimulated by light or any other stimuli. Various types of photoconductive materials may all exhibit such an effect. Here, we demonstrated with the most common type of semiconductor, Si. The specific performance depends on the band structure, carrier lifetime, light wavelengths and intensity, dimension of the particle, and electrical properties of the suspension medium. In terms of other types of stimuli, we consider that materials that change electrical conductivities in magnetic fields, *i.e.* those with high magnetoresistance,[90] could possibly exhibit an analogous effect.

The facile switching mechanism is a new add to the tool box of nanomanipulation techniques, and could offer opportunities that are worth of exploration. For instance, as shown in the demonstration, encoded light signals can be transmitted into alignment oscillations of a single device, which communicates meaningful words in Morse code. The same approach could be potentially explored to develop unique opto-mechanical conversions for complex coupled micro/nanomachines. Moreover, with patterned light from DLP, we successfully demonstrated individually controlled rotary stepper motors in the same field, each can toggle between the oscillation and full-turn synchronous rotation modes, independently. With tunable intensity of light, it is feasible to control each in the pull-out torque and power (Appendix B). Ultimately, it could be attainable to control arrays of stepper micro/nanomotors that exhibit individually controlled performances by dynamic light patterns. The working mechanism could also be exploited for the future micro/nanorobots independently operating for collaborative task forces, and even to control different components within a micro/nanorobots for programmable operations.

In the aspect of fundamental research, the light effect on the real part of the electrical polarization anisotropy has been studied in this work. We investigate the light stimulated electro-alignment behavior of Si nanowires with experimentations, simulations, and demonstrated applications. This work also prepares the foundation for other types of related phenomena, *i.e.* light tunable transport and chaining of particles, and adds the knowledge of the optical effect on the real part of electrical polarizability anisotropy of Si nanowires in aqueous solution.

The presented switchable manipulation is efficient and versatile. However, it is more feasible for on-chip devices than in-vivo applications. Challenges should be addressed in future research, including the oxidation problem that many semiconductors have in aqueous solution, and the compatibility with complex media.[91,92] More sophisticated materials design should be considered to replace the simple wires for useful applications. The full potential of this technique will also be helped by advanced optical projection devices with high resolution and large projection area, as well as sophisticated programming of light projects to equip automation[93] and intelligence to the manipulation. Overall, this work suggests new opportunities in nanorobotics research, in both the fundamental and application aspects.

Chapter 6: Light Guided Dielectrophoresis

In this section, we propose an orignal manipulation method that can compel micropaticles with multimode linear locomotion and simultanously controlled alignment. The working mechanism is based on the complex interactions of light, electric fields, and semiconductors. The proposed mechanism is based on systematic calculation and simulation. The results provide a guidance on how to utilize light to modulate DEP forces applied to silicon microparticles of various geometries to select their different actuation modes. To be noticed, the proposed mechanism differs from the optoelectronic tweezers, although they both involve a photoresponsive semiconductor material with conductivity change upon local light illumination.

The optoelectronic tweezers utilize the light-induced photoconductivity change in the a:Si substrate to locally modulate the electrical field intensity and gradient for DEP generation.[94] Distinctly, our approach does not affect the distribution of the electrical field, but the polarizability of the particles being fine tuned by light intensity. A successful implementation of the proposed approach could enable a new class of micromachines with rarely found individually-controllable locomotion in a swarm. This work could also be applied towards the separation and purification of optoelectric microparticles with similar electric conductivities in dark but different geometries.

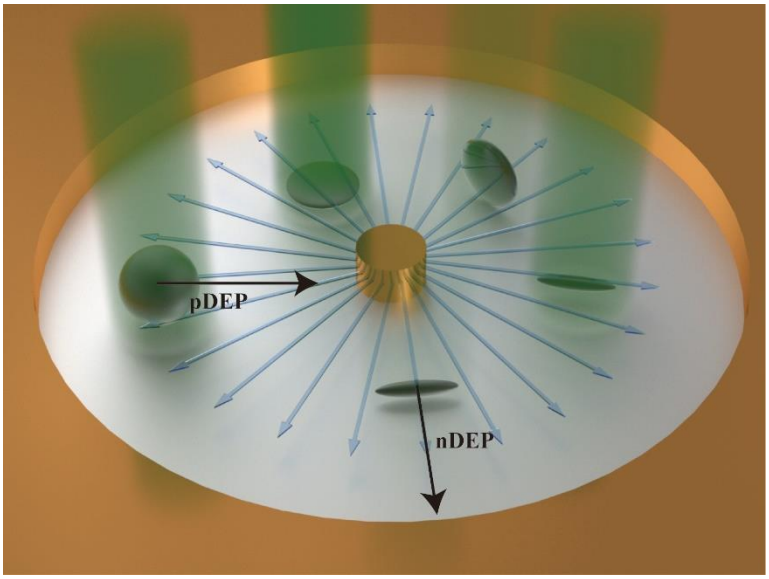

Figure 6.1. Schematic of light-guided dielectrophoretic propulsion of silicon microparticles of different geometries and numerical simulation of electric-field distribution. For example, a pair of concentric circular microelectrodes with inner and outer electrodes generates a non-uniform AC field (as indicated by the blue arrows). Silicon particles of various geometries in deionized (DI) water are propelled by the light-controlled DEP forces. Light patterns projected onto individual particles excite photogenerated carriers and results in increase of the conductivity of the particle, so that both the direction and magnitude of the DEP forces can be tuned.

6.1. Dependence of Electric Polarization on AC Frequency, Geometry and Conductivity of Si Particles

We begin our investigation of the dependence of the Maxwell-Wagner polarization, which is the major contribution of the total electric polarization across all frequencies on the AC frequency, geometry, and conductivity of a Si particle. The real part of K can be written in the following form derived from equation (2.11):

$$\mathrm{Re(K)} = \frac{\varepsilon_2 - \varepsilon_1}{3\varepsilon_1 + 3(\varepsilon_2 - \varepsilon_1)L} + \frac{\frac{\sigma_2 - \sigma_1}{\sigma_1 + (\sigma_2 - \sigma_1)L}[\varepsilon_1 + (\varepsilon_2 - \varepsilon_1)L] - (\varepsilon_2 - \varepsilon_1)}{[\varepsilon_1 + (\varepsilon_2 - \varepsilon_1)L](1 + \frac{[\varepsilon_1 + (\varepsilon_2 - \varepsilon_1)L]^2}{[\sigma_1 + (\sigma_2 - \sigma_1)L]^2}\omega^2)} \qquad (6.1)$$

By defining the Maxwell-Wagner charge relaxation time as $\tau_{MW} = \frac{\varepsilon_1+(\varepsilon_2-\varepsilon_1)L}{\sigma_1+(\sigma_2-\sigma_1)L}$, equation (6.1) can be written as:

$$\mathrm{Re}(K) = \frac{\varepsilon_2 - \varepsilon_1}{3\varepsilon_1 + 3(\varepsilon_2 - \varepsilon_1)L} + \frac{(\sigma_2 - \sigma_1)\tau_{MW} - (\varepsilon_2 - \varepsilon_1)}{[\varepsilon_1 + (\varepsilon_2 - \varepsilon_1)L](1 + \tau_{MW}^2\omega^2)} \tag{6.2}$$

The low-frequency limit of Maxwell-Wagner polarization is $K = \frac{\sigma_2-\sigma_1}{3\sigma_1+3(\sigma_2-\sigma_1)L}$, and the high-frequency limit is $K = \frac{\varepsilon_2-\varepsilon_1}{3\varepsilon_1+3(\varepsilon_2-\varepsilon_1)L}$. For a silicon particle and DI water with $\sigma_2 - \sigma_1 > 0$ and $\varepsilon_2 - \varepsilon_1 < 0$, thus Maxwell-Wagner polarization has a positive low-frequency limit and a negative high-frequency limit. There always is a crossover frequency ω_C that devides the positive and negative polarization region, regardless of the particle geometry. The crossover frequency ω_C at which $\mathrm{Re}(K) = 0$ can be expressed as:

$$\omega_C = \sqrt{\frac{\sigma_1 - \sigma_2}{\varepsilon_2 - \varepsilon_1}\frac{L\sigma_2 + (1-L)\sigma_1}{L\varepsilon_2 + (1-L)\varepsilon_1}} \tag{6.3}$$

For a spheroid particle (a=b), $L_a = L_b = (1 - L_c)/2$. As the aspect ratio $\beta = c/a$ increase, L_c decreases and $L_{a,b}$ increases. For disk-like particles (a=b, c is mall), $L_a = L_b \ll 1$, and $L_c \approx 1$. For spherical particles, $L_a = L_b = L_c = \frac{1}{3}$. For needle-like particles (a=b, c is large), $L_a = L_b \approx \frac{1}{2}$, and $L_c \ll 1$. The depolarization factor versus aspect ratio is shown in Fig. 6.2. Since $\frac{\sigma_2}{\varepsilon_2} > \frac{\sigma_1}{\varepsilon_1}$, the crossover frequency increases with the depolarization factor *L*. In another words, higher aspect ratio (c/a), leads to lower crossover frequency along the major axis. Furthermore, *L* is bounded between 0 and 1, there naturally exists two limits of the crossover frequency, the upper limit is $\lim_{L\to 1}\omega_c = \sqrt{\frac{\sigma_1-\sigma_2}{\varepsilon_2-\varepsilon_1}\frac{\sigma_2}{\varepsilon_2}}$, and the lower limit is $\lim_{L\to 0}\omega_c = \sqrt{\frac{\sigma_1-\sigma_2}{\varepsilon_2-\varepsilon_1}\frac{\sigma_1}{\varepsilon_1}}$. Non-spherical particles have different depolarization factor *L* along different axes, and the corresponding crossover frequencies are different (as long as $\frac{\sigma_2}{\varepsilon_2} \neq \frac{\sigma_1}{\varepsilon_1}$). Thus, there exists differences among the crossover frequencies along different axes, and as a result, the particle will favor different alignment orientations at different frequencies. For spheroid particles, the crossover frequency along

the major axis (longest principal axis) ω_{C1} is lower than that along the minor axis (shortest principal axis) ω_{c2}. When $\omega < \omega_{C1} < \omega_{C2}$, the particle aligns with the major axis in parallel to the field. When $\omega_{C1} < \omega < \omega_{C2}$, the particle aligns to the orientation that minor axis is parallel to the field. When $\omega_{C1} < \omega_{C2} < \omega$, the particle favors the orientation that major axis in parallel with the field again. Different crossover frequencies along different axes enable a distinct approach to control the particle orientation by tuning the AC field frequency, and a wide frequency window between ω_{C1} and ω_{C2} is preferred. From equation (6.3), it can be found that the depolarization factor *L* plays the role as a weight coefficient in the expression. Higher aspect ratio of the particle leads to larger discrenpancy in the depolarization factor along major and minor axes, and results in a wider frequency window between the two crossover frequencies. Finally, with the value of $\varepsilon_1, \varepsilon_2$ and σ_1 fixed, increasing the particle conductivity σ_2 (upon light exposure), can effectively increase the low frequency limit of K, as well as the crossover frequency ω_C. For non-spherical particles, width of the frequency window between ω_{C1} and ω_{C2} also increases with the particle conductivity σ_2, as the difference between $\frac{\sigma_2}{\varepsilon_2}$ and $\frac{\sigma_1}{\varepsilon_1}$ increases with σ_2.

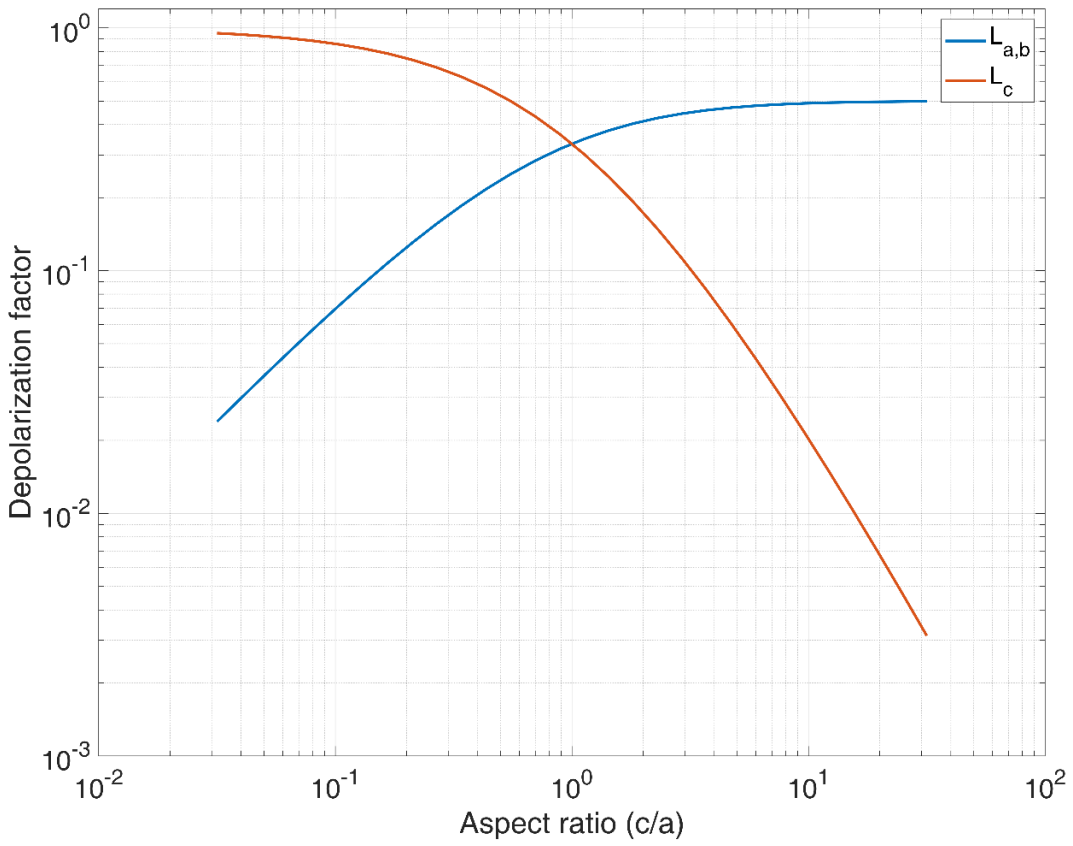

Figure 6.2. Depolarization factor along the principal axes a, b and c (a, b axes are equal in length) with different aspect ratios are shown in red and blue, respectively.

Besides the Maxwell-Wagner polarization, the electrical double layer is also frequency dependent with a different relaxation time τ_{RC}. From equations (2.19, 2.20), it can be found that, at low frequencies ($\omega_{\tau_{RC}} \ll 1$), both real part and imaginary part of the total polarization along any axes almost vanish at the low frequency limit due to the EDL screening, while at high frequencies, they are asymptotic to the Maxwell-Wagner polarization as the EDL effect gradually fades away with the increase of AC frequency. With consideration of the EDL effect, we separately calculate the polarization components

of Mawell-Wagner polarization and EDL as well as the total polarization of three representative particles as shown in Fig. 6.3-6.5. In this system, the relaxation time of EDL ($\tau_{RC} = 2 \times 10^{-5}$ s) is always longer than the Maxwell-Wagner charge relaxation time τ_{MW} within the considered range of particle conductivity and regardless of the particle geometry. The crossover frequency determined from Maxwell-Wagner polarization is almost identical to the crossover frequency of the total polarization as shown in Fig. 6.3-6.5.

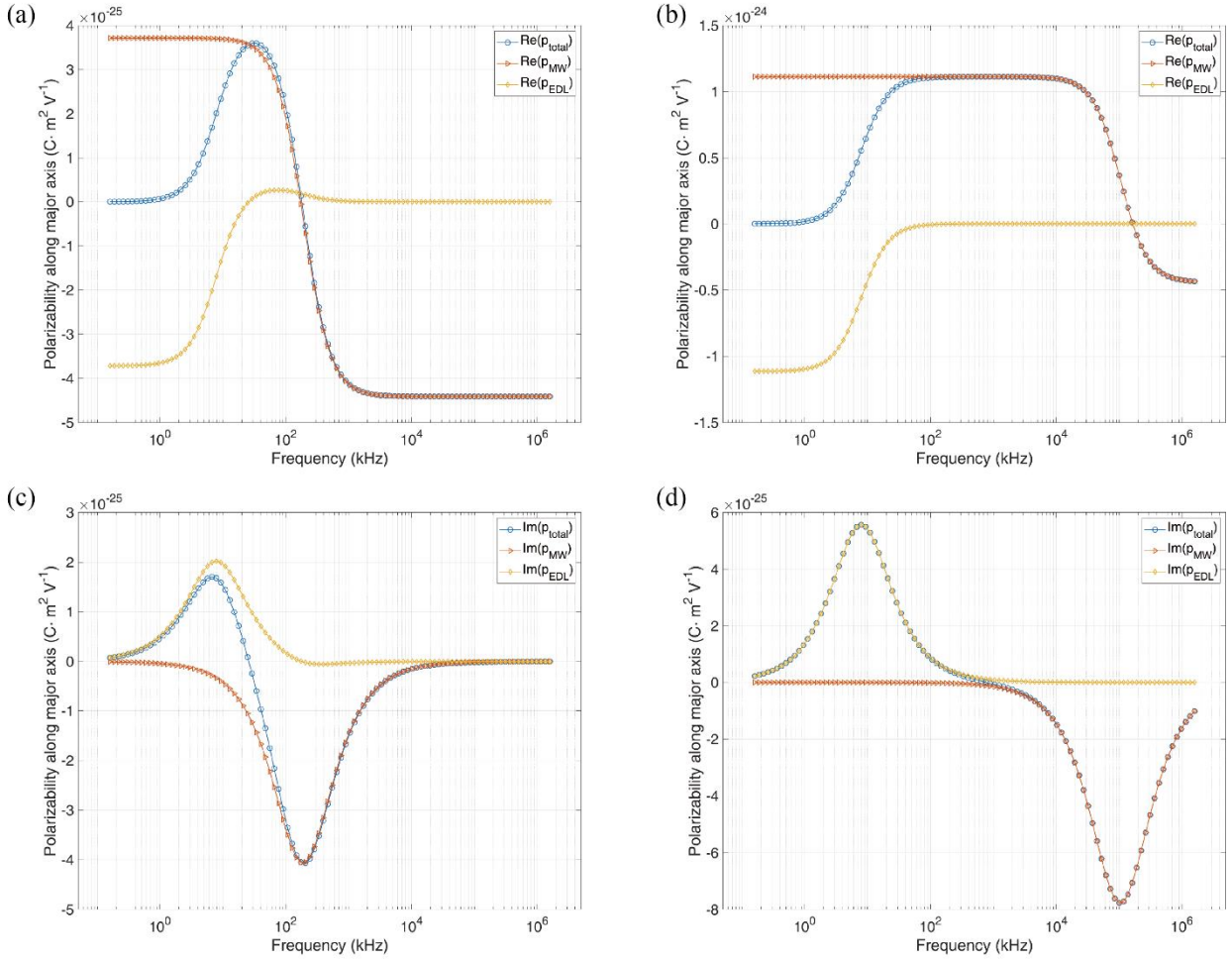

Figure 6.3. Polarizability components of a spherical silicon particle (5 μm in radius) in D.I. water (conductivity of 4 μS/cm). The real and imaginary parts of the total polarizability, and polarization components from Maxwell-Wagner polarization and EDL are displayed, respectively. Real part of polarizability with (a) a low electric conductivity (σ_{Si}=0.001 S/m), and (b) a high electric conductivity (σ_{Si}=1 S/m). Imaginary part of polarizability with (c) a low electric conductivity (σ_{Si}=0.001 S/m), and (d) a high electric conductivity (σ_{Si}=1 S/m).

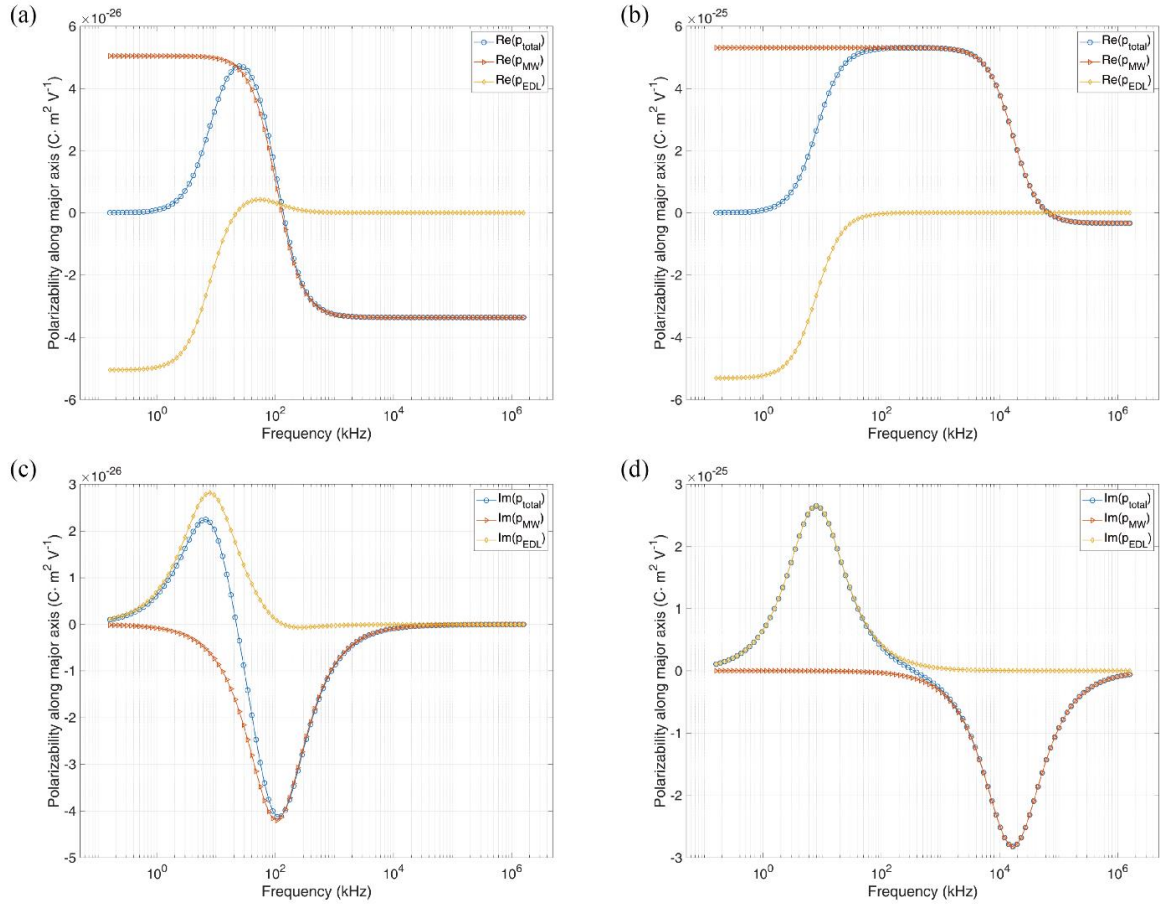

Figure 6.4. Polarizability components of a disk-shaped particle (#6, a:b:c=10:10:1). The real and imaginary parts of the total polarizability, and polarization components from Maxwell-Wagner polarization and EDL are displayed, respectively. Real part of polarizability with (a) a low electric conductivity (σ_{Si}=0.001 S/m), and (b) a high electric conductivity (σ_{Si}=1 S/m). Imaginary part of polarizability with (c) a low electric conductivity (σ_{Si}=0.001 S/m), and (d) a high electric conductivity (σ_{Si}=1 S/m).

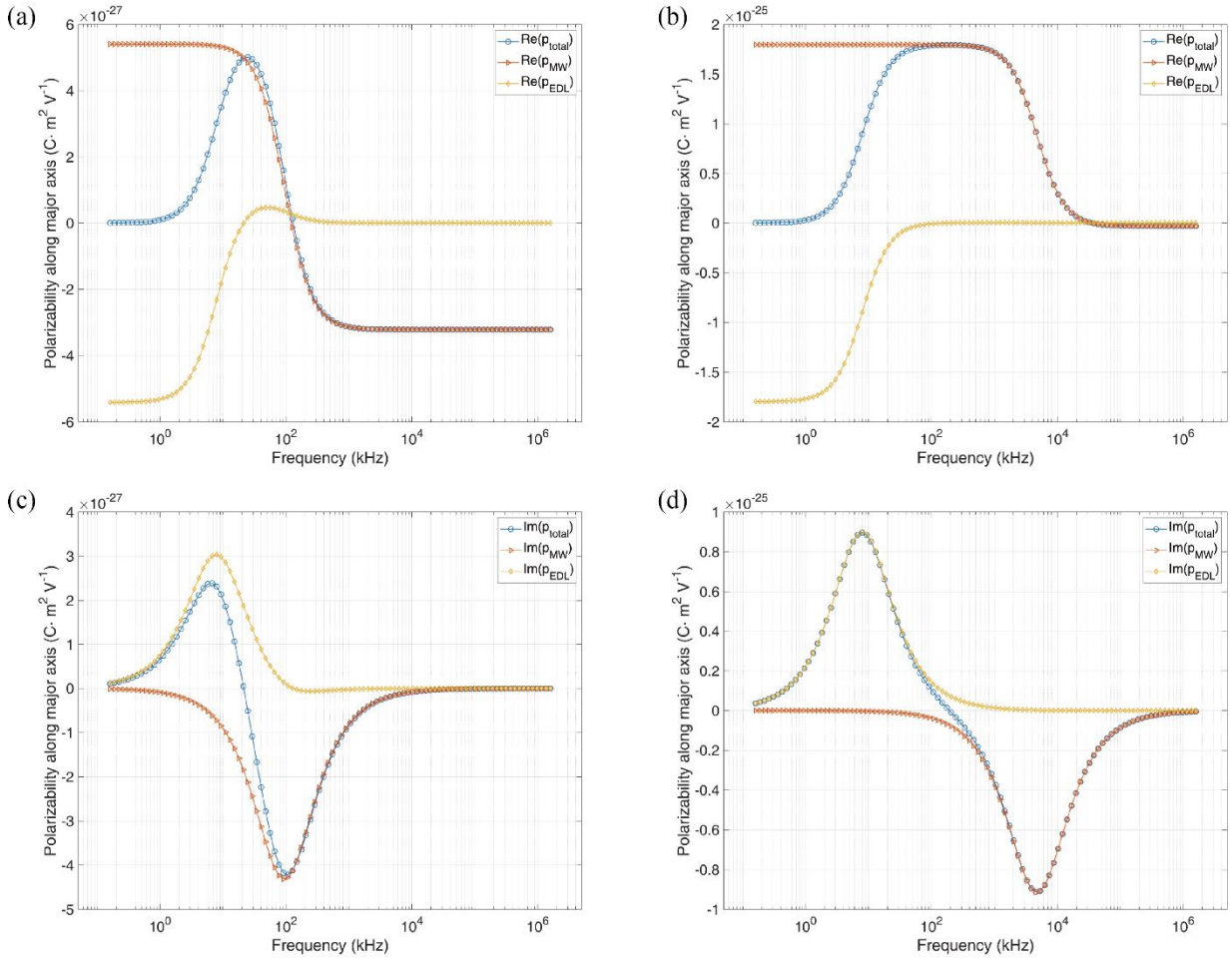

Figure 6.5. Polarizability components of a needle-shaped particle (#11, a:b:c=1:1:10). The real and imaginary parts of the total polarizability, and polarization components from Maxwell-Wagner polarization and EDL are displayed, respectively. Real part of polarizability with (a) a low electric conductivity (σ_{Si}=0.001 S/m), and (b) a high electric conductivity (σ_{Si}=1 S/m). Imaginary part of polarizability with (c) a low electric conductivity (σ_{Si}=0.001 S/m), and (d) a high electric conductivity (σ_{Si}=1 S/m).

6.2. Numerical Results and Analysis

With the above analytical discussion of the frequency, geometry and conductivity dependence of polarization, we then conducted numerical investigation for a set of spheroid

particles. First, oblate spheroid silicon particles ($a = b > c$) are studied, including one sphere ($a = b = c = 5\ \mu m$) and another 5 spheroids with monotonically reduced aspect ratio $\beta = c/a$ from 0.8 to 0.1 $0.8\ to\ 0.1$with the half-axis length a and b fixed at 5 μm. Both the polarization at a low conductivity ($\sigma_{Si} = 0.001$ S/m) and a high conductivity ($\sigma_{Si} = 1$ S/m) are calculated to demonstrate the effect of photoconductivity upon light exposure. The polarizability is calculated by using the model discussed above by considering both Maxwell-Wagner relaxation and the electrical-double-layer effect.

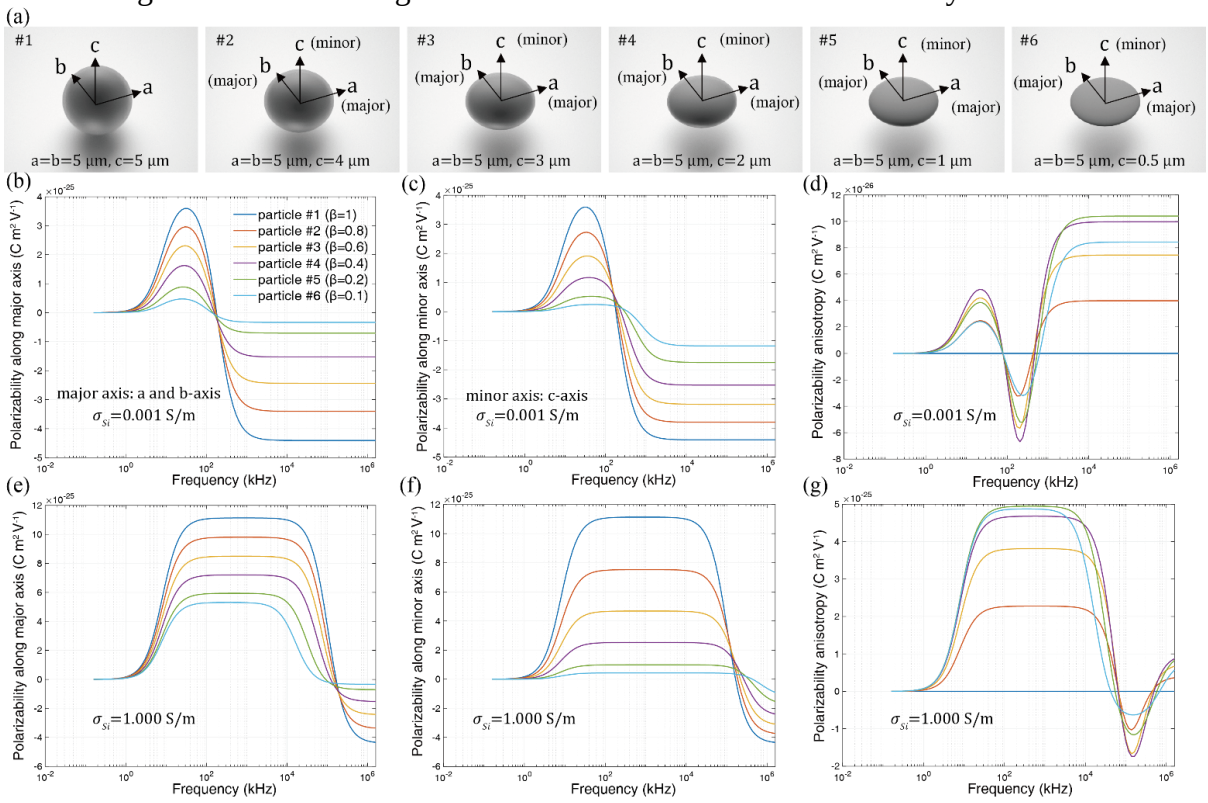

Figure 6.6. Calculation of the electric polarizability and anisotropy (difference between polarizabilities along major axis and minor axis) of various oblate spheroid Si particles with different electric conductivities in the medium of deionized water with conductivity of 4 μS/cm. (a) Six oblate spheroid particles in the simulation. (b-d) The electric polarizability along the major axes (a and b-axis), minor axis (c-axis) and the anisotropy of the oblate spheroid particles with a low conductivity of 0.001 S/m, and (e-g) a high conductivity of 1 S/m.

As shown in Fig. 6.6b-c, the electric polarizability along the major axes (the longest principal axes, which are a-axis and b-axis in this case) always vanishes at the low frequency limit due to the EDL screening, while at the high frequency limit, it levels off to a negative value as discussed in the previous section. The magnitude of the electric polarizability decreases when the spheroid shrinks in the c-axis, which agrees with equation (3), which indicates the electric polarization is directly proportional to the volume of a particle. By comparing the electric polarizability at both low and high electric conductivities controlled by light illumination, it can be readily found that the electric conductivity plays an immense role in governing the frequency-dependent electric polarization. First of all, by increasing the electric conductivity, the magnitude of the peak of the positive electric polarizability can be augmented by several times depending on the particle geometry, and the peak of the positive polarization can extend to a broad range of frequencies into a plateau, which is a result of $\frac{1}{\tau_{RC}} \ll \frac{1}{\tau_{MW}}$. By tuning the electric conductivity from 0.001 S/m to 1 S/m, for the spherical particle (#1), the maximum positive polarizability can be magnified by around 3 times, while for the disk-like oblate spheroid (#6) with aspect ratio (c/a) of 0.1, the magnification is more than 11 times. Thus, with the reduction of the dimension along the c axis, the increase of the electric polarization by the light-enhanced electric conductivity becomes more effective. For the negative polarizability, at the low electric conductivity, the crossover frequency occurs at around 200 kHz, while at the high electric conductivity controlled by light, the switching frequency shifts to above 100 MHz, which is already beyond the commonly used AC-frequency range for electrokinetics. As a result, below 200 kHz, the positive electric polarization can be much improved by the increase of the electric conductivity, and the positive DEP force can be amplified several times. At the same condition, when it is above 200 kHz, the sign of

the electric polarization, as well as the DEP force, can be switched from negative to positive by increasing the conductivity.

Furthermore, when a particle changes the geometry from spherical, oblate spherical, to disk as shown in Fig. 6.6a, the directional anisotropy of electric polarizability emerges, and the electric polarizability along the c-axis differs from that of a-axis for a particle of either a low (Fig. 6.6d) or a high electric conductivity (Fig. 6.6g). As the anisotropy of the electric polarizability along different axes emerges, the orientation of the particle should be considered since the total electrical potential energy is different along different orientations. For a oblate spheroid, it either orients with a,b-axis or c-axis along the direction of the electric field depending on which polarizability has a greater real-part value as shown in equation (3). We calculate the anisotropy of the electric polarizability, given by $\mathrm{Re}[\alpha_a - \alpha_c]$, of all the six shapes (Fig. 6.6a) for a particle of either a low (Fig. 6.6d) or a high electric conductivity (Fig. 6.6g). It is found that at a low electric conductivity, all the oblate spheroidal particles orient towards the a-axis (or b-axis) along the electric-field direction below ~77 kHz, and switch to the c-axis alignment with the electric field between 77 kHz to around 550 kHz (slightly different for different geometries), and then switch back to the a-axis alignment at even higher frequencies. At a high conductivity, all of the oblate spheroidal particles align with one of its major axes orienting along the electric-field direction below 60 MHz, and switch to the minor-axis-alignment in the range of ~ 60 MHz to ~100 MHz, and then switch back to the major-axis-alignment at even higher frequencies. The sphere (#1 in Fig. 6.6(a)) does not show electric anisotropy and alignment effect, but even a minor shape change can result such an effect (oblates #2-6 in Fig. 6.6a). In addition, by comparing the sign of the anisotropy of the electric polarizability between 77 kHz to 550 kHz for a particle of a low (Fig. 6.6d) and high conductivity (Fig. 6.6g), it is clear that the orientation of oblate particles can be

facilely switched between the two alignment states by tuning the electric conductivity with light. More will be discussed later.

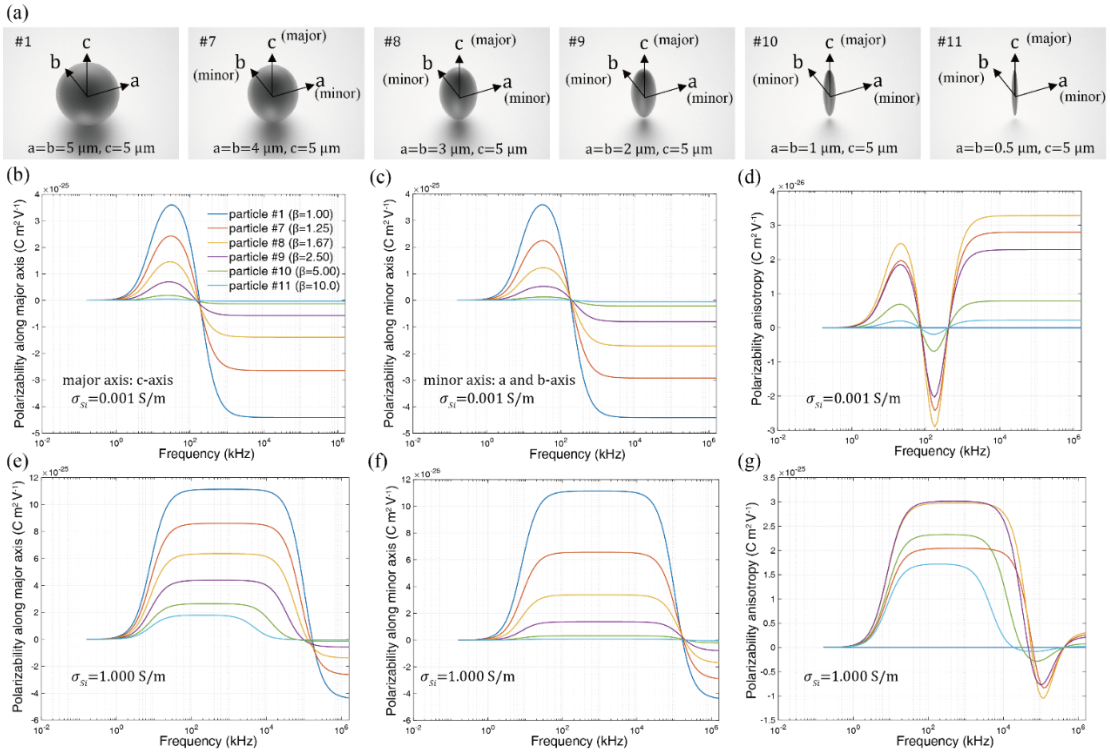

Figure 6.7. Calculation of electric polarizability and electric anisotropy of various prolate spheroidal silicon particles with different electric conductivities suspended in deionized water with conductivity of 4 μS/cm. (a) Diagrams of six prolate spheroidal particles. Electric polarizability along the (b) major axes (c-axis) and (c) minor axes (a and b-axis), and (d) the electric anisotropy of the six prolate spheroid particles of low electric conductivity of 0.001 S/m and (e-g) high conductivity of 1 S/m.

Another type of special geometry of interest is the prolate spheroids (a=b<c). Here we studied 6 prolate spheroids with an aspect ratio $\frac{c}{a}$ ranges from 1 to 10, where the half length a and b ranging from 5 μm to 0.5 μm, and $c = 5$ μm. As shown in Fig. 6.7a-f, the prolate spheroid polarizability spectrum is generally similar to that of the oblate spheroid, with moderate differences in amplitude and frequency. Particularly, it is found

that the amplification of the positive electric polarizability along the major axis (c-axis) between the low and high conductivities increases with the aspect ratio $\frac{c}{a}$. The needle-like prolate particle (#11) for example, has an aspect ratio of 10, and its polarizability along the c-axis amplifies more than 35 times as the electric conductivity increases from 0.001 to 1 S/m by light, while with the same change of electric conductivity, the electric polarizability of a spherical particle (#1) only can be enhanced by around 3 times (Fig. 6.7b and e). Thus, the prolate spheroids are better shapes for obtaining a large range of light-tunable DEP forces with high sensitivity to electric conductivity.

The above discussion summarizes the systematic study of the frequency, geometry, and conductivity dependence of electric polarizabilities of silicon spheroid particles in DI water from both numerical results and anlytical discussion. The obtained understanding is essential to realize the function-oriented design of microparticles for efficient light-reconfigurable manipulation and applications.

6.3. Light-Stimulated Transport of Microparticles with Simultaneously Controlled Alignment

The obtained results of the dependence of the electric polarizability of Si microparticles on the geometry, AC frequency and electric conductivity are critical for us to design innovative systems for light-stimulated versatile transport of microparticles with simultaneously controlled alignment. For simplicity, we first consider the scenario that the electric-field gradient is parallel to the electric field direction. Such an electric-field distribution can be implemented by applying an AC voltage onto two concentric circular electrodes as shown in Fig. 6.1. Both the electric field and the gradient of the electric field

are radial, pointing towards the center of the inner electrode (to be quantitatively discussed later).

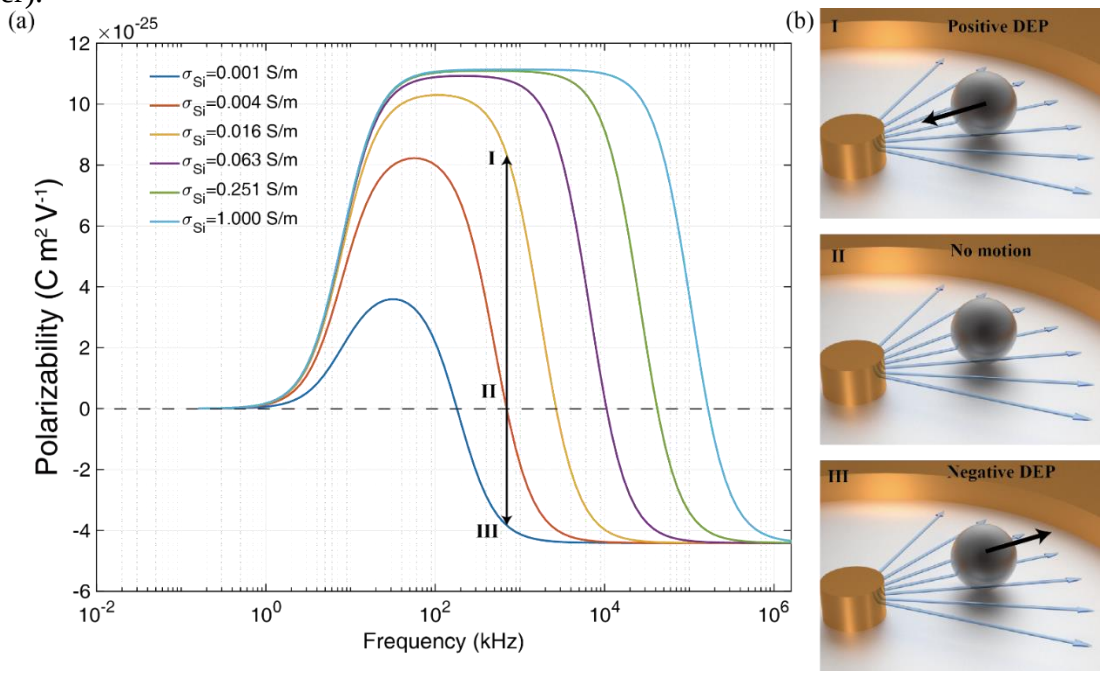

Figure 6.8. Calculation of the electric polarizability of the spherical particle (#1). (a) Electric polarizability of a spherical particle versus AC frequency with different electric conductivities. At 700kHz, I, II and III show three possible motion modes with positive, zero and negative DEP forces, respectively. (b) Corresponding diagrams of the three motion modes.

Due to the geometric symmetry, a spherical particle experiences zero alignment torque in an AC electric field, and the polarizability is isotropic. Within a concentric electric field, there only are three possible modes of motion for the spherical particles: (1) moving towards the center, (2) moving away from the center (3) no motion. It is possible to switch the motion modes by just controlling the light intensity at a given AC frequency, a result of the tuning of the photoconductivity of the silicon particles. Here, in addition to the light-controlled photoconductivity, there could be additional electric conductivity from

doping and thermal excitation. For simplicity, we consider the Si is undoped and the photoconductivity is the dominant source of electric conductivity due to its change of many orders of magnitude. We calculate the electric polarizability of the spherical particle #1 by varying the electric conductivities from 0.001 to 1 S as shown in Fig. 6.8a. The AC frequency is selected to be 700 kHz, where a transition of the polarizability from negative to positive occurs. A base light intensity is defined at which the particle's electric conductivity equals 0.004 S/m. At this condition, the real-part electric polarizability equals zero and the particle remains stationary as indicated as the point II in Fig. 6.8a and Fig. 6.8c. If the light intensity increases higher than this base value, a positive DEP force is triggered, and the particle transports towards the center electrode (point I in Fig. 6.8a and Fig. 6.8b). If the light intensity decreases below this base value, a negative DEP force is produced, and the particle moves outwards from the center (point III in Fig. 6.8a and Fig. 6.8d).

For the oblate particle #6 (disk-like, aspect ratio 0.1), there are more possible modes of motion. To depict the general behavior, we first calculate the real-part polarizability along the major axes (a,b-axis) and minor axis (c-axis) as well as the polarizability anisotropy ($\mathrm{Re}[\alpha_a - \alpha_c]$) at a series of electric conductivities from 1 to 0.001S/m as shown in Fig. 6.9a-c. With the obtained results, we select an AC frequency at 1 MHz, where we can obtain five distinct motion modes as summarized in Fig. 6.9d and Table 6.1.

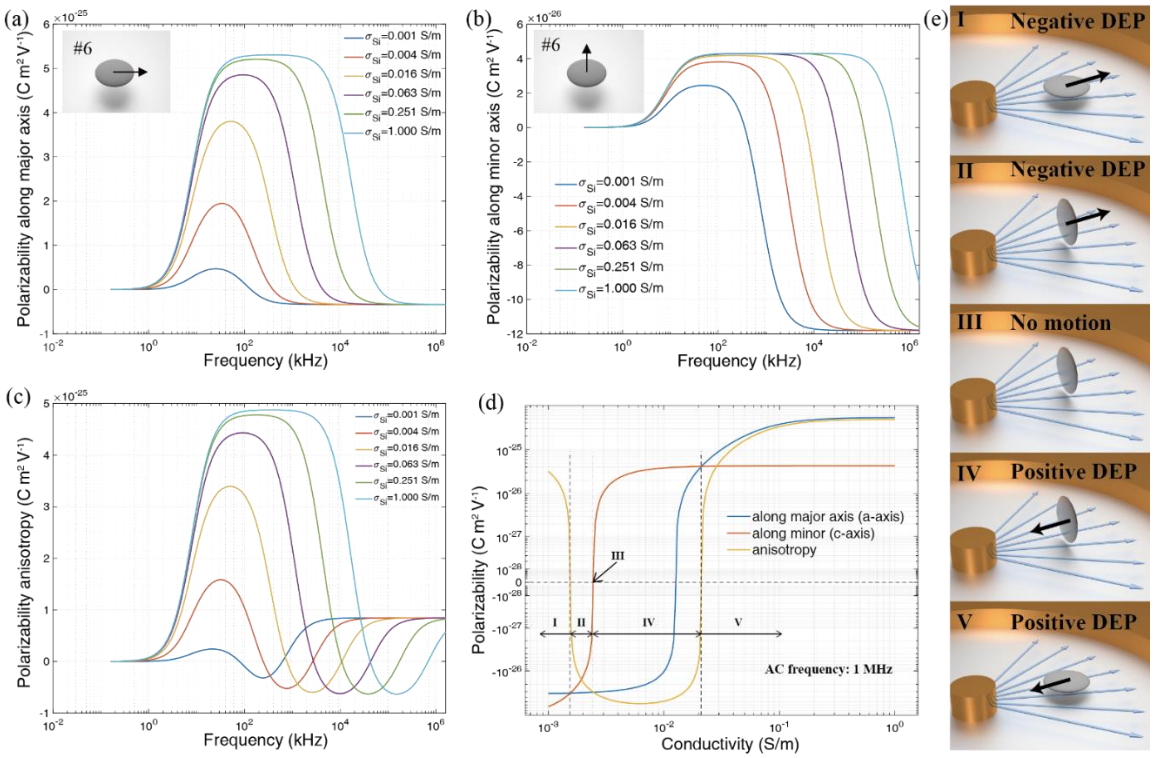

Figure 6.9. Calculation of the electric polarizability of the oblate spheroid particle (#6, disk-like, aspect ratio 0.1). Electric polarizability of the particle along (a) the major axis and (b) the minor axis versus AC frequency with different electric conductivities (inset: diagram of the polarization direction). (c) Electric polarizability anisotropy between the major-axis and minor-axis polarizabilities. (d) Electric polarizability and anisotropy as a function of electric conductivity at 1 MHz. (e) Diagrams of the five inter-switchable motion modes.

Motion Modes	I	II	III	IV	V
Conductivity (S/m)	<0.0015	0.0015-0.0024	~0.0024	0.0024-0.0219	>0.0219
Orientation along E-field	major-axis	minor-axis	minor-axis	minor-axis	major-axis
Sign of DEP force	negative (-)	negative (-)	zero	positive (+)	Positive (+)

TABEL 6.1. FIVE INTER-SWITCHABLE MOTION MODES OF THE OBLATE SILICON PARTICLE (#6, DISK-LIKE, ASPECT RATIO 0.1) WITH TUNABLE ELECTRIC CONDUCTIVITY BY LIGHT IN AN ELECTRIC FIELD AT 1 MHZ

By utilizing the same aproach, we analyze the electric polarizability, anisotropy, and motion modes of the prolate particle #11(needle-like, aspect ratio 10) as shown in Fig. 6.10a-d in Table 6.2. For the prolate particle #11, a, b-axis are the minor axes, and c-axis is the major axis. The anisotropy is defined as $\mathrm{Re}[\alpha_c - \alpha_a]$. The selected AC frequency is 2 MHz, at which maximum number of motion modes occurs.

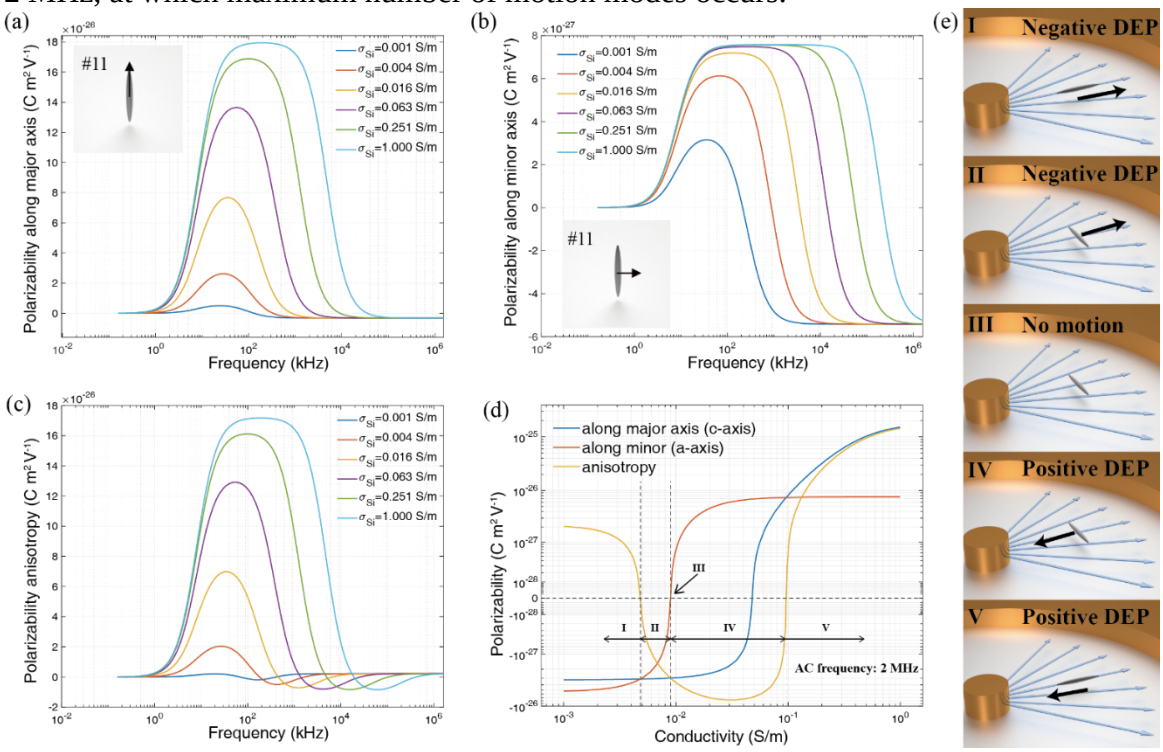

Figure 6.10. Calculation of the electric polarizability of the prolate spheroid particle (#11, needle-like, aspect ratio 10). Electric polarizability of the particle along (a) the major axis and (b) the minor axis versus AC frequency with different electric conductivities. (inset: diagram of the polarization direction). (c) Electric polarizability anisotropy between the major-axis and minor-axis polarizabilities. (d) Electric polarizability and anisotropy as a function of electric conductivity at 2 MHz. (e) Diagrams of the five inter-switchable motion modes.

Motion modes	**I**	**II**	**III**	**IV**	**V**
Conductivity (S/m)	<0.0024	0.0024-0.0045	~0.0045	0.0045-0.0437	>0.0437
Orientation along E-field	major-axis	minor-axis	minor-axis	minor-axis	major-axis
Sign of DEP force	negative	negative	zero	positive	positive

TABEL 6.2. FIVE INTER-SWITCHABLE MOTION MODES OF THE PROLATE SILICON PARTICLE (#11, NEEDLE-LIKE, ASPECT RATIO 10) WITH TUNABLE ELECTRIC CONDUCTIVITY BY LIGHT IN AN ELECTRIC FIELD AT 2 MHZ.

In summary, we demonstrate that for either the prolate or oblate spheroid particles, by selecting proper AC frequencies, one can rationally select and switch the translocation direction and alignment of a particle among 5 possible modes by simply modulating the photoconductivity. Two orientations, either alignment along the semi-major or the semi-minor axis with the electric field can be obtained. Within each orientation, the DEP force can be finely tuned from a negative value to a positive value.

6.4. Discussion

In this chapter, we conducted theoretical investigation on the tunable polarization of semiconductor microparticles under various light illumination and electric field frequencies. The model we applied is based on the Maxwell-Wagner polarization at the particle-medium interface as well as the electrical-double-layer effect at the charged surfaces. The description of Maxwell-Wagner polarization is analytical for the spheroid

particles, while the model for the EDL is a RC model. In our model, the EDL is represented by an effective dipole moment with opposite direction to the dipole from Maxwell-Wagner polarization, which has proved its effectiveness in understanding experimental results in electrorotation and electroalignment in previously reported works.[65,66] Not that this model can not predict the effect when particle size is small enough to be comparable with the EDL thickness. In this work, we only consider the particle above micrometer scale as the particle size is much larger than the electrical double layer thickness, *i.e.*, a thin-double layer approximation. A more sophistigated model can assist to understand a case when the size a particle is compareable to electric double by coupling the ion transfer, electrostatic (quasi-static) and hydrodynamics (osmosis flow) simultaneously.[73,74,95] Also as shown by a recent experiments that for particles with a size comparable to the EDL thickness, the Maxwell-Wagner polarization can be much overwhelmed by the space charge from the electrical double layer.[96]

We presented a theoretical investigation. It is desirable to further study the proposed light-controlled DEP manipulation to observe possible unforseen efforts, and unveil the potential limit. Here we would like to point out the potential challenges that could arise in experimental study. Note that in this theoretical study, we considered an ideal 2D planar electric field, and omitted all the possible effect from the specific design of electrodes. With practically fabricated microelectrodes, the electric field can have non-ideal distribution in 3D at their edges that should be considered in experimental testing. When using thin film microelectrodes for electric manipulation, AC electroosmosis (ACEO) flow could be induced around the microelectrodes when applying an AC voltage at frequencies below tens of kHz. This could disturb the motion of the particles near the microelectrodes. Such ACEO flows can be suppressed by choosing a suspension medium with low electric conductivity and apply a high frequency AC field. Moreover, the electrically polarized

microparticles near the thin film metallic microelectrode could experience an attractive dipole-dipole interaction originated from the induced charges. To minimize such an interaction, the particles under investigation should be manipulated sufficiently away from the electrodes. The properties of Si microparticles that can vary with different fabriation processes should be considered as well, including the size, geometry and doping level, surface conditions. The size may affect the EDL formation as previously mentioned. The geometry of particle will be influential to the light absorption at different wavelengths. Both doping level and surface oxidation will impact electric properties of the particle, deviating them from those of bulk silicon.

Here, we only presented an example of electrode design, *i.e.*, circular microelectrodes. The same working principle could be extended to 2D and 3D manipulations by utilizing strategically designed microelectrodes to generate the required field gradient in three dimensions. For instance, multipole electrodes that are symmetrically arranged circularly could be applied to generate desired in-plane field gradient in both the x and y directions, simply by adjusting the electrical potential applied on each of the microelectrode pads. By increasing the number of microelectrodes, fine control of the field gradient can be realized with the assistance of electrostatic simulation. Introducing the same electrodes array on top of the experimental cell, spaced by a thin separation layer, the electrical potential in 3D can be obtained, modulated, so does the field gradient. As a result, we expect the same working principle being applicable for 3D manipulation.

In terms of applications, in addition to micromachines, we envision that our work can add a new strategy to the current DEP-based cell/particle sorting techniques in continuous flow. For instance, controlling the orientation of non-spherical particles can change the drag coefficient for DEP-enabled particle sorting by geometry. Furthermore, if the particles are photo-responsive, a digital light projection system with real-time image

analysis will be able to generate and project dynamic light patterns and realize the modulation of each particle's conductivity and movement both simultaneously and independently.

Chapter 7: Collective Behavior of Silicon Micromotor Swarm in Suspension

Collective behaviors represent a wide range of phenomena that exist in nature as well as in artificial systems where the interaction between a large number of similar fundamental units of the system eventually results in a large-scale ordering in terms of either structure or movement. Collective behaviors in nature are pretty typical for animals that live in groups with a significant number, such as bird flock, fish school, ant colony etc.[97] The special communication and interaction mechanisms within the swarm play an important role in controlling the entire group's macroscopic movement. These phenomena also attract significant interest in fundamental science and engineering. The general idea is to dig out the simple rules of control on single elements to achieve complex swarm functionality. For example, it is of great importance to control a robotic swarm, where each robot may only be able to execute several simple commands or receive very limited signal from surroundings, yet the entire swarm may still be capable of performing challenging and complex tasks. Over the past decades, there are plenty of works studying the collective behaviors from systems of a wide range of scales, from as small as molecular systems such as DNA self-assembly,[98] to large system such as drone swarm.[99] In between, the colloidal system with elemental units of micrometer size attracts significant interest as they are simple, clean, and easy to be manipulated. Self-assembly of colloids is a structural form of collective behavior which has been extensively studied via electrostatic,[100-103] magnetic,[102,104-106] hydrodynamic[107] and chemical reactions.[42] Collective motion of self-propelled colloids is also studied as a dynamic form of collective behavior.[108-113] Although among these artificial systems, the mechanisms of the ordering formation are various, they are still helpful in accumulating the understanding of fundamental interactions that are

capable of generating ordering behavior, that can facilitate the design of other systems or providing understanding of an existed systems with similarity.

In this work, we introduce a new colloidal system consists of rod-like silicon nanowires that break the spherical symmetry and actuated by an AC rotating field applied horizontally with perturbation of light as the trigger of local structure formation. The previous study on the optical modulation of the electro-rotation and electro-alignment of silicon nanowires has revealed that the light-induced conductivity change can effectively modulate the nanowire polarization under AC electric field. The electro-rotation experiment has shown that the imaginary part of the nanowire polarization under a rotating AC electric field can be enhanced, attenuated, or reversed by light stimuli at various frequencies.[114] From the electro-alignment experiment, the light-induced enhancement of the real part polarization from silicon nanowire under a linear AC field has been demonstrated.[66] These experimental studies have revealed the effect of light on the induced dipole and the regulation of the dipole-field interaction correspondingly.

With low nanowire density in the solution, the interaction between the neighboring nanowires is negligible as their separation is substantial. On the other hand, it is also of great interest to study collective behavior in a system with high nanowire density. As the density of wires increases, the separation between neighboring wires is sufficiently small, and under electric field, the induced dipole-dipole interaction from neighboring wires becomes vital in addition to the dipole-field interaction. The dipole-dipole interaction is proportional to the square of the electric field strength. However, we only apply a moderate field intensity so that without light stimuli, the dipole-dipole interaction is insufficient to trigger the collective behavior, and the ordering pattern forms locally in the area with light exposure. We demonstrate two distinct self-organization of nanowires into a 2D network

structure and cluster structure at different frequencies, and provide a qualitative understanding from a simple electrostatic-based model.

7.1. Results

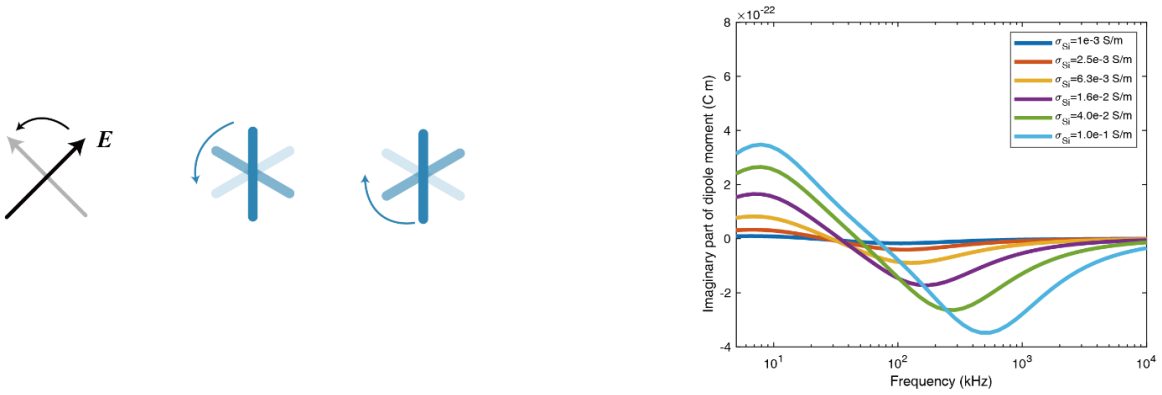

Figure 7.1. Schematic of the electro-rotation and the spectrum of imaginary polarization of the nanowire.

We first provide a summary of the fundamental behavior of single nanowires under the rotating electric field. As reported in our previous work, a rotating AC electric field with frequencies ranging from 5 kHz to 2 MHz can effectively drive the rotation of a silicon nanowire. The rotation speed can be modulated under laser exposure as the light-induced photoconductivity changes the polarization of the silicon nanowires. As the rotating frequency of the field is much higher than the rotation speed of the nanowire, during one cycle of the field oscillation, the nanowire can be regarded as still. The electro-rotation is thus an asynchronous rotation, where the field rotates much faster than the wires. The field vector can thus be decomposed into two components, one along the longitudinal direction of the nanowire, and the other along the transverse direction of the nanowire. We define the x-axis along the nanowire's longitudinal direction. The field vector can be expressed

as $\boldsymbol{E} = \boldsymbol{E_0}\,(\hat{\mathbf{x}} - \mathrm{i}\hat{\mathbf{y}})\exp(i\omega t)$ that is rotating counterclockwise at angular frequency ω. The field is introduced by applying four sinusoidal voltage signals with 90 degree phase lag sequentially onto the four electrode pads as shown in Fig. 3.1. Assuming that all the nanowires in the system have identical geometry and electrical properties, identical polarizability α can be introduced. Furthermore, as the nanowires have sufficiently large aspect ratio, the polarizability along the transverse direction is negligible in most frequencies, and α only represents the polarizability along the longitudinal axis of the nanowire. Under an AC field, due to the Maxwell-Wagner polarization and electrical double layer effect, the polarizability α is a function of frequency and also a complex quantity contains the phase relation to the external field. The induced dipole from individual nanowires is $\boldsymbol{p} = \alpha \boldsymbol{E}_{\parallel}$. Since the field is constantly rotating, the phase of the field is the angle of the field vector. In a uniform electric field, the force that the field exerted on the induced dipole is always zero, however, the field exerts a torque on the induced dipole when the dipole moment has a non-zero imaginary part with reference to the phase of $\boldsymbol{E}_{\parallel}$. The averaged torque over one cycle can be expressed as: $\boldsymbol{\tau_e} = \frac{1}{2}\mathrm{Re}\left[\underline{\mathbf{p}}(\mathbf{t}) \times \underline{\mathbf{E}}^{*}(\boldsymbol{t})\right] = -\frac{1}{2}E_0^2\mathrm{Im}[\alpha]\hat{\mathbf{z}}$. In previous chapter, we have reported a simulation model that can effectively predict the general trend of polarization of silicon nanowire in DI water with various conductivity. The imaginary part of dipole moment of a silicon nanowire with 500 nm diameter and 10 μm length under an electric field of 60000 V/cm is calculated as shown in Fig. 7.1b. With a positive imaginary dipole moment, the nanowire spins along its center opposite the field rotation direction, and a negative imaginary dipole moment results in the rotation of wires that are in the same direction of the field. At around 10 kHz, the value of $\mathrm{Im}(\boldsymbol{p})$ reaches maximum, and gradually decreases until reaching the minimum in the range of 100 kHz to 500 kHz depending on its conductivity. For the nanowire used in this work, when there is no laser exposure, the nanowire's conductivity

is estimated to be around 10^{-3} S/m, as low as the intrinsic conductivity of undoped silicon at room temperature (dark blue curve in Fig. 7.1b). When exposed under 100 mW/cm^2 laser with 532 nm wavelength, the conductivity of the nanowire is estimated around 10^{-1} S/m. As a result, the laser exposure can effectively enhance the imaginary part of polarization.

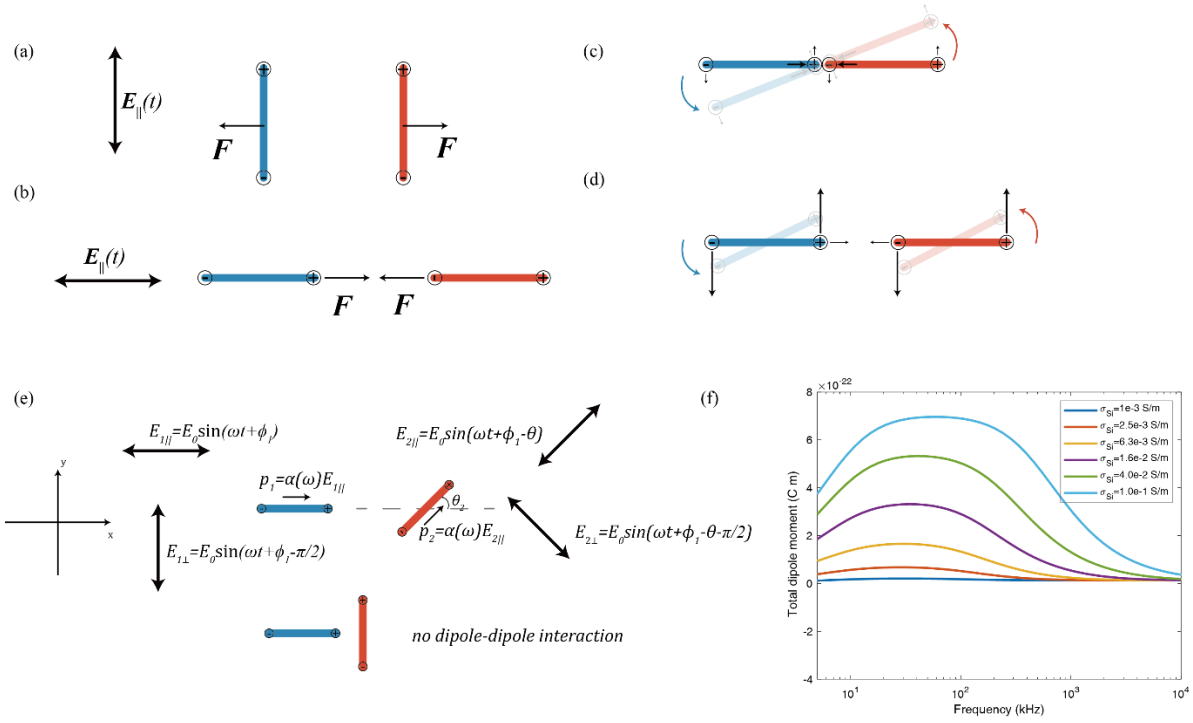

Figure 7.2. Two nanowire interaction. The dipole-dipole interaction between two identical nanowires arranged (a) side by side; (b) head to tail. (c) Two nanowires in the chaining mode, that assembled into a chain and rotate together when dipole-dipole interaction is strong. (d) Two nanowires in the spinning mode, without forming a chain when dipole-dipole interaction is weak, and rotational torque is strong. (e) The interaction between two wires with arbitrary orientation. (f) The total polarization spectra of nanowires with different conductivity.

Besides rotational torque from the dipole-field interaction, the dipole-dipole interaction between nanowires is also vital for the collective behavior. First, consider the

basic scenario with two identical nanowires under the field. As shown in Fig. 7.2a, when two wires are arranged side by side in parallel, the induced dipoles on each nanowire tend to repel each other. In Fig. 7.2b, when two wires are arranged head to tail, the induced dipoles attract each other. The dipole-dipole interaction is proportional to the square of the dipole moment and the square of the electric field strength. After considering the rotational torque, it is evident that when two wires are close to each other in the head-to-tail arrangement, the attractive force from the dipole-dipole interaction tends to drag two wires together, while the rotational torque from the dipole-field interaction tends to separate two wires and let them spin independently. When the attractive force dominates, two wires form an assembly and rotate as a whole (Fig. 7.2c). When the rotational torque dominates, two wires spin along their geometrical center separately (Fig. 7.2d). The competition between these two forms of motion is the foundation of the collective behaviors that will be discussed in the following sections.

To better understand, we adopt a simplified point-charge model to describe the interaction between the nanowires and the external field. Although the treatment of the induced dipole on nanowire as two opposite point charges fixed at the tips is not accurate, especially in the near field, it has been proved to be effective in reproducing many experimental observations with proper assumptions. Several assumptions are made in the model: 1) the nanowires are identical; 2) the dipole moment of individual nanowires is solely dependent on the external field, and the influence from neighboring wires' induced field is neglected; 3) only the polarization along the long axis of the nanowire is considered; 4) the hydrodynamic interactions between different wires are neglected as the electrostatic forces dominate over the hydrodynamic forces in most of the experimental conditions unless specifically noted in certain scenario (low frequencies). All the above assumptions

are reasonable in a model aiming for qualitative understanding. A more comprehensive explanation and experimental validation will be provided in the discussion section.

Each dipole is treated as two point-charges located at the two ends of the nanowire's long axis. As shown in Fig. 7.2e, the center of two nanowires are located at $\boldsymbol{r_1}$ and $\boldsymbol{r_2}$ with length l and orientation θ_1 and θ_2 relative to the x axis. Without losing generality, we assign $\theta_1 = 0$, as nanowire 1 in parallel with x axis. $\hat{\boldsymbol{s}}_1$ and $\hat{\boldsymbol{s}}_2$ are the unit vector along the long axes of the nanowire 1 and 2. The orientation of the nanowire is defined in the interval of $(-\pi/2, \pi/2]$. The component of the electric field $\boldsymbol{E}(t)$ that is in parallel with nanowire 1 and 2 are $\boldsymbol{E_{\parallel 1}} = E_0 \exp(i\omega t - i\theta_1)\, \hat{\boldsymbol{s}}_i$ and $\boldsymbol{E_{\parallel 2}} = E_0 \exp(i\omega t - i\theta_2)\, \hat{\boldsymbol{s}}_j$, and the corresponding induced dipoles are $\boldsymbol{p_1} = \alpha \boldsymbol{E_{\parallel 1}}$ and $\boldsymbol{p_2} = \alpha \boldsymbol{E_{\parallel 2}}$. To be noticed, since there exist a phase lag of $\theta_2 - \theta_1$ between $\boldsymbol{E_{\parallel 1}}$ and $\boldsymbol{E_{\parallel 2}}$, same phase lag will pass to the induced dipole $\boldsymbol{p_1}$ and $\boldsymbol{p_2}$. The dipole on nanowire 1 is then represented by two point-charges $q_1^+ = \frac{|\boldsymbol{p}_1|}{l}$ and $q_1^- = -q_1^+$ located at $\boldsymbol{r_1^+} = \boldsymbol{r}_1 + \frac{l}{2}\hat{\boldsymbol{s}}_1$ and $\boldsymbol{r_1^-} = \boldsymbol{r}_1 - \frac{l}{2}\hat{\boldsymbol{s}}_1$. The dipole-dipole interaction between the nanowire 1 and 2 is then calculated as a result of the Coulomb's forces between the four point-charge $q_1^+, q_2^+, q_1^-\ and\ q_2^-$. Since the nanowires are identical, $q_0 = |q_1^+| = |q_2^+| = |q_1^-| = |q_2^-|$. The induced charges are directly proportional to the dipole moment, and thus the same phase lag between $\boldsymbol{p_1}$ and $\boldsymbol{p_2}$ will be inherited by the charges: $q_1^{\pm} = \pm q_0 \alpha E_0 \exp(i\omega t - i\theta_1)$, $q_2^{\pm} = \pm q_0 \alpha E_0 \exp(i\omega t - i\theta_2)$. As a result, the Coulomb's force between $q_1^{\pm}$ and $q_2^{\pm}$ in average over one period equals:

$$F_{12} = \frac{\omega}{2\pi}\int_0^{\frac{2\pi}{\omega}} \frac{1}{4\pi\varepsilon}\frac{\mathrm{Re}\left(q_1^{\pm}\right)\mathrm{Re}\left(q_2^{\pm}\right)}{\left|\boldsymbol{r_1^{\pm}} - \boldsymbol{r_2^{\pm}}\right|^2}\mathrm{d}t = \frac{\cos(\theta_2 - \theta_1)}{2}\frac{1}{4\pi\varepsilon}\frac{q_0^2}{\left|\boldsymbol{r_1^{\pm}} - \boldsymbol{r_2^{\pm}}\right|^2} \qquad (7.1)$$

When two nanowires have an orthogonal orientation that $|\theta_1 - \theta_2| = \pi/2$, the dipole-dipole interaction vanishes.

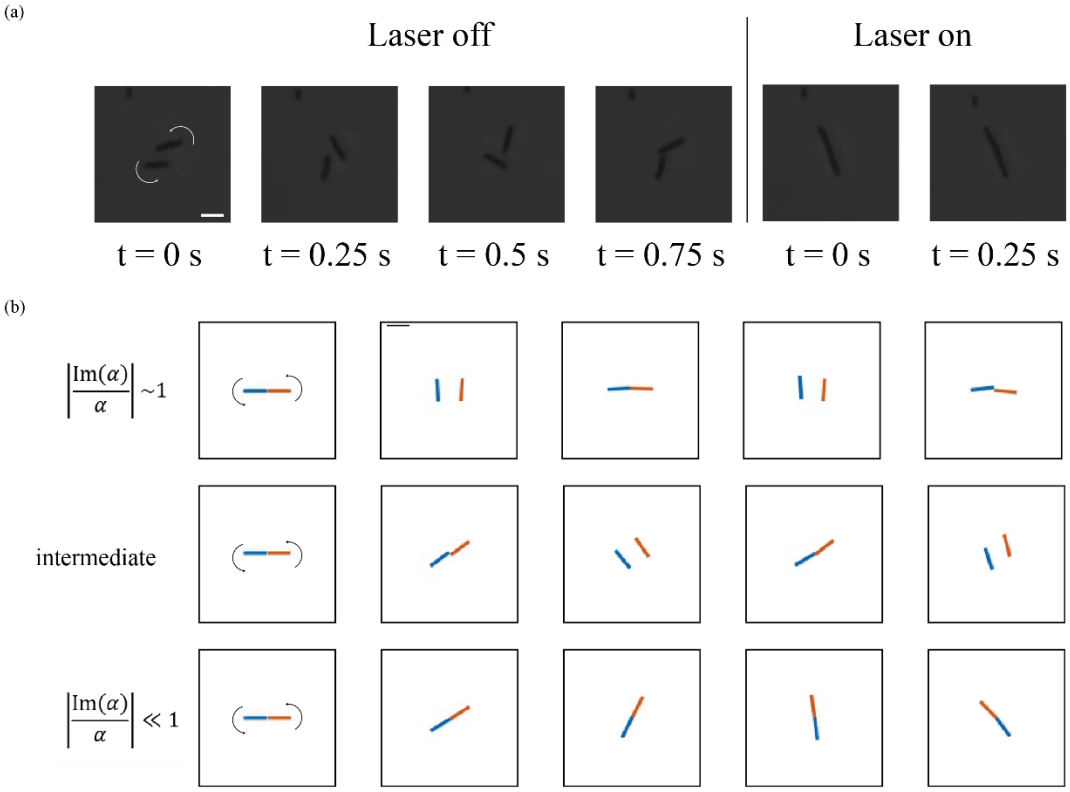

Figure 7.3. Dynamics of two neighboring nanowires. (a) Two nanowires rotate under 50 kHz AC field (60000 V/m) with and without laser exposure ($100\ mW/cm^2$). (b) Brownian dynamic simulation of two neighboring nanowires rotating with different fraction of imaginary part of polarization over total polarization. Scale bar is 10 μm.

We conduct experiments and Brownian dynamic simulations to study the two nanowire dynamics under various conditions with the above discussed dipole-field interaction and dipole-dipole interaction. In experiments, we select the frequency of 50 kHz. Without laser exposure, two nanowires close to each other spin along with their geometrical centers, as the rotational torque dominates over the attraction force from induced dipoles. When the laser shines on the wires, they quickly assemble into a chain, as the attraction force dominates over the rotational torque. Whether two neighboring wires

will spin separately or assemble into a chain depends on the competition between the rotational torque and the attraction force. The former depends on the imaginary part of polarization, and the latter depends on the total polarization. Thus, we conducted a series of Brownian dynamics simulations of two neighboring nanowires with a various ratio of $\left|\frac{\mathrm{Im}(\alpha)}{\alpha}\right|$ ranges from 0 to 1. When $\left|\frac{\mathrm{Im}(\alpha)}{\alpha}\right|$ is close to 1, the rotational torque dominates, and two wires spin separately as shown in Fig. 7.3b. On the other hand, when $\left|\frac{\mathrm{Im}(\alpha)}{\alpha}\right| \ll 1$, the attraction force dominates, and two wires assemble into a chain and rotate as an integral. This transition from the spinning state to chaining state is the fundamental reason for the first type of collective behavior we will discuss.

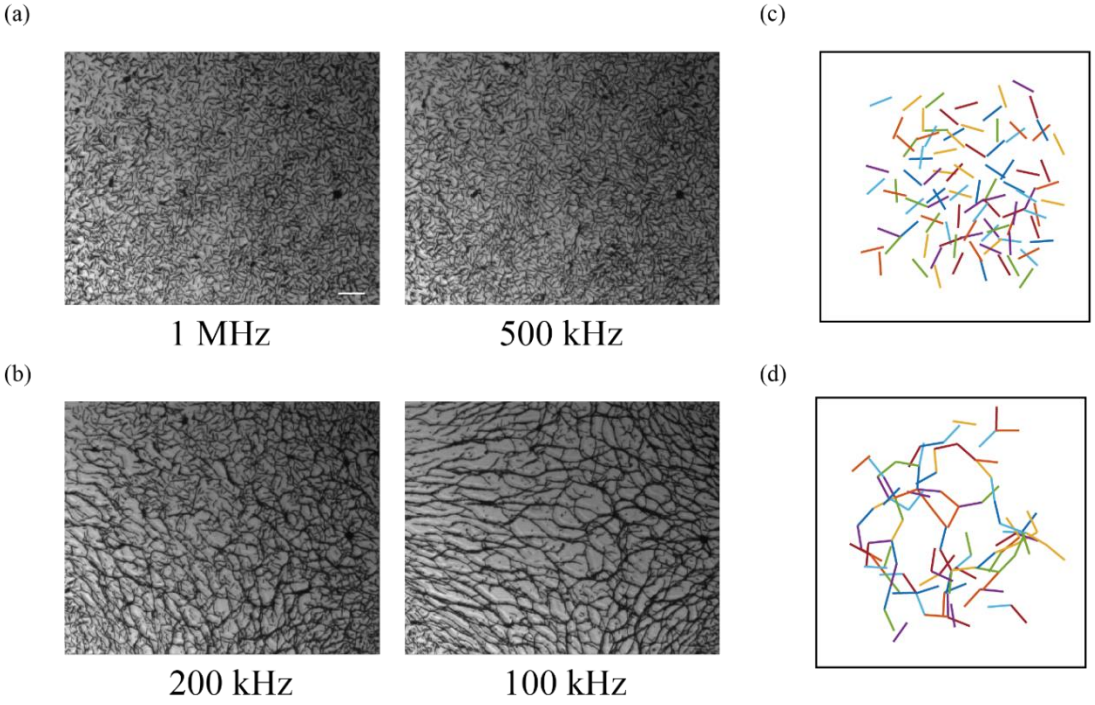

Figure 7.4. The behavior of nanowire suspension under rotating electric field of various frequencies with global laser exposure of 100 $\mathrm{mW/cm^2}$. (a) The spinning state of the nanowire suspension is observed at frequencies above 500 kHz. (b) The network formation of the nanowire suspension is observed between 50 kHz to 200 kHz. (c) the simulation result of the spinning state. (d) the simulation result of the network formation. Scale bar is 50 μm.

With the above understanding, we investigated the behavior of the suspensions of silicon nanowires. First of all, without laser exposure, across all frequencies from 10 kHz to 1 MHz, under field strength of 60000 V/m, the nanowires spin independently and are randomly oriented without any unique pattern formation. We intentionally select this moderate electric field strength so that the dipole-dipole interaction is insufficient without laser exposure, and the collective behavior can only be triggered by the laser exposure, under which the dipole moment can be significantly enhanced. When exposed to the laser, as the polarization has been enhanced, the more vital dipole-dipole interaction results in unique pattern formation at certain conditions. Above 500 kHz, according to the simulation result shown in Fig. 7.1b, the rotation speed of nanowires under laser exposure is significantly accelerated. However, all wires still spin along with their geometrical centers independently without much interaction with neighboring wires, as shown in Fig. 7.4a. Between 50 kHz to 200 kHz, the wires interconnect with the neighboring wires and form a highly branched 2D network under laser exposure, as shown in Fig. 7.4b. Within this frequency range, the imaginary part of polarization takes up a small fraction of the total polarization so that the attraction force from dipole-dipole interaction dominates over the rotational torque from dipole-field interaction. At 200 kHz, the nanowires still rotate until they are strongly attracted to one of the main branches. It is a dynamic process in which short and thin branches and isolated wires still rotate or even detach from the current network and reassemble at more stable locations. The network becomes most stable at 100 kHz when the rotational torque almost vanishes, and wires quickly connect to neighboring wires upon laser exposure. Initially, the network contains many small cells separated by a highly branched network. As time goes, the small cells gradually coarsen into larger cells as the small branches merge with the main branches nearby. The network will quickly dissemble as soon as the laser is turned off. We further demonstrated that the network

formation could be localized with a predefined light pattern projected on the sample surface. The simulation result also confirms that when $\left|\frac{\mathrm{Im}(\alpha)}{\alpha}\right| \sim 1$, nanowires are in the spinning state as shown in Fig. 7.4c, same as the experimental observation under 500 kHz and above. When $\left|\frac{\mathrm{Im}(\alpha)}{\alpha}\right| \sim 0$, the nanowires quickly form a network as shown in Fig. 7.4d, very similar to the experimental observation at 100 kHz. Overall, we understand that the transition of nanowire suspension from spinning state to the formation of a stable network is originated from the increasing of total polarization and the decreasing of the imaginary part of polarization.

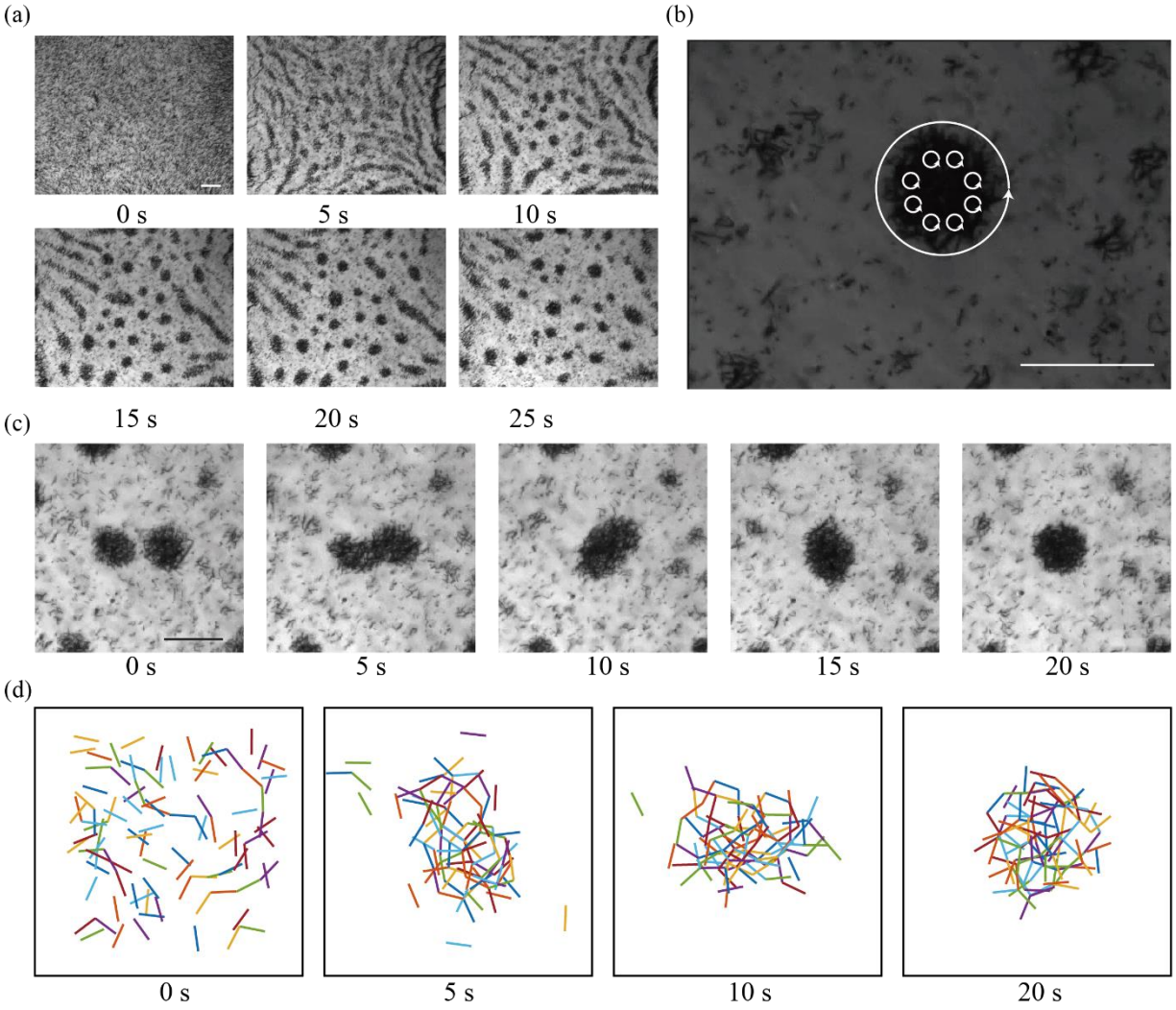

Figure 7.5. The clustering of silicon nanowire suspension at 10 kHz. (a) the snapshot with 5 second time interval showing the clustering process under global laser exposure. (b) the zoom-in image of one cluster, where the nanowires spin around their own center as well as process along the periphery of the cluster. (c) the merging process of two neighboring clusters. (d) the simulation result that reproduces the clustering. Scale bars are 50 μm.

Further decreasing frequency, a new clustering phenomenon occurs at 10 kHz, where the wires under laser exposure tend to nucleate into clusters, as shown in Fig. 7.5a. The clustering process takes longer than network formation, as it requires long-range interactions that attract wires to the nucleation sites across a longer distance. The initial

nucleation sites are highly random when the wire density is uniform in the suspension. It can be regarded as an analogy to the homogenous nucleation process. The nucleation occurs due to the random local fluctuation of nanowire density or geometry (i.e., a long wire or a wire bundle with intense polarization is more likely to become the nucleation center). All nucleation sites attract nanowires nearby, and as their size and density increase, the attractive forces increase as well so that wires further away can be attracted. Eventually, the clusters stabilize when the nearby nanowires deplete, and the distance between clusters is far enough so that no coalescence could happen. The clusters contain a high density of wires stacking in multiple layers, each wire spins counter the field rotation direction, and the entire cluster also rotates in the same direction as an integral, as shown in Fig. 7.5b. When two clusters are approaching, they coalesce into a bigger cluster, as shown in Fig. 7.5c. To understand this clustering phenomenon, we also conduct a simulation and reproduce similar patterns. When setting the parameters in the model, since wires do not form chains but spin independently, the imaginary part should take up a significant fraction of the total polarization as $\left|\frac{\mathrm{Im}(\alpha)}{\alpha}\right| \sim 1$. Furthermore, we found out that to let the wires be attracted to the nucleation center, the total polarization must be strong enough to provide sufficient attractive forces across the long distance that can overwhelm the Brownian motion that tends to diffuse the wires away from the high-concentration area. When the total polarization is strong enough and $\left|\frac{\mathrm{Im}(\alpha)}{\alpha}\right| \sim 1$, we successfully reproduced the clustering phenomenon in the simulation as shown in Fig. 7.5d.

(a)

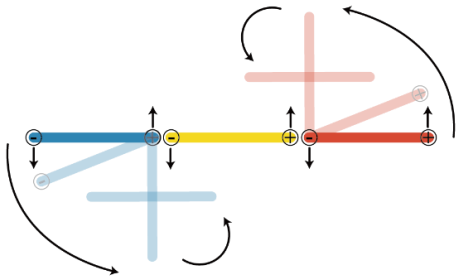

(b)

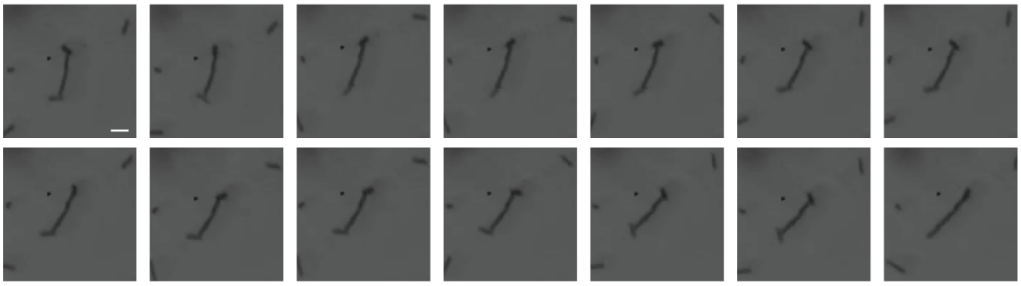

(c)

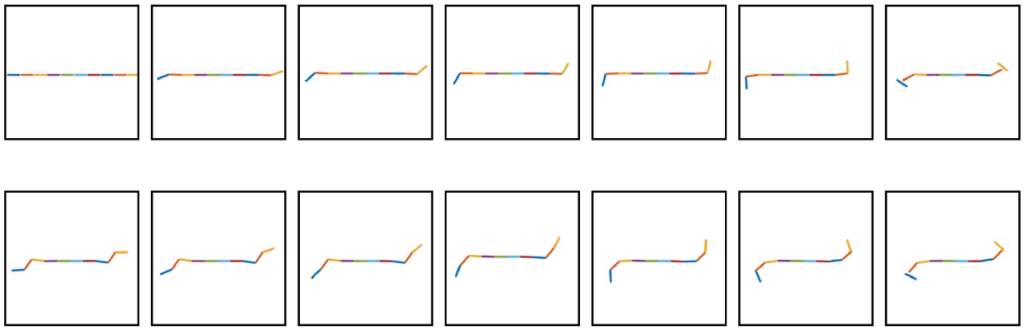

(d)

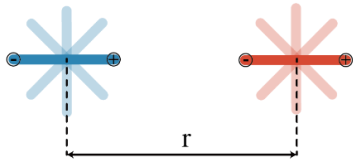
r

(e)

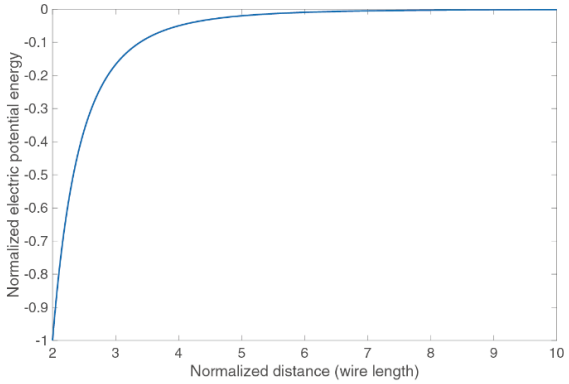
Normalized electric potential energy
0
-0.1
-0.2
-0.3
-0.4
-0.5
-0.6
-0.7
-0.8
-0.9
-1
2
3
4
5
6
7
8
9
10
Normalized distance (wire length)

Figure 7.6. The local confinement of chaining and long-ranged interaction. (a) the three wire dynamics showing the confinement of the nanowires in the middle of assembled chain. Scale bar is 10 μm. (b) The snapshots of a nanowire chain under 200 kHz rotating field with a time interval of 0.25 s. (c) The simulation result of a nanowire chain assembled from 10 wires. (d) the schematic of the orientation configurations between two nanowires. (e) the averaged electric potential energy over all possible orientation configurations between two nanowires as a function of the distance between two nanowire center.

The network formation and clustering occur under the condition when the induced dipole-dipole interaction is vital, i.e., under laser exposure and when the frequency is between 10 kHz to 200 kHz. We also want to dig more into the transition between these two types of collective behaviors. For both clustering and network formation, the dipole-dipole interaction is vital. There comes a natural question, why the network forms without further shrinking into clusters? We provide the following model of a nanowire chain assembled from more than three nanowires to understand it. As shown in Fig. 7.6a, when three wires assemble into a chain, although the yellow wire in the middle still experiences the rotational torque exerted by the field, the attraction force at the two tips from the neighboring two wires will cancel out the torque. For the wires at the ends of the chain, they have one end fixed to the neighboring wire, with the other end free to rotate under an external field. As a result, the blue and red wires will first rotate around the fixed tip. When they are $90°$ about the neighboring wire (yellow wire), the dipole-dipole interaction vanishes, and they are likely to dissemble from the chain. The snapshots in Fig. 7.7b shows the experimental result of one assembled nanowire chain with the two wires at the tips rotated around, and dissembled from the main chain when they are orthogonal. Our simulation also confirms such dynamics as shown in Fig. 7.7c. In the nanowire suspension, the density is so high, that the wires will quickly assemble with neighboring wires and eventually form a network. In the center area of the network, the nanowire chains do not have a free end to rotate along with under the field. As a result, although there might exist

long-range attraction forces from the dipole-dipole interaction that tend to make the nanowires shrink into some nucleation, they are too weak to overcome the energy barrier needed to break an assembled chain. On the other hand, at 10 kHz, the rotational torque is more substantial and prohibits chain formation. The nanowires can freely spin around their own geometrical center accompanied by the strong dipole-dipole interaction. As previously shown in Fig. 7.2a,b, the dipole-dipole interaction between two wires can be either attractive or repulsive depending on the arrangement. When the wires are freely spinning, one can reasonably assume that the relative angle between two wires is uniformly distributed in the range of $(0, \pi]$ (Fig. 7.7e). With this assumption, we can calculate the average electrical potential between two wires under the rotating electric field of all possible orientational arrangements as a function of the distance between two wires' center, as shown in Fig. 7.7f.

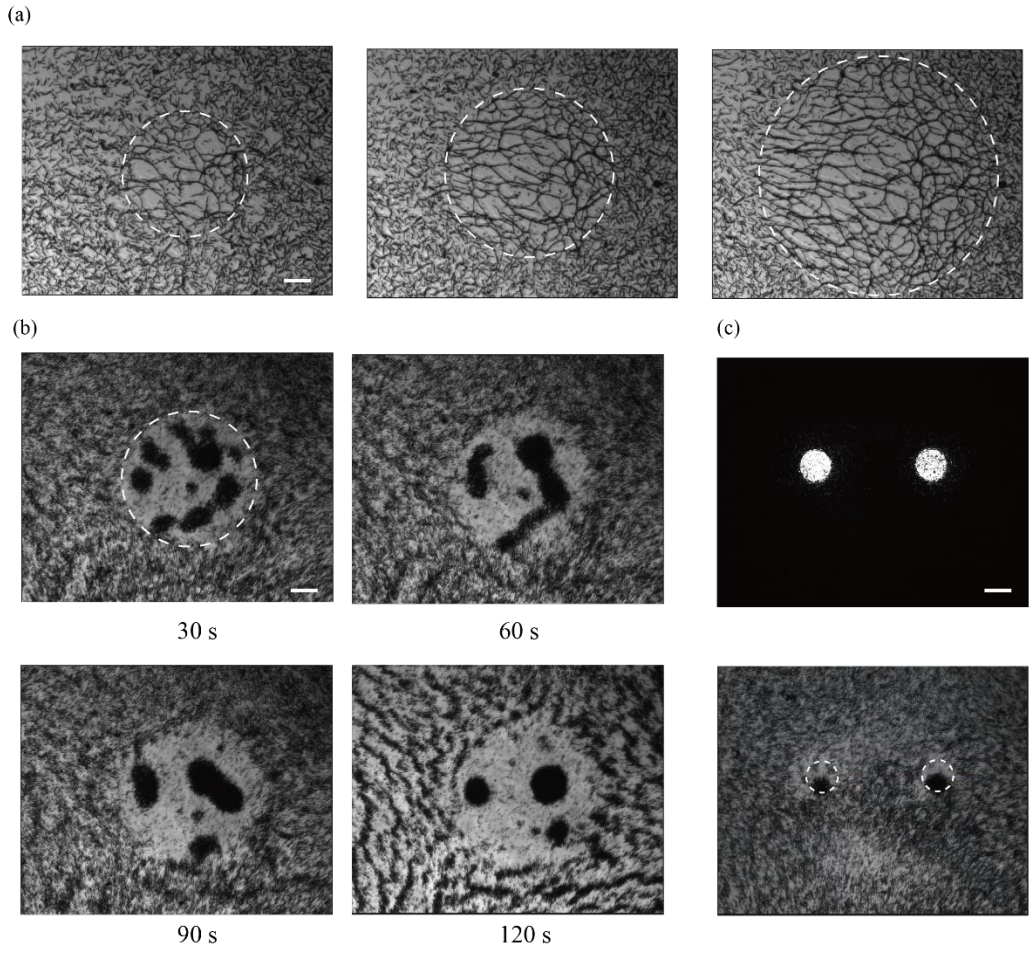

Figure 7.8. Localized formation of structured by programmable light patterning. (a) the network formation under three circular light pattern with increasing radius. (b) the snapshots of the clustering formation and evolution within a circular light pattern. (c) light pattern guided clustering. Scale bars are 50 μm.

One of the advanced features of this system is that the collective behaviors are only triggered under laser exposure. With the implementation of a digital light projection, we can project predefined light patterns onto the sample surface with high resolution and realize localized pattern formation on purpose. As shown in figure 7.8a, three circular light

patterns of various sizes can effectively guide the local network formation without affecting the unexposed area. Similarly, a circular pattern was projected onto the nanowire suspension under an electric field at 10 kHz. More than ten nucleation sites emerged within the exposed area, followed by a series of coalescence until three clusters left (Fig. 7.8b). The clusters cannot further grow as the nearby nanowires have been depleted already and are insufficient to form a cluster as large as the light pattern. However, if we reduce the size of the light pattern, it is possible to form one single cluster in the pattern. As shown in Figure 7.8c, with two small circular light patterns, two nanowire clusters form at the exact location of the light pattern. These demonstrations confirm that we can control the local formation of the network within a specific area and the nucleation location of clustering by projecting properly defined light patterns.

7.2. Discussion

In this work, we have introduced a new system that shows collective behaviors from silicon nanowire suspension driven by rotating AC electric field with light modulation. The combination of non-spherical silicon nanowire and the rotating electric field correlates the orientation of nanowires to the phase of field and enables a special kind of dipole-dipole interaction that can generate unique collective behaviors. Due to the silicon nanowires' semiconductive properties, laser exposure can induce photo-excited carriers in the nanowire and cause significant enhancement in the polarization as well as modulating the fraction of the imaginary part of polarization. We observed two different collective behaviors at two different frequency regions, the formation of the 2D network and the clustering. The working principle of the 2D network formation is similar to many previously reported works where colloidal particles are assembled into a chain via in-plane dipole-dipole interaction. However, we utilized a rotating field at high frequency so that

the chain can form in arbitrary orientation, and resulting in a highly branched 2D network. Clustering is also one of the most representative collective behavior that has been extensively studied in many other systems. For non-self-propelled particles to form clusters, a long-ranged attractive interaction is essential. In our system, this attraction comes from the dipole-dipole interaction. When nanowires are freely spinning, the orientation of wires can be regarded as randomly distributed, and the dipole-dipole interaction in average over all possible configurations turns out to be attractive at long-range. As a result, the wires are attracted towards the area with high nanowire density and eventually form clusters with the circular periphery.

On the other hand, we want to clarify that although we have reproduced the clustering with intense polarization with a high fraction of imaginary part, we are not able to understand why the clustering occurs at low frequencies, yet not observed at 500 kHz-1000 kHz high-frequency range, where both the imaginary part of polarization and total polarization are also substantial. We believe this discrepancy is attributed to the electroosmosis flows that are much stronger at 10 kHz yet almost vanish above 500 kHz. At high frequencies, the flow around the nanowire is solely disturbed by the mechanical motion of the nanowire. On the other hand, at low frequencies, i.e., 10 kHz, the flow results from mechanical motion and the induced-charge-electro-osmosis (ICEO) flow. We believe that the electrokinetic phenomena such as the formation of electrical double layer and ICEO at low frequency must play some roles in facilitating the long-range attraction between the nanowires so that the clustering patterns occur. In future studies, these effects should be considered to obtain a more quantitative understanding of the clustering phenomena. Both of these two types of patterns are triggered within the area that is under laser exposure. With a digital light projection system, we demonstrated the localized formation of patterns guided by predefined light patterns. This unique feature of the system

offers substantial advantages for both fundamental study and application-oriented study in the future, as the light patterning allows a versatile approach to control the pattern formation with high spatial resolution. For example, the light guided the formation of a semiconductor network that may be used for the assembly of electronic devices in the future. The programmable light projection can be regarded as tunable boundary conditions of the system that is convenient for the fundamental study of the collective behavior without changing the physical boundary of the system.

Chapter 8: Application of Rotary Micro Motors for Biosensing

In this section, we demonstrate that the locomotion from previously discussed rotational micromotors facilitates the sensing speed for practical applications. Here we report the design, fabrication, and application of a rotary micromotor-sensor system for robust augment of capture and detection speed of biomolecules, *i.e.*, salmon sperm DNA, with Surface Enhanced Raman Scattering (SERS) spectroscopy. The sensitive, durable, and position-stable rotating sensors continuously monitor the dynamic capture process of DNA molecules *in situ* and in quasi-real-time. The rotation notably accelerates the capture efficiency of the DNA molecules by at least 4 folds at 1200 rpm, and boosts the detection speed of low-concentration DNAs (80 nM) by 3 times at 630 rpm. Theoretical analysis and modeling unveil the working mechanism, governed by the complex molecule-motor-flow interaction, and suggest its application range.

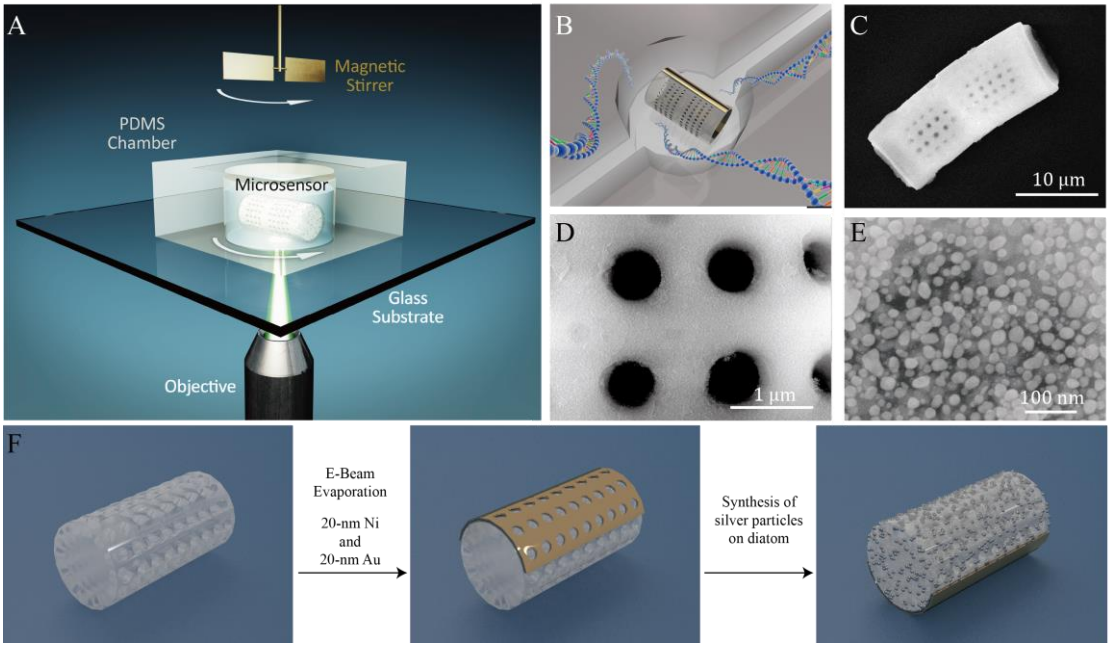

Figure. 8.1. Design and fabrication of the optoplasmonic micromotor-sensors. (A-B) Schematic of a rotating biosilica opto-plasmonic microsensor in a well with DNA molecules. (C-D) Scanning electron microscopy (SEM) images of the diatom frustules with periodic nanopores, and (E) the dense surface-distributed Ag nanoparticles. (F) Schematic fabrication workflow.

8.1. Photonic-Crystal Enhanced SERS Detection of DNA

A bioenabled opto-plasmonic enhanced micromotor-sensor is designed consisting of a diatom frustule as the sensor body, uniformly distributed plasmonic Ag nanoparticles on the surface for SERS biodetection, and a thin magnetic film deposited on the side for magnetic actuation [Fig. 8.1A-B]. Diatoms are one of the most common and widespread types of photosynthetic microalgae, living abundantly in marine ecosystems. Frustules are the cell walls of diatoms made of silica with ordered arrays of nanopores [Fig. 8.1C-D]. These naturally existing and widely available biomaterials exhibit high mechanical strength and chemical stability, which suggest feasible applications as micro/nanomechanical devices.[115] The periodic nanopore structures on the surface work as natural photonic crystals that can interact with light and induce guided-mode resonance.[116,117] The guided-mode resonance can further couple with the plasmonic Ag nanoparticles and enhance the localized surface plasmon. Such photonic-crystal-plasmonic resonance can substantially boost SERS signals for ultrasensitive molecule detection.[118] The high mechanical strength, and chemical stability, low cost and the photonic structure make the diatom frustule a great material for various applications.[119-121]

The detail of the fabrication of the above designed microsensor is discussed in the section of Materials and Methods. Briefly, to fabricate well-reproducible and high-quality micromotor-sensors, we disperse, sonicate, filter, and calcinate commercially-available diatomaceous earth powder to produce refined diatom frustules.[115] These processes remove

both organic and inorganic impurities and broken pieces of frustules and deliver purified cylindrical diatom frustules with diameters of 8- 16 μm and lengths of 20 to 35 μm [Fig. 8.1C]. Next, A bilayer nickel (Ni)/gold (Au) thin film is deposited on one side of the diatom frustules with electron-beam evaporation for magnetic manipulation. Then, high-density arrays of plasmonic Ag nanoparticles are synthesized uniformly on the surface of the diatom frustules for SERS detection [Fig. 8.1E].[122,123] The average diameter is 23.38±3.30 nm and the junction ranges from 0.5 nm to 5 nm.

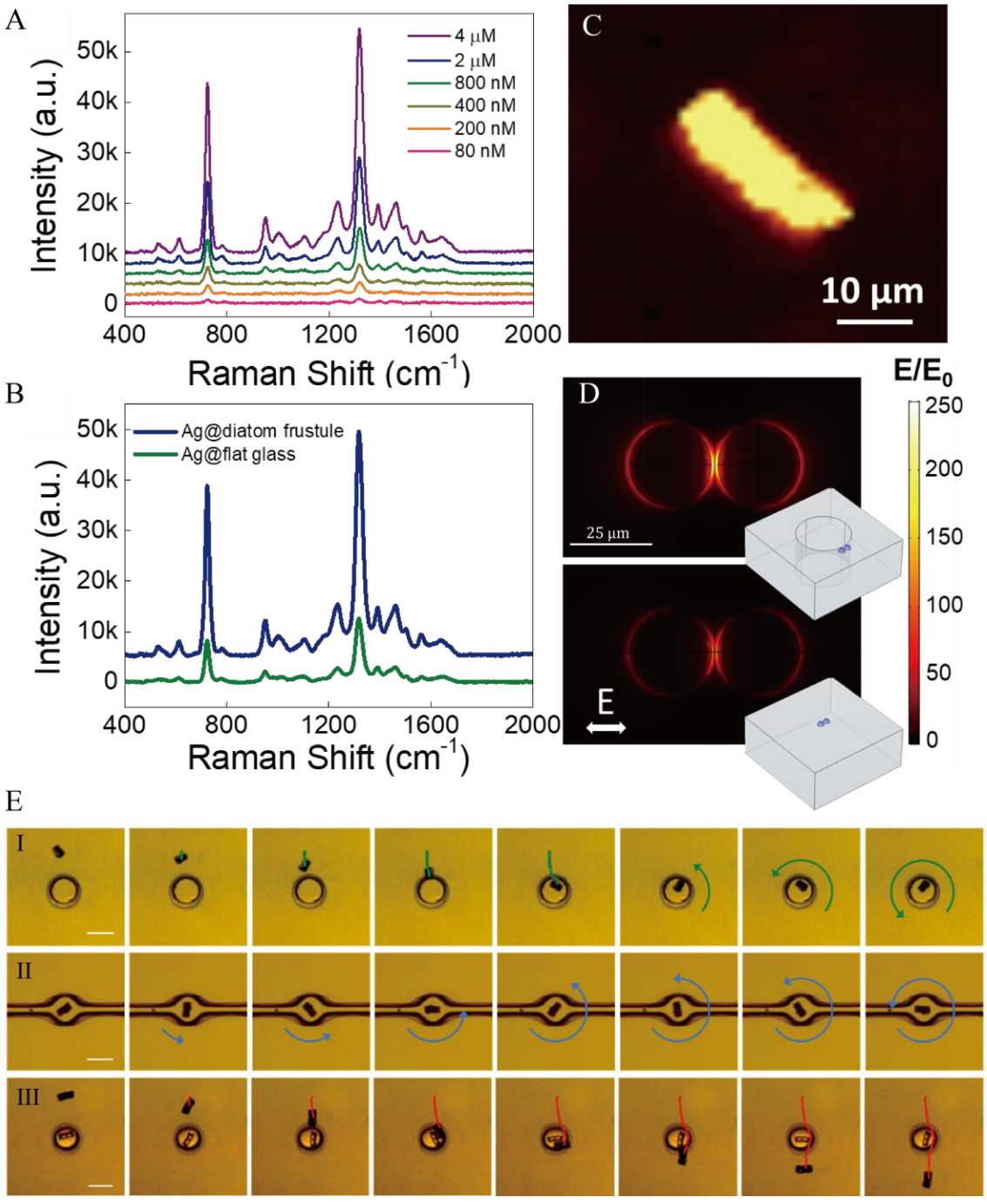
A
Intensity (a.u.)
50k
40k
30k
20k
10k
0
400
800
1200
1600
2000
Raman Shift (cm-1)
4 μM
2 μM
800 nM
400 nM
200 nM
80 nM
C
10 μm
B
Intensity (a.u.)
Raman Shift (cm-1)
Ag@diatom frustule
Ag@flat glass
D
25 μm
E
E/E0
250
200
150
100
50
0
E
I
II
III

Figure 8.2. Surface enhanced Raman spectroscopy with the micromotor-sensors and their rotation-assisted assembly in microfluidic wells. (A) SERS spectra of DNA molecules of 80 nM to 4 μM. (B) Comparison of SERS spectra of DNA molecules (4 μM) on a microsensor (in blue) and on an Ag-nanoparticle coated flat glass substrate (in green). (**C**) Raman mapping of DNA molecules (4 μM, 724 cm^{-1}) on a microsensor (2-hour incubation) shows signals with good uniformity. (**D**) Simulations of electric-field distribution around a pair of Ag nanoparticles placed on a diatom frustule (top) and flat glass (bottom). Insets: schematics of the respective structures with a pair of Ag nanoparticles. Incident laser is horizontally polarized. (**E**) I. A micromotor-sensor rotating and assembling into a microwell (Snapshots: every second in the first 5 seconds and then every 0.05 seconds). II. A micromotor-sensor stably rotates in a microfluidic channel (snapshots: every 0.025 seconds). III. A micromotor-sensor rotating at 300 rpm detoured around an occupied microwell (snapshots: every second, scale bar 30 μm).

Next, we characterized the Raman sensitivity of the microsensors by testing Salmon sperm DNA molecules. A 532 nm laser of 500 μW and 25 μm in diameter is utilized as the excitation source. At this intensity, laser-heating effect in enhancing the capture dynamics of the molecules is not observable as shown by the control experiments and simulation. Among various important biomolecules, DNA molecules are chosen due to their significant roles in medical diagnosis, treatment, and forensic investigation.[124,125] It also due to the large size and low-diffusivity of many DNA molecules that suffer notably difficulties in high-efficiency detection. As shown in Fig. 8.2A, after incubation in DNA solutions of 80 nM to 4 μM for 2 hours, we can detect their signals with a concentration as low as ~80 nM with an averaged signal-to-noise ratio of 5 at 724 cm^{-1} and 1319 cm^{-1} (both from the vibration of nucleobase adenine).[126] The Raman intensity monotonically increases with the DNA concentration with a largely uniform enhancement along the length of the microsensors [Fig. 8.2C]. It was determined that the enhancement factor is up to ~ 10^9 to 10^{10} on the surface of Ag-nanoparticle-dispersed substrate fabricated with the same method and morphology.[122,127] Moreover, compared to Ag nanoparticles grown on a flat glass substrate at the same condition, the Raman intensity shows additional improvement on the

plasmonic diatom-frustule motor as high as 3.66 ± 0.31 folds across all the major DNA peaks [Fig. 8.2B], *i.e.* 724 cm^{-1} (adenine), 957 cm^{-1} (deoxyribose moiety), 1235 cm^{-1} (thymine and cytosine), 1319 cm^{-1} (adenine) and 1391 cm^{-1} (guanine).[126,128] As shown in the numerical simulation in Fig.8.2D, at least 1.98 time increase in the electric-field intensity is found for a pair of Ag nanoparticles placed next to a nanopore compared to that on a flat glass substrate (Materials and Methods). This value can be higher as the Ag nanoparticles are grown on a 3D surface. Furthermore, since the plasmonic Ag nanoparticles offer orders-of-magnitude Raman enhancement, while such enhancement only presents in the vicinity of the Ag nanoparticles and their narrow junctions, the so-called hotspots, we can safely consider that only the DNA molecules on the surface of the micromotor sensors are detected. The DNAs in the background suspension without the plasmonic enhancement essentially have no contribution to the collected Raman signals [Fig. 8.2C]. Therefore, we can readily monitor the dynamic capture process of the DNA molecules by the solid surface *in-situ* and in quasi-real-time owing to the near-field effect of SERS.

8.2. Mechanical-Rotation-Enhanced Detection of DNA

To detect biomolecules in a position-deterministic and robust manner for duration sensing, the as-obtained micromotor-sensors are integrated into individual microwells (or microchannels) *via* self-assembly assisted by magnetic rotation. Here, a tunable rotating magnetic field is applied above the microsensors dispersed on the microfluidic device with arrays of microwells as shown in Fig. 8.1A. A magnetic stirrer, commonly used in chemistry and biology labs, provides the magnetic field. The upward direction and tunable magnitude of the magnetic-field-gradient balance the gravitational force and effectively

reduce the hindering force from the substrate. This setup ensures stable and durable rotational actuation of the micromotor-sensors. It is particularly useful for the capture and detection of various biomolecules in suspension with complex composition and high ionic ingredients in which the substrate sticking problem may occur.

It is found that with an applied magnetic field (***B***), all dispersed micromotor-sensors rotate at a synchronous speed that can be controlled up to 1200 rpm. The driving magnetic torque is given by $\boldsymbol{\tau_m} = \boldsymbol{m} \times \boldsymbol{B}$, where $\boldsymbol{m}$ is the magnetic moment of a micromotor-sensor. During the rotation, the microsensors slowly move on the Polydimethylsiloxane (PDMS) film and assemble into individual microwells (30 μm in diameter and 10 μm in height) [Fig. 8.2E]. Importantly, the assembly is accomplished in a one-on-one fashion: when one micromotor-sensor encounters a microwell that has already been occupied by a rotating microsensor on its moving path, it detours around and moves forward. The one-on-one assembly can be robustly obtained owing to the fluidic repulsion between two close-by rotating motor sensors,[107] which is critical for long-time and reliable molecule capture and SERS detection.

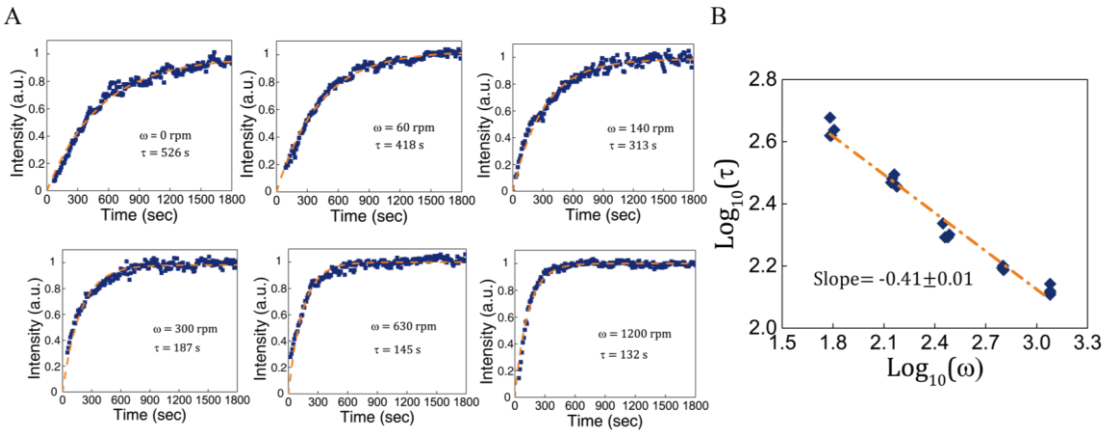

Figure 8.3. Dynamics of the mechanical-rotation-accelerated capture of DNA molecules revealed by SERS. (A) Time dependent DNA capture (4 μM) by a microsensor with various rotation speeds. (B) Log-log plot of the characteristic DNA capture time (in second) *versus* rotation speed (ω in rpm). The linear fitting from 60 rpm to 1200 rpm shows a slope of -0.41.

With all the above efforts on the design, fabrication, sensing characterization, and the one-on-one assembly of individual rotary sensor-in-well devices, we are ready to study how controlled mechanical rotation can change the capture and detection efficiency of DNA molecules. Albeit mounting efforts on the optimization of the binding buffers [129-131] and substrates,[132-134] the efficiency in DNA capture remains poor, particularly for analytes of low concentrations.[135] It can take tens of minutes to several hours to reach a capture saturation for DNA molecules binding to silica surface, when the dynamic absorption rate equals to the desorption rate.[136,137]

Now, we monotonically increase the rotation speed of the individually assembled micromotor-sensors up to 1200 rpm and detect the Raman signals simultaneously. The DNA capture process is continuously monitored quickly after adding a mixed sample into the testing microwell with Raman signals taken every 10 seconds for 30 minutes from a rotating diatom microsensor. The Raman intensity of DNA molecules increases

monotonically until it reaches a plateau on the microsensors as shown in Fig. 8.3(A). We found that the mechanical rotation clearly accelerates the DNA capture and enrichment process. For instance, the required time to reach 95% of the capture equilibrium of DNA is reduced from ~ 28 minutes on a static microsensor, to ~ 7 minutes on a rotating microsensor at 1200 rpm, which is a 4-fold improvement [Fig. 8.3A]. Even at a speed of 300 rpm, the capturing process only requires 1/3 of the capture time of that with a static microsensor. We further obtain the characteristic time (τ) at different rotation speed (ω) by fitting the time-dependent Raman Intensity of DNA [Fig. 8.3A] with an exponential function given by $I = I_0\left[1 - \exp\left(-\frac{t}{\tau}\right)\right]$, and then plot the log-log dependence of τ *versus* ω [Fig. 8.3B]. It is found that the characteristic time τ monotonically decreases with the rotation speed ω from 60 rpm to 1200 rpm, with a power-law dependence of $\tau \sim \omega^{-0.41\pm0.01}$. The above series of experiments clearly evidence that the capture speed of DNA molecules indeed can be enhanced with mechanical rotation. To understand the mechanistic role of mechanical rotation in the enhancement of molecule capture, we carried out theoretical analysis and modeling. The results are implemented to shed light on this DNA molecule-motor-fluid system to be discussed as follows.

8.3. Theoretical Analysis and Modeling

Reaction-Diffusion-Convection Kinetics: The understanding of transport and reaction of diluted analyte molecules with their receptors is critical for the understanding of the working mechanism and limits of the motorized micro/nanobiosensors. Great efforts have been spent on investigating the kinetics of such reaction-diffusion-convection systems from both the experimental and theoretical perspectives.[138-140] Three important interactive

processes can be identified that govern the molecule capture kinetics by a solid surface, *i.e.*, the convection of analyte molecules driven by the flow, the diffusion of the analytes towards the solid surface, and the reaction on the solid surface [Fig. 8.4A]. When hard limits occur, it is usually one of the three processes becoming the rate-determining step. Thus, determining the rate-limiting process is essential for lowering the barrier towards a better performance.

When a fluidic flow is introduced into a system, the convection term of mass transport must be added into the transport equation in addition to the Fick's second law given by Equation (1):

$$\frac{\partial \mathrm{c}}{\partial \mathrm{t}} = \mathrm{D}\nabla^2 c - \mathbf{v} \cdot \nabla \mathrm{c} \tag{8.1}$$

where *c*, *D*, and *v* are the concentration of molecules, diffusion coefficient, and flow velocity, respectively. Convection is generally more effective in mass transport compared to that of the passive diffusion for most molecules.

To quantitatively solve the above complex convective-diffusion problem at low Reynolds numbers and to understand the behavior of our experimental system, our strategy is to divide the modeling into two sub-problems. First, we utilize numerical simulation to compute the convection-diffusion dynamics to study the diffusion boundary layer thickness as a function of the external flow rate. Here, we inherit the concept of the Nernst Diffusion Layer with a small modification. Nernst assumed a layer with thickness δ_D in which only the diffusion occurs in a moving liquid. This layer is static and in the immediate vicinity of the solid surface. Beyond this layer, molecule concentration is constant as same as that of the bulk due to external convection. The clear physics picture provided by Nernst's theory, however, does not allow quantitative computation due to the unnatural definition of the boundary. In order to quantitatively determine the diffusion layer thickness with

numerical simulation, in the frame of the Nernst-Diffusion-Layer model, we define the outer boundary of the diffusion layer wherever the concentration of the analyte equals to 90% of the bulk concentration. Then, we study a 1D reaction-diffusion kinetic problem within the static diffusion layer, without the convection term. In our treatment, the convection plays the role in influencing the diffusion layer thickness; within the diffusion layer, the molecule transport dynamics is solely governed by the diffusion and reaction processes. We believe this strategy, differing from other works, can offer a clear physics picture of the role that each factor plays in the system for the understanding of the underlying working mechanism of the experimentally observed mechanical-motion-enhanced detection of DNA molecules.

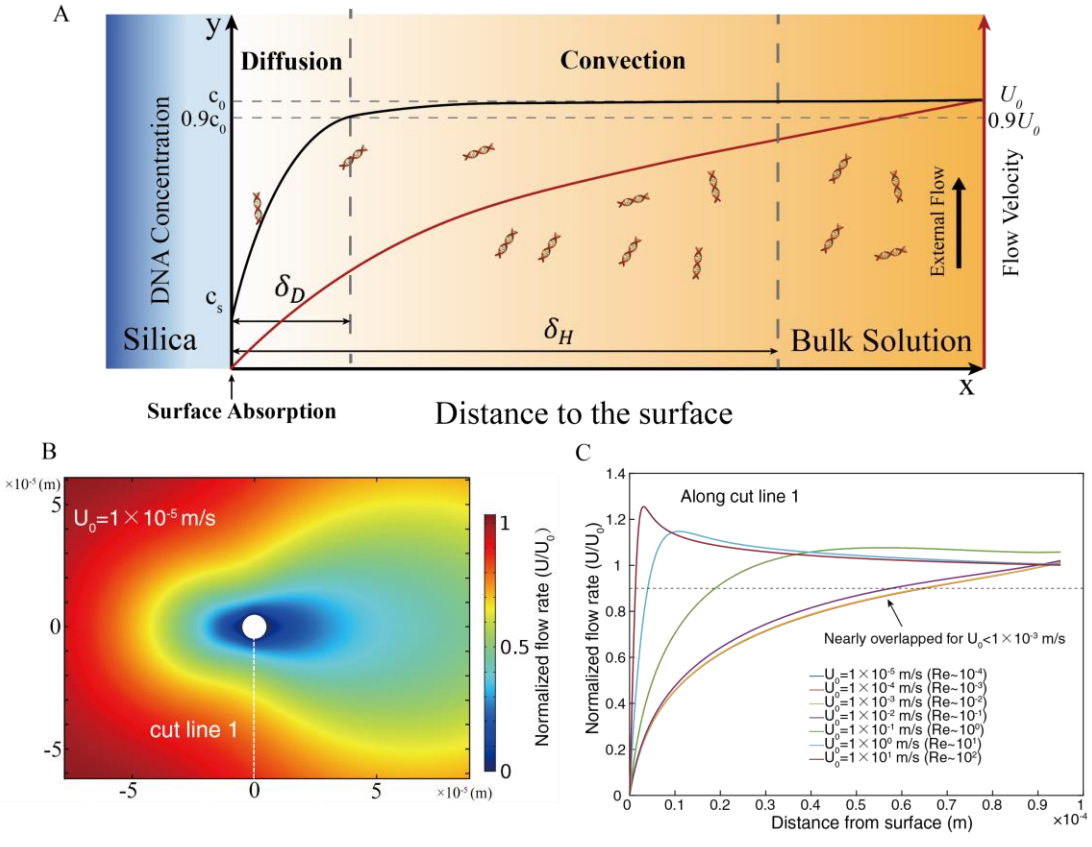

Figure 8.4. (A) Diagram of the DNA capture process involving reaction on a solid surface, diffusion and convection. (B) The profile of laminar flows passing across a circular cylinder (cross-section view) at a low Reynolds number of 1×10^{-4}. (C) Flow rate along the cut line 1 with various external flow rates (U_0).

Diffusion-Convection Kinetics: in the first step, we simplify the 3D model of a self-spinning microsensor to a 2D problem of laminar flow passing across a circular cylinder of 10 μm in diameter as shown in Fig. 8.4B. The flow rate is varied from 10^{-5} m/s to 10 m/s, which corresponds to a Reynolds number from 10^{-4} to 100. The flow rate profile is mapped along the cut line 1 as shown in Fig. 8.4C. On the surface, due to the none-slipping boundary condition, the flow rate is always zero. With the increase of the distance from the cylinder, the flow rate monotonically increases to 90% of the external flow rate U_0, the location of which is defined as the outer edge of the hydrodynamic boundary layer with a thickness of δ_H. For systems with a Reynolds number Re $>10^{-2}$, the dimensionless flow profile changes significantly, the increase of the external flow rate U_0 results in the decrease of δ_H, and at high Reynolds numbers, the dependence of δ_H on U_0 approximates to $\delta_H \sim U_0^{-0.5}$ as predicted by the Prandtl's boundary layer theory.[141] On the other side, at a low Reynolds number, *i.e.*, a system with $\mathrm{Re} \leq 10^{-3}$, the normalized flow profiles remain largely the same, indicating that the hydrodynamic boundary layer thickness δ_H is independent of the external flow rate at an extremely low Reynolds number, which is a characteristic of a Stokes flow.

Although the flow profiles after normalization by the external flow rate U_0 are almost identical for various flow rates when $U_0 < 1 \times 10^{-3}$ m/s, the convection term in equation (8.1), which is directly proportional to the flow rate, can be enhanced. Here, we further simulate the convective diffusion of DNA, carried by an external flow ranging from

1.00×10^{-5} m/s to 2.51×10^{-3} m/s passing around the same cylinder with a fast reaction boundary condition $c = 0$ at the cylinder surface, and assume that the incoming flow carries the same concentration c_0. The concentration profile is probed when the system is fully developed [Fig. 8.5A-C]. In particularly, we monitor the concentration profile along the cut lines 1, 2 [Fig. 8.5A] under different external flow rates as shown in Fig. 8.5D-E. The concentration profile is significantly altered by the flow. With the increase of the external flow rate U_0, the concentration gradient increases, and the thickness of the diffusion boundary layer (δ_D) decreases accordingly. This result indicates that even in a low Reynolds number region, the enhancement of convection in mass transport by flow is still effective and practically useful. We summarize the result of both the hydrodynamic boundary layer thickness (δ_H) and diffusion boundary layer thickness (δ_D) as a function of the external flow rate in Fig. 8.5F. The fitting of diffusion boundary layer δ_D as a function of the external flow rate U_0 determines a dependence of $\delta_D \sim U_0^{-0.349\pm0.015}$ at the front side, and $\delta_D \sim U_0^{-0.341\pm0.022}$ on the top and bottom of the cylinder. The slight difference among different locations on the cylinder allows us to adopt an average value to represent the dependence as $\delta_D \sim U_0^{-0.344\pm0.020}$ for further analysis.

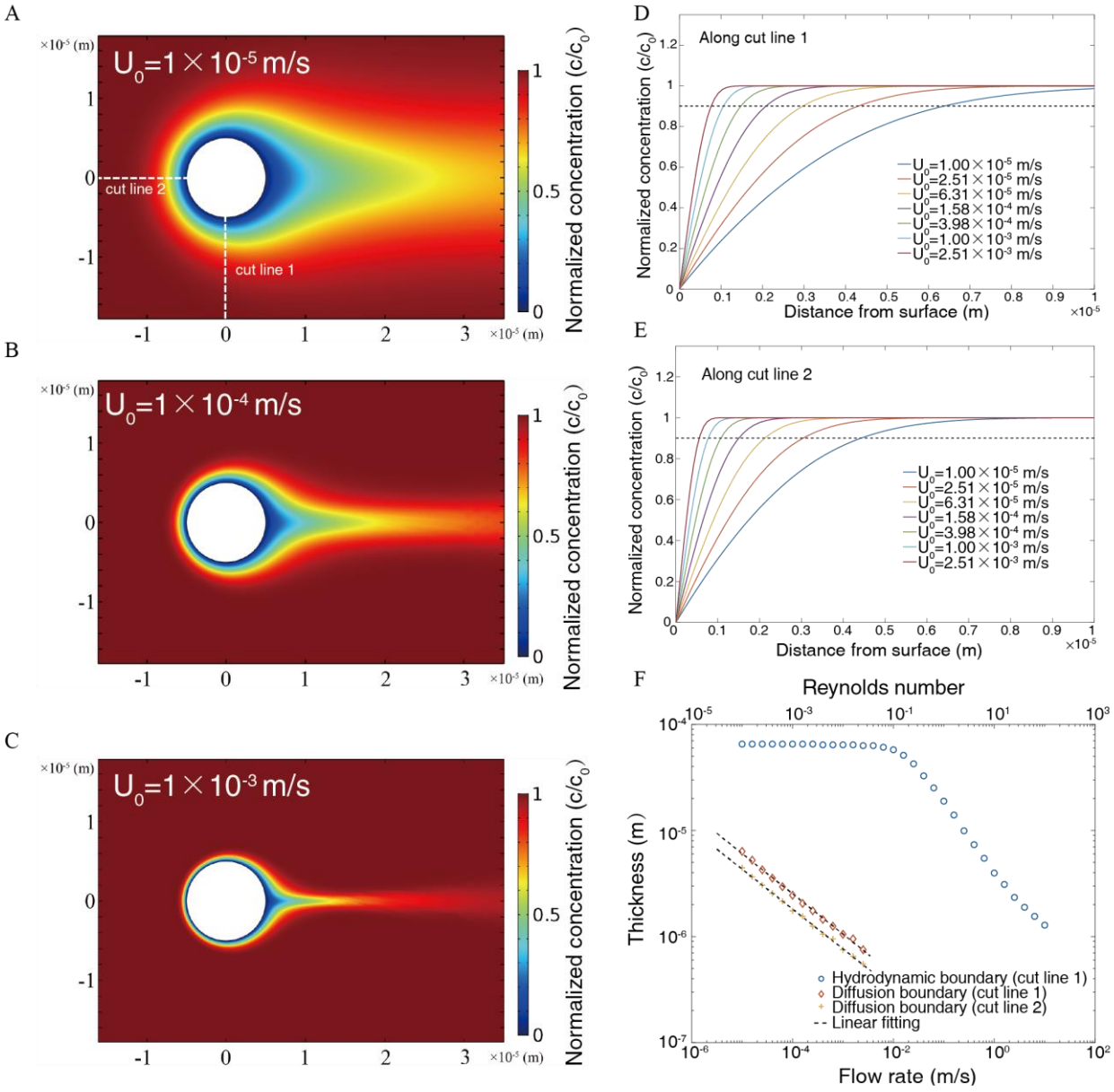

Figure 8.5. Simulation of the convective diffusion at low Reynolds numbers. (A-C) Concentration profile of laminar external flow with various flow rates U_0 carrying DNA molecules passing around a reactive cylinder surface with zero concentration. (D) Normalized concentration along cut line 1 under different external flows and (E) along cut line 2. (F) Thickness of hydrodynamic (in blue) layer and diffusion boundary layer (in red) *versus* flow rate.

Reaction-Diffusion Kinetics: in the above, we model the convection-diffusion dynamics with a simplified fast reaction boundary condition to extract the impact of external flows to the thickness of the hydrodynamic and diffusion layers. The obtained power dependence on flow rate is valid not only for fast reaction conditions but also for the conditions when the surface reaction does not consume all transported molecules. Next, we start the investigation of a 1-D molecule reaction-diffusion system without convection (the effect of convection has been considered by the dependence of δ_D on U_0). The system consists of a reactive solid surface, *i.e.,* the silica surface of the micromotor sensor, which captures DNA molecules *via* adsorption, as well as a diffusion boundary layer with thickness of δ_{D}, across which the concentration of DNA can vary with time (*t*) and position (*x*). We apply the following Fick's second law:

$$\frac{\partial c}{\partial t} = \mathrm{D}\nabla^2 c \tag{8.2}$$

where *c* and *D* are the volumetric concentration and diffusion coefficient of the DNA molecules, respectively. To solve this equation, two boundary conditions are required at the edges of the domain of interest. The first boundary condition at the outer edge of the diffusion boundary layer is given by: $c = c_0$, at $x = \delta_D$. The second boundary condition involves the surface reaction at the silica/solution interface. Given the mass conservation, the flux of the analytes going towards the surface has to be equal to the instantaneous adsorption rate of analytes at the surface, which can be written as: $\frac{\partial \mathrm{n}}{\partial \mathrm{t}} - \mathrm{D}\frac{\partial \mathrm{c}}{\partial \mathrm{x}} = 0, at\ x = 0.$ Here we assume that Fick's first law is valid at low concentration and define a surface adsorption density as n, which is the number of absorbed DNA molecules per unit area by the silica surface. Here, the surface adsorption kinetic can be described by the Langmuir isotherm as follows:

$$\frac{\partial \mathrm{n}}{\partial \mathrm{t}} = k_a(n_{max} - n)c_s - k_d n \tag{8.3}$$

where k_a, n_{max}, c_s, and k_d are the adsorption coefficient, maximum surface adsorption density, surface concentration of analyte molecules in the solution immediately next to the solid surface, and desorption coefficient, respectively (more details in Appendix B).

To get insights of the reaction-diffusion kinetics, we further non-dimensionalize the equations (8.2-8.3) and numerically solve the 1D reaction-diffusion problem with the finite-differential-time-domain (FDTD) method (Details in Appendix B). The results determine that the molecule transport kinetics depends on the Damköhler number of the system, which is defined by the ratio of the reaction and diffusion rates given by $Da = \frac{\delta_D n_{max} k_a}{D}$. When the system reaches an equilibrium, the surface concentration c_s becomes c_0, and the surface density is given by $n_{eq} = \frac{k_a n_{max} c_0}{k_a c_0 + k_d}$. Let $\tilde{c} = \frac{k_a c_0}{k_d}$, n_{eq} can then be written as $n_{eq} = \frac{\tilde{c}}{1+\tilde{c}} n_{max}$. In the simulation, the range of the Damköhler number is selected from $0.001\ to\ 1000$ that covers the surface-adsorption-reaction limited process when it is ultrasmall, *i.e.*, $Da \ll 1$, and the diffusion limited process when it is large, *i.e.*, $Da \gg 1$.

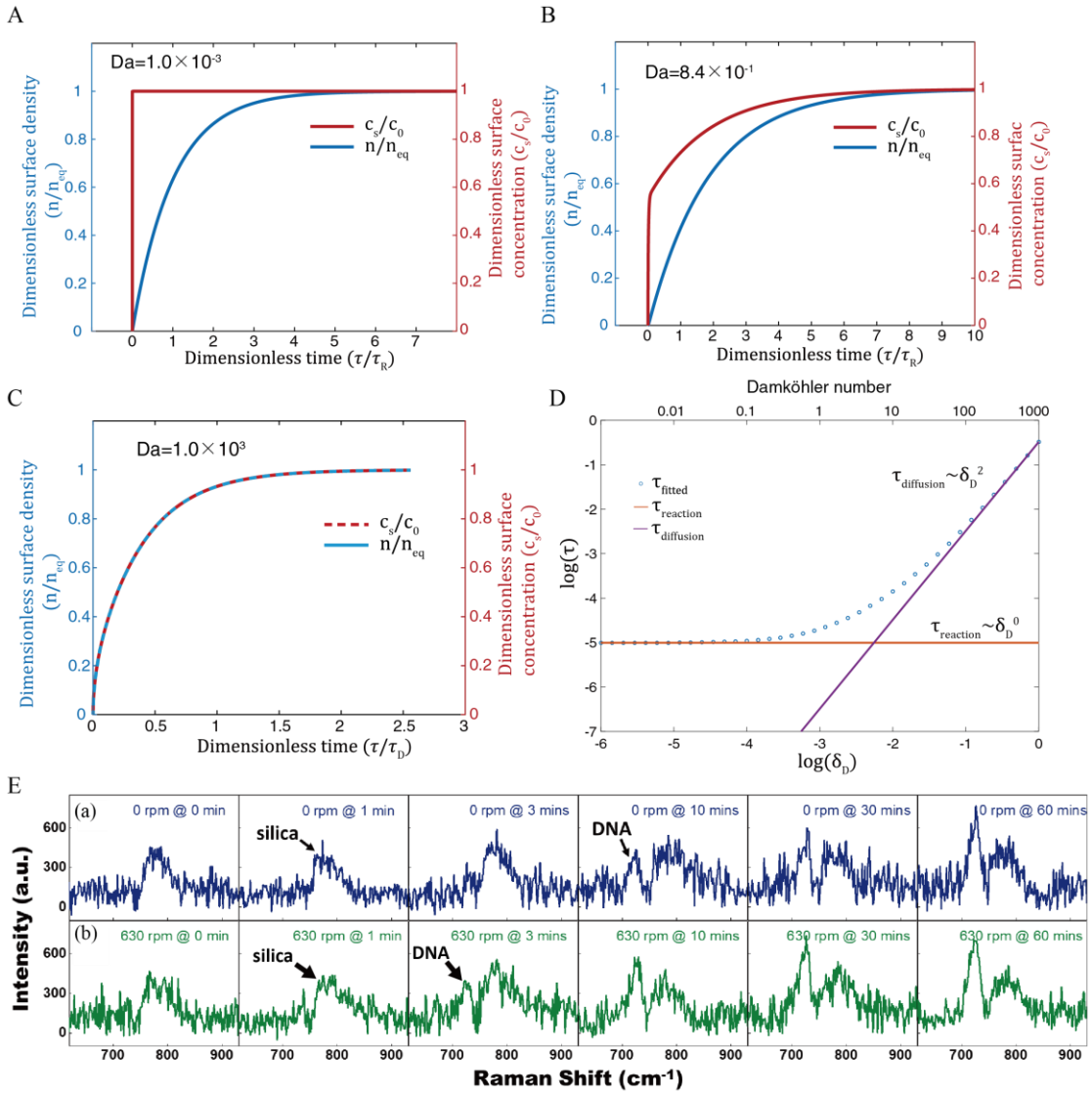

Figure 8.6. Simulation of the reaction-diffusion kinetics at different Damköhler numbers and demonstration of rotation accelerated detection of low-concentration DNA molecules. (A-C) The evolution of surface adsorption density and surface concentration with (A) Da=0.001, (B) Da=0.84, and (C) Da=1000. (D) The characteristic time scale of the reaction-diffusion process obtained by fitting at different thickness of diffusion layer. (E) Raman spectra of low-concentration DNA molecules (80nM) measured at fixed time intervals for an hour on (a) a static (in blue) and (b) on a rotating microsensor at 630 rpm (in green).

Three sets of representative systems with Da numbers of 10^{-3}, 8.4×10^{-1} and 10^{3} are evaluated to show the evolution of both the molecular surface adsorption density (n) (in blue) and concentration of molecules next to the surface (c_s) (in red). At Da=10^{-3}, when the system is in the reaction-rate limited regime, the diffusion process quickly reaches equilibrium as shown by the steep profile like a step function in red [Fig. 8.6A]. Due to the low reaction speed, the surface density of molecules *versus* time (n) follows an exponential function given by $n(t) = n_{eq}[1 - \exp\left(-\frac{t}{\tau_R}\right)]$, where $\tau_R = \frac{1}{k_d(1+\tilde{c})}$. At Da=$10^{3}$, the time-dependent dimensionless n/n_{eq} and c/c_s essentially overlap [Fig. 8.6C]. This is a result of the diffusion-limited process, in which the reaction goes through a quasi-static process controlled by the speed of the diffusion. Here, the molecular concentration gradient is the driving force of the diffusion flux that n/n_{eq} is always close to but slightly lower than c/c_s in the same time scale. Finally, for a system with an intermediate Da number of 0.84, the reaction and diffusion rates are comparative, and the kinetics is governed by both diffusion and reaction [Fig. 8.6B].

We further calculate the characteristic time of molecule transport (τ) at different Da numbers for a system, where δ_D is the only varying parameter that can be changed by an external flow speed. The value of τ is obtained *via* fitting the time-dependent molecular surface density (n) with $\frac{n}{n_{eq}} = 1 - \exp\left(-\frac{t}{\tau}\right)$ as shown in [Fig. 8.6D]. When the diffusion layer is thin that corresponds to a small Da number and a reaction-limited process, the value of τ is essentially a constant (red tangent line in [Fig. 8.6D]). This agrees with our earlier discussion that the reaction time constant is given by $\tau_R = \frac{1}{k_d(1+\tilde{c})} \sim \delta_D^0$, independent of δ_D. With the increase of δ_D, the process becomes diffusion dominated and τ scales with ${\delta_D}^2$ as given by the time constant of diffusion $\tau_D = \frac{\delta_D^2}{D}$, shown by the purple tangent line and data points at the high Da-number region. In between the two extremes, $\tau \sim \delta_D^p$, and

the power coefficient p ranges from 0 to 2. From the above, it can be found that the molecular transport dynamics in a diffusion-reaction system highly depends on the thickness of the diffusion layer that can be modulated by external flows.

8.4. Implement the Modeling towards Understanding the Experimental Observation

The above modeling can be readily applied to provide insights to our experimental results. As shown in Fig. 8.3, we observed acceleration of DNA capture by the rotating microsensors. The fitting shows that the characteristic time (τ) follows a power-law dependence of $\tau \sim \omega^{-0.41\pm0.01}$ on the rotation speed ω. Since the highest rotation speed tested in the experiment is 1200 rpm, corresponding to a Reynolds number of approximately 0.01, all the experimental conditions are within the low Reynolds number region. Therefore, for our system it is feasible to use the dependence of $\delta_D \sim U_0^{-0.34\pm0.03}$ as shown in Fig. 8.6F. Also, because the external flow rate U_0 is proportional to the rotation speed ω, we can readily obtain $\delta_D \sim U_0^{-0.34} \sim \omega^{-0.34}$. Now, combining the dependence of $\delta_D \sim \omega^{-0.34}$ from the numerical simulation and $\tau \sim \omega^{-0.41}$ from the experiments, we can readily determine the dependence of $\tau \sim \delta_D^{1.21}$, which corresponds to a Damköhler number of 20. This Da number indicates that the overall rate-limiting step is the diffusion process in this DNA capture system.

Therefore, the role of mechanical rotation can be understood. The rotation and the resulted flow convection effectively reduce the diffusion layer thickness (δ_D), and in turn increase the DNA diffusion rate, which is the kinetic limiting step of the overall reaction. The rotation, as a result, can be utilized to substantially increase the capture efficiency of DNA molecules. The higher the rotation speed, the narrower the diffusion layer, and the

greater the capture efficiency. Since the value of the demonstrated Damköhler number of around 20 still has room to improve, we expect the DNA capture speed can be even more enhanced with higher rotation speed.

Finally, with the above understanding, we further demonstrate the enhancement of detection efficiency of low-concentration DNA molecules by mechanically rotating a micro/nanosensor. DNA samples at 80 nM are tested on both static and rotating microsensors as shown in [Fig. 8.6E]. The speed of rotation is 630 rpm. Fig. 8.6E presents the obtained time-dependent Raman spectra of DNA molecules. The Raman peak at ~780 cm^{-1} from silica remains constant during the detection showing the invariance of the sensitivity of the microsensors under the mechanical rotation. The Silica peak is used as a reference for comparison with DNA signals. On the static microsensor, the Raman signal of DNA at 724 cm^{-1} can be hardly observed in the first 3 minutes and becomes gradually clear at ~ 10 minutes. From the rotating microsensor, however, it takes only 3 minutes to exhibit the Raman signal of DNA molecules with an intensity similar to that obtained at around 10 minutes from the static microsensor. The improvement is ~ 3 folds in detection speed, confirming the feasibility in obtaining enhanced detection speed of low-concentration molecules with motorized micro/nanosensors. The result has been observed in multiple repeats.

8.5. Conclusions

In summary, we report mechanical-rotation-enhanced capture and detection of low-concentration biomolecules. The opto-plasmonic microsensors made of diatom frustules provide silica surface chemistry for DNA capture, and periodic nanopore arrays coupled with dense plasmonic Ag hotspots for sensitive and quasi-real-time dynamic SERS

sensing. The microsensors are transported and self-assembled in individual microfluidic wells or channels that enables the desired position-deterministic sensing of DNA molecules during high-speed rotation. The mechanical rotation effectively accelerates the capture process of DNA molecules, *i.e.*, 4 times at a speed of 1200 rpm. This strategy is particularly advantageous in its low requirement of sample volume, which can rapidly accumulate interesting molecules by self-spinning induced localized flow. In comparison, for microfluidic-based passive biosensors, if enhancing by analyte flows, a large volume of samples generally should be prepared. Moreover, in this work, we understand the fundamental working mechanism of motorization-enhanced sensing by analysis, modeling and simulation. We find that to enhance the performance of such micro/nanoscale biosensors, it is critical to estimate the dimensionless Damköhler number, which represents the ratio between the reaction and transport rates of molecules. For a high-Da-number system, *e.g.* macromolecules in passive diffusion, strategies should be devoted to the enhancement of mass transportation, and the mechanical motorization is a feasible and effective approach. For a low-Da-number system, *e.g.* small molecules with convective diffusion, the detection efficiency could still benefit from mechanical locomotion due to fluidic agitation that may reduce the depletion region around a sensor when the concentration of molecular analytes is ultralow. However, in general, the improvement of reaction/adsorption kinetics could be more effective for enhancing the detection efficiency. In addition to the molecule capture and sensing system reported in this work, the theoretical modeling also helps advance our understanding of related systems that involve mechanical-motion-modulated surface adsorption and diffusion.[43] Furthermore, the method and results of modeling could be applied towards understanding molecule-nanoobject interactions often observed in micro/nanorobotic devices that operate in aqueous environments. It could assist the design and optimization of micro/nanomotors, machines, and robots for

molecular capture, sensing, and delivery, in which low-Reynolds-number hydrodynamics and reaction-diffusion kinetics play immense roles. Overall, the device design, characterization, application, as well as modeling and simulation presented in this work could inspire device schemes for high-speed biochemical enrichment, sensing, reaction, and release that are relevant to biodetection, delivery, and micro/nanorobotics.

8.6. Methods and Supporting Information

8.6.1. Fabrication of Bio-Opto-Plasmonic Microsensors:

Preparation of diatom frustules: the diatomaceous earth powders are purchased from Natural Gardener (Austin, TX) at a price of 1 dollar per pound. The diatom frustules used in this work are processed and refined *via* dispersion, sonication (2 minutes), and filtration in D.I. water. Impurities and broken pieces of frustules are filtered out by filter papers (VWR® Grade 417 Filter Paper, size of particle retention: 40 μm). The diatom frustules are then calcinated in air at 500 ˚C for 2 hours to remove organic residues.

Deposition of magnetic thin film: the magnetic thin film on diatom frustules consists of 20 nm Ni and 20 nm Au, which are deposited by electron-beam evaporation. Here the Au layer works as a passivation layer that prevents magnetic aggregation of the diatom frustules in suspension.

Synthesis of plasmonic Ag nanoparticles: Ag nanoparticles are synthesized on the surfaces of diatom frustules by catalytic reduction of silver nitrate ($AgNO_3$). Firstly, the diatom frustules are incubated and stirred in the mixture of $AgNO_3$ (0.06 M, 500 μL) and ammonia (0.12 M, 250 μL) for sufficient adsorption of Ag ions. Then polyvinylpyrrolidone (PVP, 10 mL of 2.5×10-5 M in ethanol) is added to promote the reduction of $AgNO_3$ and growth of Ag nanoparticles at 70 ˚C. After 7-hour reaction, dense Ag nanoparticles are

uniformly synthesized on the surface of diatom frustules. Finally, after rinsing in ethanol and D.I. water (repeated centrifugation and dispersion), the microsensors based on diatom frustules are stored in D.I. water.

8.6.2. Capture and Detection of DNA Molecules on Microsensors:

Materials: salmon sperm DNA used for the demonstration is purchased from Invitrogen @ Thermo Fisher Scientific (Carlsbad, CA). As stated by the manufacturer, the DNA is extracted by phenol-chloroform and sheared to an average size of < 2000 bp. The composition of binding buffer is 50 mM tris(hydroxymethyl)aminomethane (Tris), 0.25 mM acetic acid, and 400 mM potassium ions(K+), with pH adjusted to 4. Potassium hydroxide (KOH) or hydrochloric acid (HCl) is used to adjust the pH value.

DNA capture: the DNA solutions (2× predetermined concentrations) are pipetted and rapidly mixed with the binding buffers (3× predetermined concentrations) and the suspensions of microsensors with a volume ratio of 3:2:1. For the capture dynamics characterized by Surface-Enhanced-Raman Spectroscopy (SERS), the DNA concentration in the mixture is 500 μg/mL, the total volume of solution after mixing is 18 μL, and the weight percentage of microsensors in suspension is ~ 10 μg/mL. At this concentration, there are only a few microsensors in the mixed solution. In this case, the DNA concentration in the bulk solution can be considered a constant during the capture process because very low amount of DNA is captured.

For the capture dynamics characterized by Ultraviolet (UV) absorbance spectroscopy, the DNA concentration in the mixture is 500 μg/mL, the total volume of solution after mixing is 120 μL, and the weight percentage of microsensors in suspension is ~ 50 mg/mL. In this case, large amount of DNA molecules is captured so that the concentration change of DNA in the solution is detectable by the UV spectroscopy. The

DNA capture dynamics at different temperatures are conducted in refrigerator (at 5 ˚C) or in thermostatic water bath (at 25 ˚C and 45 ˚C, respectively). The DNA solutions, binding buffers and the suspensions of microsensors are all pre-cooled or pre-heated at a designated temperature for 30 minutes before mixing.

SERS characterization: In the concentration-dependent experiment as shown in Fig. 8.2A, the microsensors are incubated in DNA solutions with concentrations ranging from 80 nM to 4 μM for 2 hours before measurements. For rotation-speed-dependent experiments shown in Fig. 8.3, the DNA capture process is continuously monitored quickly after adding mixed sample solution into the testing microwell with Raman signals taken every 10 seconds for 30 minutes from a rotating sensor. A 532-nm laser with a spot of ~25 μm and power of 500 μW is used for SERS measurements. The exposure time for each test is 2 seconds. In Raman mapping, a 532-nm laser with a spot size of 1 μm and power of 100 μW is used. The exposure time for each testing point is 1 second.

Capture dynamics characterized by SERS: Diatom microsensors are immersed in 0.4 M KCl solution for half hour to remove residual PVP and for stability before use. The DNA solutions and binding buffers are pipetted and rapidly mixed with the suspension of microsensors, the concentrations of DNA molecules captured on the static or rotating microsensors are detected continuously. The laser has a spot size of ~ 25 μm so that the DNA molecules captured on the entire microsensors can be detected. The laser power is 500 μW. The exposure time for each testing point is 10 seconds.

Chapter 9: Conclusion

To develop future micro/nanorobotics, high degrees of freedom in motion is required to perform complex tasks and functions. For electrokinetic manipulations, there are several important phenomena that can generate forces and torques which are useful to drive the motion of particles in certain electric fields, i.e. dielectrophoresis, electro-alignment and electro-rotation. All of the above-mentioned phenomena are governed by the interaction between the dipole moment of the particle and the electric field. One obvious approach to change the motion of particles is to reconfigure the electric field in either strength or distribution. For instance, the light pattern projected on the photoconductive substrate will locally change the electric field distribution and realize particle trapping by dielectrophoretic forces. Meanwhile, an alternative approach would be using the light as stimuli to change the electrical properties of the particles themselves and resulting in change of mechanical motion without disturbing the external electric field.

We demonstrated a new mechanism using visible light to modulate the electrical conductivity of silicon nanowires and realized optically reconfigurable mechanical motions driven by various AC electric fields. In principle, once the silicon nanowire is placed in an AC electric field, the field will induce electrical dipole moment on the nanowire, and the dipole will further interact with the E-field, generating mechanical forces and motions accordingly. By using light to change the electrical conductivity of the nanowire, the dipole moment induced by the E-field will be modulated as well, and thus, resulting changes in mechanical behaviors. To investigate the optical effect on the electrical polarization, the optical effects on the electro-alignment and electro-rotation of silicon nanowires have been studied experimentally and theoretically. Based on the understanding of light modulation on electric polarization of semiconductor particles, we further conducted theoretical investigation on light modulation of dielectrophoresis, and proposed

a mechanism that can control the translational motion and orientation of silicon particles simultaneously. In addition to manipulating individual particles, the system with high density and strong interaction that coupling neighboring particles is also of great interest. A system consisted of spinning nanowires as the fundamental units has been studied. By introducing the dipole-dipole interaction between neighboring wires, two types of collective behaviors from silicon nanowire suspension is observed under various electric field and optical illumination conditions.

The combination of electric field and optical field has many advantages. Electric field can be generated as the driving source of the system by a relatively simple experimental setup compared with other physical fields. The field is highly tunable and versatile in terms of phase, waveform, frequency, strength etc. On the other hand, the optical field in visible wavelength can reach very high spatial resolution theoretically, which makes up for the deficiency that the local modulation of electric field is very hard. Modulating the electrical properties on particles rather than disturbing the electric field offers a new train of thought towards opto-electric manipulations, which can inspire the development of novel micro/nanorobotic devices with versatile mechanical motions and functionalities.

This working mechanism can be exploited for developing a new type of efficient visible-light-responsive micro/nanomachines without requirements of chemical fuels, UV light source, or special geometry of nanoparticle building blocks. The optically tunable polarization on silicon nanowires has been utilized to achieve reconfiguration in electromechanical motions. Based on our understanding, such an effect can be generalized to any types of materials as long as their electrical conductivities can be changed prominently when stimulated by light or any other stimuli. Various types of inorganic and organic photoconductive materials may all exhibit such an effect. Here, we demonstrated

with the most common type of semiconductor, Si. The specific performance depends on the band structure, carrier lifetime, light wavelengths and intensity, dimension of the particle, and electrical properties of the suspension medium.

Myriad demonstrations have shown the great potential of ultrasmall motors in cargo transport, single-cell drug delivery, biochemical sensing, cellular and tissue surgery, and environmental remediation. We also demonstrated rotational motion of micromotors can effectively accelerate the absorption rate and sensing speed of biomolecules. We hope this research could open up new opportunities for interdisciplinary fields, including reconfigurable optical devices, NEMS, nanorobots, nanomachines, communication, tunable molecule release, nanoparticle separation, and microfluidic automation.

Appendix A: Optical and Electrical Properties of Silicon Nanowires

Surface Depletion Effects in Silicon Nanowires

We note that the test of Si nanowires made from Si wafers with resistivity ranging from 0.6 Ω cm to over 5000 Ω cm exhibits generally similar rotation spectra with or without laser illumination. It suggests that although the doping levels of the original Si wafers are different by a few orders of magnitude, the effective electric conductivities among nanowires are much closer. Related phenomena have been observed and understood by the surface depletion effects in Si nanowires.[83,84] For as-grown Si nanowires without surface passivation, the interface between Si and the naturally oxidation layer SiO2 generate a large number of surface trapping states, which deplete carriers from the dopant and thus greatly reduce the electric conductivity. With our metal-assisted-chemical-etching fabrication process and no further passivation, the grown Si nanowires have relatively high surface state density. Taking a conservative value for surface state density of $D_{it} = 3 \times 10^{11}$ $eV^{-1}cm^{-2}$ for the nanowires, then it can be found that the complete depletion of dopant based charging carriers occurs in nanowires (500 nm in diameter) with a doping density less than 3×10^{15} cm^{-3}, or when the resistivity is greater than 1.6 Ω cm.[84] This suggests that the Si nanowires used in our experiments are mostly depleted, resulting in a much higher electric resistivity compared to the wafer, except for the nanowires made from heavily doped degenerate silicon of 0.001-0.005 Ω cm, in which no opto-mechanical effect has been observed.

Light Adsorption and Photoconductivity

Light absorption of a silicon nanowire (~5 μm in length, 500 nm in diameter and made from n-doped Si wafer of $560 - 840\ \Omega$ cm) under illumination of a 532nm laser

(127 $\mathrm{mW\,cm^{-2}}$) has been simulated by COMSOL. The finite element analysis gives results of total energy absorption cross-section (ACS) of $1.02 \times 10^{-12}\ \mathrm{m^2}$ and $9.6 \times 10^{-13}\ \mathrm{m^2}$ for TEz and TMz polarizations, respectively, shown in Fig. S1. Since the ACSs for TEz and TMz polarizations are only different within 5%, the rotation periodicity of Si nanowires due to the polarization of laser is too small to be observed compared to the opto-mechanical effect.

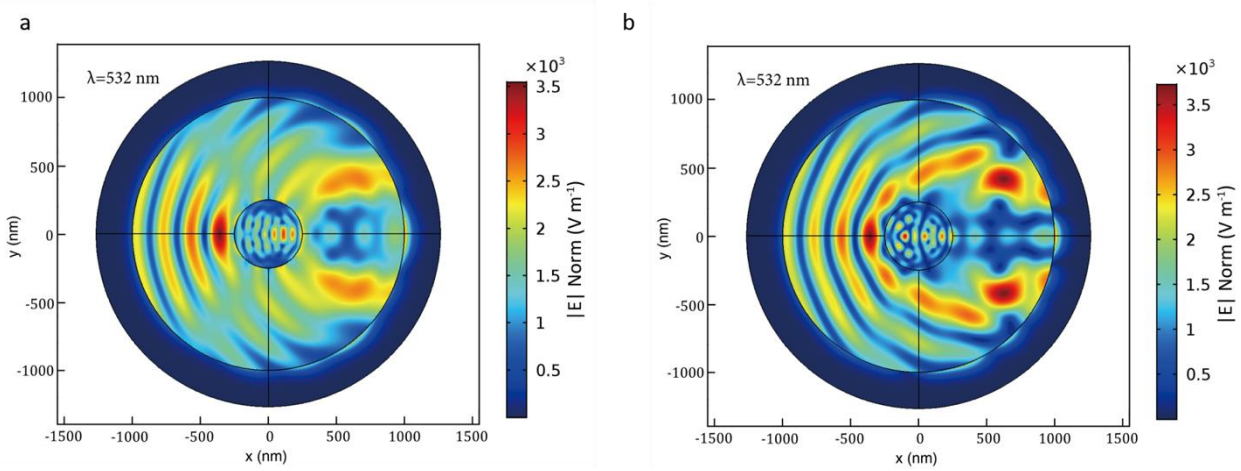

Figure S1. Light absorption of silicon nanowires. (a, b) Norm of *E*-field distribution in TEz and TMz polarizations.

For a silicon nanowire of 500 nm diameter and 10 μm length, under the illuminance of $318\ \mathrm{mW/cm^2}$ at 532 nm, the total power absorbed is equivalent to the energy of $1.7 \times 10^{10}\ \mathrm{photons\ s^{-1}}$. We adopt 50% as the quantum efficiency for a conservative magnitude estimation, as a result, the photo-excited carrier generation rate (G) is $4.3 \times 10^{21}\ \mathrm{s^{-1}\ cm^{-3}}$. When the steady state of the system is reached, there must be a balance established between the photoexcitation and recombination, which indicates the recombination rate of the nanowire must equal to the carrier generation rate (G) of

4.3×10^{21} $s^{-1}cm^{-3}$. The recombination rate of excess carriers can be expressed as $\Delta n/\tau_{eff}$, where Δn is the excess carrier density (for intrinsic silicon, $\Delta n = \Delta p$, and we need to just consider Δn for the purpose of calculation), τ_{eff} is the effective excess carrier lifetime. For steady state, $G \cdot \tau_{eff} = \Delta n$. The effective lifetime is composed of two parts, the bulk lifetime and the surface lifetime, and can be expressed as $\frac{1}{\tau_{eff}} = \frac{1}{\tau_{bulk}} + \frac{4S}{d}$, where τ_{bulk} is the bulky recombination lifetime mainly relating to Auger, Shockley-Read-Hall and radiative recombination, *S* is the surface recombination rate and *d* is the diameter of the nanowire. For nanowires, the bulk recombination is negligible, and the surface recombination dominates. After a comprehensive literature survey, we found that the surface recombination rate of silicon nanowire falls into the magnitude of 10^4 cm s^{-1} without special surface passivation,[142-145] and thus $\tau_{eff} \approx$ 5 ns for silicon nanowire of 500 nm diameter. The excess carrier density can then be calculated $\Delta n = G \cdot \tau_{\backslash eff} \approx 2.2 \times 10^{13}$ cm^{-3}. Therefore, we can calculate the photoconductivity given by $\Delta\sigma = (\mu_e + \mu_h)e\Delta n$ with a magnitude of 10^{-1} S m^{-1}.

Only the Si nanowires with the highest doping made from the n-doped 0.001-0.005 $\Omega \cdot$ cm silicon wafers are an exception. They do not show any opto-reconfiguration. It can be attributed to the ultrahigh dopant concentration of $1 \times 10^{19}\ cm^{-3}$ of the Si wafer, which corresponds to a carrier concentration of 6 orders of magnitude higher than that induced by the laser excitation ($10^{13}cm^{-3}$).

Appendix B: Characterization of the Synchronous Stepper Micromotors

Since this novel motor capable of multiple operation modes with light control could be useful for micro/nanomachinery, it is desirable to quantitatively characterize its performance by using measures such as the pullout torque-speed curve, which is often used to evaluate comparable macroscopic stepper motors. To measure this curve, we measure the phase lag θ, the angle between nanowire and electric field, by simultaneously recording the phase of the electric field at the custom function generator and the nanowire position via our computer vision tracking algorithm.

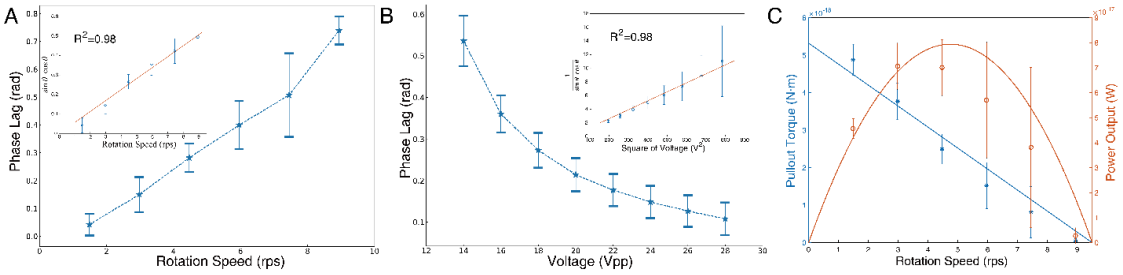

Figure S2. Analysis of dynamics of a micromotor with in-phase rotation under 318 mW/cm^2 laser illumination. (A) The phase lag θ as a function of the synchronous rotation speed ω_2. Inset: The fitting between $\sin\theta\cos\theta$ and ω_2 shows a high linear dependence with $R^2 = 0.98$. (B) The phase lag θ as a function of the driving voltage. Inset: Fit between $\frac{1}{\sin\theta\cos\theta}$ and the square of driving voltage (V^2) shows a good linear dependence with $R^2 = 0.98$. (C) Pull-out torque (in blue) and output power (in red) versus rotation speed of the micromotor at 15 V_{pp}.

When the motor operates in phase, the driving torque balances the drag torque, as previously described, due to the low Reynold number of the system. Therefore, the phase lag θ is given by:

$$\sin\theta\cos\theta = -\frac{\omega_2}{A} = -\frac{2\gamma\omega_2}{E_0^2\mathrm{Re}(\alpha_\parallel - \alpha_\perp)} \tag{B1}$$

This dependence can be verified by two experiments. Placing a nanowire in the quadruple microelectrodes, we first fix the amplitude of an applied electric field voltage at $15\,V_{pp}$ and expose the nanowire to a 532-nm laser at $318\,\mathrm{mW/cm^2}$ mW. We then measure the corresponding phase lag θ of the micromotor at different synchronous speeds ω_2 , with results shown in Figure S2A. We observe a linear dependence (inset of Figure S2A) of ω_2 on $\sin\theta\cos\theta$ with the coefficient of determination $R^2 = 0.98$ (with intercept forced at zero), confirming our understanding that the balanced driving and drag torques are proportional to the rotation speed ω_2 as in equation (S5). Second, we fix the electric field rotation speed at $\omega_2 = 1.49$ Hz, then measure the phase lag of in-phase rotation at different voltages (Figure S2B). A linear dependence of $1/V_0^2$ on $\sin\theta\cos\theta$ is obtained with $R^2 = 0.98$ (with intercept forced at zero). This result further confirms that the driving torque is proportional to the square of the electric field intensity or voltage as also shown in equation (B1).

Another two key performance characteristics of industrial synchronous motors are the pull-out torque and output power, which represent the maximum torque and power that can be extracted from the motor before it loses in-phase synchronism. For our microscale stepper motors, the pull-out torque can be calculated from a given phase lag and speed in Figure S2A as $\tau_{\mathrm{out}} = (1 - 2\sin\theta\cos\theta)\tau_{max}$. The output power at a given speed and voltage can be calculated as $P_{\mathrm{out}} = \tau_{\mathrm{out}} \cdot \omega = (1 - 2\sin\theta\cos\theta)\tau_{max}\omega$ as shown in Figure S2C. Here, we report normalized values to avoid dependence on γ, which cannot be easily calculated accurately because of a lack of good approximations for drag on nanowires rotating near a flat substrate.

Appendix C: Scale Analysis for the DNA Absorption on Micromotor Surface

SERS Signal Intensity, Surface Adsorption Density and Surface Concentration

Our previous experimental results showing the SERS signal as the characteristic variable representing the adsorption status. To be noticed, it is important to clarify which parameter the SERS signal actually reflects, the surface adsorption density *n* or the surface concentration c_s? For small analytes, the SERS signal may be dependent on both n and c_s, however, for the large analyte molecules like DNAs being used in our experiments, the SERS signal should only be proportional to n. Due to the working principle of SERS, the enhanced electric field from localized surface plasmon resonance reaches the maximum in the gap between adjacent silver nanoparticles, and decay rapidly from the particle surface. Considering the size of nanoparticles and the gap are below 10 nm, and the size of the salmon sperm DNA is about 70 nm (gyration radius), it is safe to consider that the Raman signal from DNA molecules can only be enhanced by the plasmonic surface when the molecules are extremely close to the surface, in other words, be in the absorbed states. Thus, it is the surface density *n* that is proportional to the SERS signal being detected.

When the system reaches an equilibrium, the surface concentration c_s is equal to c_0, and the surface density in equilibrium is given by $n_{eq} = \frac{k_a n_{max} c_0}{k_a c_0 + k_d}$. Let $\tilde{c} = \frac{k_a c_0}{k_d}$, n_{eq} can then be written as $n_{eq} = \frac{\tilde{c}}{1+\tilde{c}} n_{max}$. For sensing and detection of diluted analytes that satisfy $n_{eq} \ll n_{max}$, $\tilde{c} \ll 1$. We notice for $\tilde{c} \ll 1$, $n_{eq} \approx n_{max}\tilde{c} = n_{max}\frac{k_a}{k_d}c_0$, a linear dependence should exist between the bulky concentration of solution and the final surface adsorption density, as well as the SERS signal intensity at equilibrium.

Scaling Analysis

To grasp a more quantitative understanding and the scaling of the equations, we non-dimensionalize the equations (2-3) as follows:

$$\frac{\partial C}{\partial T_D} = \frac{\partial^2 C}{\partial X^2} \tag{C1}$$

$$C = 1 \quad at\ X = 1 \tag{C2}$$

$$\frac{\partial \mathrm{N}}{\partial \mathrm{T_{RD}}} - Da\frac{\partial C}{\partial X} = 0 \tag{C3}$$

$$\frac{\partial N}{\partial T_R} = C_s - \frac{1}{1+\tilde{c}}N \approx C_s - N \tag{C4}$$

where $\mathrm{C} = \frac{\mathrm{c}}{\mathrm{c_0}}, X = \frac{x}{\delta_D}, T_D = \frac{t}{\tau_D}, N = \frac{n}{n_{eq}}$, $\mathrm{T_{RD}} = \frac{t}{\tau_{RD}}, T_R = \frac{t}{\tau_R}$, with $\tau_\mathrm{D} = \frac{\delta_D^2}{D}$, $\tau_{RD} = \frac{k_a n_{max}\delta_D}{k_d(1+\tilde{c})D}$, $\tau_R = \frac{1}{k_d(1+\tilde{c})}$, and the dimensionless number $Da = \frac{\delta_D n_{max} k_a}{D}$ is referred as Damkohler number, which represents the ratio between reaction rate to diffusion rate. By tuning the δ_D, we investigate systems with Damkohler numbers ranging from $0.001\ to\ 1000$. When $Da \ll 1$, the kinetic rate is limited by the surface adsorption reaction. On the other hand, for $Da \gg 1$, the kinetic rate is limited by the diffusion process.

Numerical implementation of FDTD with the Crank Nicolson method

J. Crank and P. Nicolson introduced the method in 1947, which is based on evaluating the space derivative from central approximation at the additional time step at point $(x_i, t_j + \frac{1}{2}\Delta t)$ as follows:

$$\frac{u_i^{j+1} - u_i^j}{2\frac{\Delta t}{2}} = D\frac{u_{i+1}^{j+\frac{1}{2}} - 2u_i^{j+\frac{1}{2}} + u_{i-1}^{j+\frac{1}{2}}}{\Delta x^2} = D\frac{(u_{i+1}^j - 2u_i^j + u_{i-1}^j) + (u_{i+1}^{j+1} - 2u_i^{j+1} + u_{i-1}^{j+1})}{2\Delta x^2} \tag{C5}$$

Let $\lambda = \frac{D\Delta t}{\Delta x^2}$, we can rewrite the equation (C5) as follows:

$$-\lambda u_{i+1}^{j+1} + 2(1+\lambda)u_i^{j+1} - \lambda u_{i-1}^{j+1} = \lambda u_{i+1}^{j} + 2(1-\lambda)u_i^{j} + \lambda u_{i-1}^{j} \qquad \text{(C6)}$$

For example, if we partition the 1-D space by 6 nodes (nx=6), as $i = 1, 2, 3, 4, 5, 6$, the boundary conditions are located at $\mathrm{i} = 1$ and $\mathrm{i} = 6$, the interior nodes to be solved are $i = 2, 3, 4, 5$.

For all interior nodes, let, $U^j = \begin{bmatrix} u_2^j \\ u_3^j \\ u_4^j \\ u_5^j \end{bmatrix}$, we want to rewrite equation (C6) into a matrix formulation as:

$$AU = B$$

To define each element in A and B, we take a closer look at each space nodes at j=2 for example. For i=5, j=2

$$-\lambda u_6^2 + 2(1+\lambda)u_5^2 - \lambda u_4^2 = \lambda u_6^1 + 2(1-\lambda)u_5^1 + \lambda u_4^1$$

Notice that u_6^2 is governed by boundary condition $u_6 = c_0$ at the outer wall of the diffusion boundary layer, we get:

$$2(1+\lambda)u_5^2 - \lambda u_4^2 = \lambda u_6^1 + 2(1-\lambda)u_5^1 + \lambda u_4^1 + -\lambda c_0$$

For $j = 1$, initial value defines u_i^1, thus, all the terms on the right side of the above equation are known and can be calculated as

$$b_5 = \lambda u_6^1 + 2(1-\lambda)u_5^1 + \lambda u_4^1 + -\lambda c_0$$

For $i = 4, j = 2$

$$-\lambda u_5^2 + 2(1+\lambda)u_4^2 - \lambda u_3^2 = \lambda u_5^1 + 2(1-\lambda)u_4^1 + \lambda u_3^1$$

Similarly, u_i^1 are defined by initial value, and all terms on the right side can be calculated as:

$$b_4 = \lambda u_5^1 + 2(1-\lambda)u_4^1 + \lambda u_3^1$$

For i>2 and i< nx-2, the general formulation can be written as:

$$-\lambda u_{i+1}^{j+1} + 2(1+\lambda)u_i^{j+1} - \lambda u_{i-1}^{j+1} = b_i$$

with $b_i = \lambda u_{i+1}^{j} + 2(1-\lambda)u_i^{j} + \lambda u_{i-1}^{j}$

For *i*= 2, another boundary condition at *x*= 0 gets involved with the surface reaction, and need additional modification from the general form.

The boundary condition at x=0 comes from the conservation of mass, where the diffusion flux into the surface equals to the amount of surface adsorption per unit time unit area as shown by:

$$\frac{\partial n}{\partial t} - D\frac{\partial u}{\partial x} = 0 \qquad \text{at } x = 0 \tag{C7}$$

In order to derive the formulation for u_2^2, we first need to know the value of u_1^2 from the boundary condition and surface reaction. First, the solution of surface adsorption density *n* can be written as:

$$\frac{\partial n}{\partial t} = \frac{n_2 - n_1}{\Delta t} = D\,\frac{u_2^1 - u_1^1}{\Delta x}$$

$$\mathrm{n}_2 = \mathrm{n}_1 + D\,\frac{u_2^1 - u_1^1}{\Delta x}\Delta t$$

Note that the subscript of *n* refers the time step. As n_2 is known, we can then substitute n_2 into the surface reaction equation to get the surface concentration at second time step u_1^2:

$$\frac{\partial \mathrm{n}}{\partial t} = D\,\frac{u_2^2 - u_1^2}{\Delta x} = \mathrm{k_a} u_1^2 n_{max} - k_d n_2$$

and u_1^2 can be calculated as:

$$u_1^2 = \frac{D\,\frac{u_2^2 - u_1^2}{\Delta x} + k_d \mathrm{n}_2}{k_a n_{max}} = \frac{\frac{D u_2^2}{\Delta x} + k_d n_2}{k_a n_{max} + D/\Delta x}$$

Substitute the above expression of u_1^2 into the general formulation (C6):

$$-\lambda u_3^2 + 2(1+\lambda)u_2^2 - \lambda u_1^2 = \lambda u_3^1 + 2(1-\lambda)u_2^1 + \lambda u_1^1$$

Moving all known terms to the right side and merge unknown terms, we can get:

$$-\lambda u_3^2 + [2(1+\lambda) - \frac{\lambda D}{\Delta x(k_a n_{max} + \frac{D}{\Delta x})}]u_2^2 = \lambda u_3^1 + 2(1-\lambda)u_2^1 + \lambda u_1^1 + \frac{\lambda k_d n_2}{k_a n_{max} + D/\Delta x},$$

And thus, $b_2 = \lambda u_3^1 + 2(1-\lambda)u_2^1 + \lambda u_1^1 + \frac{\lambda k_d n_2}{k_a n_{max} + D/\Delta x}$.

Now we can write each element in the matrix formulation AU=B as:

$$A = \begin{bmatrix} [2(1+\lambda) - \frac{\lambda D}{\Delta x(k_a n_{max} + \frac{D}{\Delta x})}] & -\lambda & 0 & 0 \\ -\lambda & 2(1+\lambda) & -\lambda & 0 \\ 0 & -\lambda & 2(1+\lambda) & -\lambda \\ 0 & 0 & -\lambda & 2(1+\lambda) \end{bmatrix}$$

$$U = \begin{bmatrix} u_2^2 \\ u_3^2 \\ u_4^2 \\ u_5^2 \end{bmatrix}$$

$$B = \begin{bmatrix} b_2 \\ b_3 \\ b_4 \\ b_5 \end{bmatrix} = \begin{bmatrix} \lambda u_3^1 + 2(1-\lambda)u_2^1 + \lambda u_1^1 + \frac{\lambda k_d n_2}{k_a n_{max} + D/\Delta x} \\ \lambda u_4^1 + 2(1-\lambda)u_3^1 + \lambda u_2^1 \\ \lambda u_5^1 + 2(1-\lambda)u_4^1 + \lambda u_3^1 \\ \lambda u_6^1 + 2(1-\lambda)u_5^1 + \lambda u_4^1 + -\lambda c_0 \end{bmatrix}$$

By iteratively solving AU=B, we can get the numerical solution in time domain of the reaction-diffusion system.

In the numerical simulation, we generate 101 space nodes between the surface of silica to the outer edge of the diffusion layer. The time increment and number of steps are adaptively selected in order to achieve high accuracy with reasonable computational costs. The initial condition is set as $n_1 = 0, u_i^1 = 0 \; for \; i = 1, 2, \ldots, 100, and \; u_{100} = c_0$.

References

1 Kolomeisky, A. B. Motor proteins and molecular motors: how to operate machines at the nanoscale. *Journal of Physics: Condensed Matter* **25**, 463101 (2013).

2 Howard, J. The movement of kinesin along microtubules. *Annual review of physiology* **58**, 703-729 (1996).

3 Oster, G. & Wang, H. Rotary protein motors. *Trends in cell biology* **13**, 114-121 (2003).

4 Berg, H. C. The rotary motor of bacterial flagella. *Annual review of biochemistry* **72** (2003).

5 Hirokawa, N., Noda, Y., Tanaka, Y. & Niwa, S. Kinesin superfamily motor proteins and intracellular transport. *Nature reviews Molecular cell biology* **10**, 682-696 (2009).

6 Coy, D. L., Wagenbach, M. & Howard, J. Kinesin takes one 8-nm step for each ATP that it hydrolyzes. *Journal of Biological Chemistry* **274**, 3667-3671 (1999).

7 Yildiz, A., Tomishige, M., Vale, R. D. & Selvin, P. R. Kinesin walks hand-over-hand. *Science* **303**, 676-678 (2004).

8 Svoboda, K., Schmidt, C. F., Schnapp, B. J. & Block, S. M. Direct observation of kinesin stepping by optical trapping interferometry. *Nature* **365**, 721-727 (1993).

9 Carter, N. J. & Cross, R. Mechanics of the kinesin step. *Nature* **435**, 308-312 (2005).

10 Magariyama, Y. *et al.* Very fast flagellar rotation. *Nature* **371**, 752-752 (1994).

11 Meister, M., Lowe, G. & Berg, H. C. The proton flux through the bacterial flagellar motor. *Cell* **49**, 643-650 (1987).

12 Kassem, S. *et al.* Artificial molecular motors. *Chemical Society Reviews* **46**, 2592-2621 (2017).

13 Erbas-Cakmak, S., Leigh, D. A., McTernan, C. T. & Nussbaumer, A. L. Artificial molecular machines. *Chemical Reviews* **115**, 10081-10206 (2015).

14 Kinbara, K. & Aida, T. Toward intelligent molecular machines: directed motions of biological and artificial molecules and assemblies. *Chemical reviews* **105**, 1377-1400 (2005).

15 Bruns, C. J. & Stoddart, J. F. *The nature of the mechanical bond: from molecules to machines*. (John Wiley & Sons, 2016).

16 Anelli, P. L., Spencer, N. & Stoddart, J. F. A molecular shuttle. *Journal of the American Chemical Society* **113**, 5131-5133 (1991).

17 Bissell, R. A., Córdova, E., Kaifer, A. E. & Stoddart, J. F. A chemically and electrochemically switchable molecular shuttle. *Nature* **369**, 133-137 (1994).

18 Koumura, N., Zijlstra, R. W., van Delden, R. A., Harada, N. & Feringa, B. L. Light-driven monodirectional molecular rotor. *Nature* **401**, 152-155 (1999).

19 Conyard, J., Cnossen, A., Browne, W. R., Feringa, B. L. & Meech, S. R. Chemically optimizing operational efficiency of molecular rotary motors. *Journal of the American Chemical Society* **136**, 9692-9700 (2014).

20 Adler, J. Chemotaxis in bacteria. *Annual review of biochemistry* **44**, 341-356 (1975).

21 Adler, J. Chemotaxis in bacteria. *Science* **153**, 708-716 (1966).

22 Childress, S. *Mechanics of swimming and flying*. Vol. 2 (Cambridge University Press, 1981).

23 Purcell, E. M. The efficiency of propulsion by a rotating flagellum. *Proceedings of the National Academy of Sciences* **94**, 11307-11311 (1997).

24 Chattopadhyay, S., Moldovan, R., Yeung, C. & Wu, X. Swimming efficiency of bacterium Escherichiacoli. *Proceedings of the National Academy of Sciences* **103**, 13712-13717 (2006).

25 Ghosh, A. & Fischer, P. Controlled propulsion of artificial magnetic nanostructured propellers. *Nano letters* **9**, 2243-2245 (2009).

26 Zhang, L. *et al.* Artificial bacterial flagella: Fabrication and magnetic control. *Applied Physics Letters* **94**, 064107 (2009).

27 Gibbs, J. & Fischer, P. Active colloidal microdrills. *Chem Commun* **51**, 4192-4195 (2015).

28 Bray, D. *Cell movements: from molecules to motility*. (Garland Science, 2000).

29 Gillies, E. A., Cannon, R. M., Green, R. B. & Pacey, A. A. Hydrodynamic propulsion of human sperm. *Journal of Fluid Mechanics* **625**, 445-474 (2009).

30 Brennen, C. & Winet, H. Fluid mechanics of propulsion by cilia and flagella. *Annual Review of Fluid Mechanics* **9**, 339-398 (1977).

31 Lowe, C. P. Dynamics of filaments: modelling the dynamics of driven microfilaments. *Philosophical Transactions of the Royal Society of London. Series B: Biological Sciences* **358**, 1543-1550 (2003).

32 Wiggins, C. H. & Goldstein, R. E. Flexive and propulsive dynamics of elastica at low Reynolds number. *Physical Review Letters* **80**, 3879 (1998).

33 Dreyfus, R. *et al.* Microscopic artificial swimmers. *Nature* **437**, 862 (2005).

34 Purcell, E. M. Life at low Reynolds number. *Am. J. Phys.* **45**, 3-11 (1977).

35 Wang, W., Duan, W., Ahmed, S., Mallouk, T. E. & Sen, A. Small power: Autonomous nano-and micromotors propelled by self-generated gradients. *Nano Today* **8**, 531-554 (2013).

36 Ma, X., Hortelão, A. C., Patiño, T. & Sánchez, S. Enzyme catalysis to power micro/nanomachines. *ACS nano* **10**, 9111-9122 (2016).

37 Paxton, W. F. *et al*. Catalytic nanomotors: autonomous movement of striped nanorods. *Journal of the American Chemical Society* **126**, 13424-13431 (2004).

38 Fournier-Bidoz, S., Arsenault, A. C., Manners, I. & Ozin, G. A. Synthetic self-propelled nanorotors. *Chem Commun*, 441-443 (2005).

39 Wang, W., Chiang, T.-Y., Velegol, D. & Mallouk, T. E. Understanding the efficiency of autonomous nano-and microscale motors. *Journal of the American Chemical Society* **135**, 10557-10565 (2013).

40 Anderson, J. L. & Prieve, D. C. Diffusiophoresis: migration of colloidal particles in gradients of solute concentration. *Separation and Purification Methods* **13**, 67-103 (1984).

41 Anderson, J. L. Colloid transport by interfacial forces. *Annual review of fluid mechanics* **21**, 61-99 (1989).

42 Hong, Y., Diaz, M., Córdova‐Figueroa, U. M. & Sen, A. Light‐driven titanium‐dioxide‐based reversible microfireworks and micromotor/micropump systems. *Advanced Functional Materials* **20**, 1568-1576 (2010).

43 Zhou, C., Zhang, H., Tang, J. & Wang, W. Photochemically powered AgCl Janus micromotors as a model system to understand ionic self-diffusiophoresis. *Langmuir* **34**, 3289-3295 (2018).

44 Pavlick, R. A., Sengupta, S., McFadden, T., Zhang, H. & Sen, A. A polymerization ‐ powered motor. *Angewandte Chemie International Edition* **50**, 9374-9377 (2011).

45 Xuan, M. *et al.* Near infrared light-powered Janus mesoporous silica nanoparticle motors. *Journal of the American Chemical Society* **138**, 6492-6497 (2016).

46 Jiang, H.-R., Yoshinaga, N. & Sano, M. Active motion of a Janus particle by self-thermophoresis in a defocused laser beam. *Physical review letters* **105**, 268302 (2010).

47 Li, J., Rozen, I. & Wang, J. Rocket science at the nanoscale. *ACS nano* **10**, 5619-5634 (2016).

48 Mei, Y. *et al.* Versatile approach for integrative and functionalized tubes by strain engineering of nanomembranes on polymers. *Advanced Materials* **20**, 4085-4090 (2008).

49 Wang, L.-l. *et al.* Efficient propulsion and hovering of bubble-driven hollow micromotors underneath an air–liquid interface. *Langmuir* **34**, 10426-10433 (2018).

50 Tierno, P., Golestanian, R., Pagonabarraga, I. & Sagués, F. Controlled swimming in confined fluids of magnetically actuated colloidal rotors. *Physical review letters* **101**, 218304 (2008).

51 Sing, C. E., Schmid, L., Schneider, M. F., Franke, T. & Alexander-Katz, A. Controlled surface-induced flows from the motion of self-assembled colloidal walkers. *Proceedings of the National Academy of Sciences* **107**, 535-540 (2010).

52 Zhang, L. *et al.* Controlled Propulsion and Cargo Transport of Rotating Nickel Nanowires near a Patterned Solid Surface. *Acs Nano* **4**, 6228-6234, doi:10.1021/nn101861n (2010).

53 Palagi, S. *et al.* Structured light enables biomimetic swimming and versatile locomotion of photoresponsive soft microrobots. *Nature materials* **15**, 647-653 (2016).

54 Qiu, T. *et al.* Swimming by reciprocal motion at low Reynolds number. *Nature communications* **5**, 1-8 (2014).

55 Neuman, K. C. & Block, S. M. Optical trapping. *Review of scientific instruments* **75**, 2787-2809 (2004).

56 Fan, D., Cammarata, R. & Chien, C. Precision transport and assembling of nanowires in suspension by electric fields. *Applied Physics Letters* **92**, 093115 (2008).

57 De Vlaminck, I. & Dekker, C. Recent advances in magnetic tweezers. *Annual review of biophysics* **41**, 453-472 (2012).

58 Ozcelik, A. *et al.* Acoustic tweezers for the life sciences. *Nature methods* **15**, 1021-1028 (2018).

59 Curtis, J. E., Koss, B. A. & Grier, D. G. Dynamic holographic optical tweezers. *Opt. Commun.* **207**, 169-175 (2002).

60 Chiou, P. Y., Ohta, A. T. & Wu, M. C. Massively parallel manipulation of single cells and microparticles using optical images. *Nature* **436**, 370-372 (2005).

61 Jones, T. B. & Jones, T. B. *Electromechanics of particles*. (Cambridge University Press, 2005).

62 Guo, F. *et al.* Three-dimensional manipulation of single cells using surface acoustic waves. *Proceedings of the National Academy of Sciences* **113**, 1522-1527 (2016).

63 Marzo, A. *et al.* Holographic acoustic elements for manipulation of levitated objects. *Nature communications* **6**, 8661 (2015).

64 Melde, K., Mark, A. G., Qiu, T. & Fischer, P. Holograms for acoustics. *Nature* **537**, 518-522, doi:10.1038/nature19755 (2016).

65 Liang, Z. & Fan, D. Visible light–gated reconfigurable rotary actuation of electric nanomotors. *Science advances* **4**, eaau0981 (2018).

66 Liang, Z., Teal, D. & Fan, D. E. Light programmable micro/nanomotors with optically tunable in-phase electric polarization. *Nature communications* **10**, 1-10 (2019).

67 Magdanz, V., Sanchez, S. & Schmidt, O. G. Development of a sperm‐flagella driven micro‐bio‐robot. *Advanced Materials* **25**, 6581-6588 (2013).

68 Chen, C. *et al.* Chemical/Light‐Powered Hybrid Micromotors with "On‐the‐Fly" Optical Brakes. *Angewandte Chemie* **130**, 8242-8246 (2018).

69 Guo, J., Gallegos, J. J., Tom, A. R. & Fan, D. Electric-field-guided precision manipulation of catalytic nanomotors for cargo delivery and powering nanoelectromechanical devices. *ACS nano* **12**, 1179-1187 (2018).

70 Masliyah, J. H. & Bhattacharjee, S. *Electrokinetic and colloid transport phenomena*. (John Wiley & Sons, 2006).

71 Jackson, J. D. *Classical electrodynamics*. (John Wiley & Sons, 2007).

72 Bazant, M. Z. & Squires, T. M. Induced-charge electrokinetic phenomena: theory and microfluidic applications. *Phys. Rev. Lett.* **92**, 066101 (2004).

73 García-Sánchez, P., Flores-Mena, J. E. & Ramos, A. Modeling the AC electrokinetic behavior of semiconducting spheres. *Micromachines* **10**, 100 (2019).

74 Miloh, T. Nonlinear alternating electric field dipolophoresis of spherical nanoparticles. *Phys. Fluids* **21**, 072002 (2009).

75 Flores-Mena, J., García-Sánchez, P. & Ramos, A. Electrokinetics of metal cylinders. *Physical Review E* **99**, 032603 (2019).

76 Rodríguez-Sánchez, L., Ramos, A. & García-Sánchez, P. Electrorotation of semiconducting microspheres. *Physical Review E* **100**, 042616 (2019).

77 Huang, Z., Fang, H. & Zhu, J. Fabrication of silicon nanowire arrays with controlled diameter, length, and density. *Adv. Mater.* **19**, 744-748 (2007).

78 Peng, K. Q., Yan, Y. J., Gao, S. P. & Zhu, J. Synthesis of Large‐Area Silicon Nanowire Arrays via Self‐Assembling Nanoelectrochemistry. *Adv. Mater.* **14**, 1164-1167 (2002).

79 Xu, X., Liu, C., Kim, K. & Fan, D. L. Electric-Driven Rotation of Silicon Nanowires and Silicon Nanowire Motors. *Adv. Funct. Mater.* **24**, 4843-4850, doi:10.1002/adfm.201303505 (2014).

80 Broersma, S. Rotational diffusion constant of a cylindrical particle. *The Journal of Chemical Physics* **32**, 1626-1631 (1960).

81 Zhang, A., Kim, H., Cheng, J. & Lo, Y.-H. Ultrahigh responsivity visible and infrared detection using silicon nanowire phototransistors. *Nano Lett.* **10**, 2117-2120 (2010).

82 Tan, S. L., Zhao, X., Chen, K., Crozier, K. B. & Dan, Y. High-performance silicon nanowire bipolar phototransistors. *Applied Physics Letters* **109**, 033505 (2016).

83 Simpkins, B., Mastro, M., Eddy Jr, C. & Pehrsson, P. Surface depletion effects in semiconducting nanowires. *J. Appl. Phys.* **103**, 104313 (2008).

84 Schmidt, V., Senz, S. & Gösele, U. Influence of the Si/SiO2 interface on the charge carrier density of Si nanowires. *Appl. Phys. A* **86**, 187-191 (2007).

85 Grumstrup, E. M. *et al.* Ultrafast Carrier Dynamics in Individual Silicon Nanowires: Characterization of Diameter-Dependent Carrier Lifetime and Surface Recombination with Pump–Probe Microscopy. *The Journal of Physical Chemistry C* **118**, 8634-8640, doi:10.1021/jp502737e (2014).

86 Dan, Y. *et al.* Dramatic reduction of surface recombination by in situ surface passivation of silicon nanowires. *Nano Lett.* **11**, 2527-2532, doi:10.1021/nl201179n (2011).

87 Demichel, O. *et al.* Surface recombination velocity measurements of efficiently passivated gold-catalyzed silicon nanowires by a new optical method. *Nano Lett.* **10**, 2323-2329, doi:10.1021/nl903166t (2010).

88 Kim, K., Guo, J., Xu, X. & Fan, D. Micromotors with step-motor characteristics by controlled magnetic interactions among assembled components. *ACS nano* **9**, 548-554 (2014).

89 Edwards, B., Mayer, T. S. & Bhiladvala, R. B. Synchronous electrorotation of nanowires in fluid. *Nano Lett.* **6**, 626-632 (2006).

90 Yang, F. Y. *et al.* Large Magnetoresistance of Electrodeposited Single-Crystal Bismuth Thin Films. *Science* **284**, 1335-1337, doi:10.1126/science.284.5418.1335 (1999).

91 Bechinger, C. *et al.* Active particles in complex and crowded environments. *Rev. Mod. Phys.* **88**, 045006 (2016).

92 Wu, Z. *et al.* A swarm of slippery micropropellers penetrates the vitreous body of the eye. *Science advances* **4**, eaat4388 (2018).

93 Palagi, S. *et al.* Structured light enables biomimetic swimming and versatile locomotion of photoresponsive soft microrobots. *Nature materials* **15**, 647 (2016).

94 Huang, Y., Liang, Z., Alsoraya, M., Guo, J. & Fan, D. Light‐Gated Manipulation of Micro/Nanoparticles in Electric Fields. *Advanced Intelligent Systems* **2**, 1900127 (2020).

95 Zhou, H., Preston, M. A., Tilton, R. D. & White, L. R. Calculation of the electric polarizability of a charged spherical dielectric particle by the theory of colloidal electrokinetics. *J. Colloid Interface Sci.* **285**, 845-856 (2005).

96 Cao, W., Chern, M., Dennis, A. M. & Brown, K. A. Measuring nanoparticle polarizability using fluorescence microscopy. *Nano Lett.* **19**, 5762-5768 (2019).

97 Vicsek, T. & Zafeiris, A. Collective motion. *Physics reports* **517**, 71-140 (2012).

98 Douglas, S. M. *et al.* Self-assembly of DNA into nanoscale three-dimensional shapes. *Nature* **459**, 414-418 (2009).

99 Mogili, U. R. & Deepak, B. Review on application of drone systems in precision agriculture. *Procedia computer science* **133**, 502-509 (2018).

100 Velev, O. D. & Bhatt, K. H. On-chip micromanipulation and assembly of colloidal particles by electric fields. *Soft Matter* **2**, 738-750 (2006).

101 Singh, J. P., Lele, P. P., Nettesheim, F., Wagner, N. J. & Furst, E. M. One- and two-dimensional assembly of colloidal ellipsoids in ac electric fields. *Physical Review E* **79**, 050401 (2009).

102 Yu, J., Wang, B., Du, X., Wang, Q. & Zhang, L. Ultra-extensible ribbon-like magnetic microswarm. *Nature communications* **9**, 1-9 (2018).

103 Leunissen, M. E., Vutukuri, H. R. & van Blaaderen, A. Directing Colloidal Self‐Assembly with Biaxial Electric Fields. *Adv. Mater.* **21**, 3116-3120 (2009).

104 Muller, K. *et al.* Pattern formation and coarse-graining in two-dimensional colloids driven by multiaxial magnetic fields. *Langmuir* **30**, 5088-5096 (2014).

105 Osterman, N. *et al.* Field-induced self-assembly of suspended colloidal membranes. *Phys. Rev. Lett.* **103**, 228301 (2009).

106 Yan, J., Bloom, M., Bae, S. C., Luijten, E. & Granick, S. Linking synchronization to self-assembly using magnetic Janus colloids. *Nature* **491**, 578-581 (2012).

107 Grzybowski, B. A., Stone, H. A. & Whitesides, G. M. Dynamic self-assembly of magnetized, millimetre-sized objects rotating at a liquid–air interface. *Nature* **405**, 1033-1036 (2000).

108 Deseigne, J., Dauchot, O. & Chaté, H. Collective motion of vibrated polar disks. *Phys. Rev. Lett.* **105**, 098001 (2010).

109 Aubret, A., Youssef, M., Sacanna, S. & Palacci, J. Targeted assembly and synchronization of self-spinning microgears. *Nature Physics* **14**, 1114-1118 (2018).

110 Ibele, M., Mallouk, T. E. & Sen, A. Schooling behavior of light‐powered autonomous micromotors in water. *Angew. Chem.* **121**, 3358-3362 (2009).

111 Kudrolli, A., Lumay, G., Volfson, D. & Tsimring, L. S. Swarming and swirling in self-propelled polar granular rods. *Phys. Rev. Lett.* **100**, 058001 (2008).

112 Bricard, A., Caussin, J.-B., Desreumaux, N., Dauchot, O. & Bartolo, D. Emergence of macroscopic directed motion in populations of motile colloids. *Nature* **503**, 95-98 (2013).

113 Kokot, G. & Snezhko, A. Manipulation of emergent vortices in swarms of magnetic rollers. *Nature communications* **9**, 1-7 (2018).

114 Liang, Z. & Fan, D. Visible light–gated reconfigurable rotary actuation of electric nanomotors. *Science advances* **4**, eaau0981 %@ 2375-2548 (2018).

115 Kim, K., Lang, Z. X., Liu, M. L. & Fan, D. L. Biobased High-Performance Rotary Micromotors for Individually Reconfigurable Micromachine Arrays and Microfluidic Applications. *Acs Applied Materials & Interfaces* **9**, 6144-6152, doi:10.1021/acsami.6b13997 (2017).

116 Clayton, J. *et al.* Electroluminescence and Photoluminescence from Nanostructured Diatom Frustules Containing Metabolically Inserted Germanium. *Adv. Mater.* **20**, 2633-2637, doi:doi:10.1002/adma.200800292 (2008).

117 Ren, F., Campbell, J., Wang, X., Rorrer, G. L. & Wang, A. X. Enhancing surface plasmon resonances of metallic nanoparticles by diatom biosilica. *Opt. Express* **21**, 15308-15313, doi:10.1364/OE.21.015308 (2013).

118 Liu, C. *et al.* Electrokinetic manipulation integrated plasmonic–photonic hybrid raman nanosensors with dually enhanced sensitivity. *Acs Sensors* **2**, 346-353 (2017).

119 Ghobara, M. *et al.* On light and diatoms: A photonics and photobiology review. *Diatoms: Fundamentals and Applications*, 129 (2019).

120 Rea, I. & De Stefano, L. Recent advances on diatom-based biosensors. *Sensors* **19**, 5208 (2019).

121 Leonardo, S., Prieto-Simón, B. & Campàs, M. Past, present and future of diatoms in biosensing. *TrAC, Trends Anal. Chem.* **79**, 276-285 (2016).

122 Xu, X. B., Kim, K., Li, H. F. & Fan, D. L. Ordered Arrays of Raman Nanosensors for Ultrasensitive and Location Predictable Biochemical Detection. *Adv. Mater.* **24**, 5457-5463, doi:10.1002/adma.201201820 (2012).

123 Xu, X. B., Kim, K. & Fan, D. L. Tunable Release of Multiplex Biochemicals by Plasmonically Active Rotary Nanomotors. *Angew. Chem. Int. Ed.* **54**, 2525-2529, doi:10.1002/anie.201410754 (2015).

124 Kutzler, M. A. & Weiner, D. B. DNA vaccines: ready for prime time? *Nat. Rev. Genet.* **9**, 776-788, doi:10.1038/nrg2432 (2008).

125 Jobling, M. A. & Gill, P. Encoded evidence: DNA in forensic analysis. *Nat. Rev. Genet.* **5**, 739-751, doi:10.1038/nrg1455 (2004).

126 Lee, G. J., Kwon, Y.-W., Kim, Y. H. & Choi, E. H. Raman spectroscopic study of plasma-treated salmon DNA. *Appl. Phys. Lett.* **102**, 021911, doi:10.1063/1.4776673 (2013).

127 Liu, J., Guo, J., Meng, G. & Fan, D. Superstructural Raman Nanosensors with Integrated Dual Functions for Ultrasensitive Detection and Tunable Release of Molecules. *Chem. Mater.* **30**, 5256-5263, doi:10.1021/acs.chemmater.8b01979 (2018).

128 Xu, L.-J. *et al.* Label-Free Surface-Enhanced Raman Spectroscopy Detection of DNA with Single-Base Sensitivity. *J. Am. Chem. Soc.* **137**, 5149-5154, doi:10.1021/jacs.5b01426 (2015).

129 Smeets, R. M. M. *et al.* Salt Dependence of Ion Transport and DNA Translocation through Solid-State Nanopores. *Nano Lett.* **6**, 89-95, doi:10.1021/nl052107w (2006).

130 Vandeventer, P. E. *et al.* Multiphasic DNA Adsorption to Silica Surfaces under Varying Buffer, pH, and Ionic Strength Conditions. *J. Phys. Chem. B* **116**, 5661-5670, doi:10.1021/jp3017776 (2012).

131 Huang, F. J. & Liang, H. J. Adsorption Behaviors of DNA/Cation Complexes on Amino and Silica Chip Surfaces: A Dual Polarization Interferometry Study. *ACS Appl. Mater. Interfaces* **5**, 5025-5033, doi:10.1021/am400813x (2013).

132 Ulrike, L., Caroline, V., K., P. V. & M., G. M. A. Droplet‐Based DNA Purification in a Magnetic Lab on a Chip. *Angew. Chem. Int. Ed.* **45**, 3062-3067, doi:doi:10.1002/anie.200503624 (2006).

133 Zhang, Y. *et al.* A Simple Thermoplastic Substrate Containing Hierarchical Silica Lamellae for High-Molecular-Weight DNA Extraction. *Adv. Mater.* **28**, 10630-10636, doi:10.1002/adma.201603738 (2016).

134 Johnson, P. A., Gaspar, M. A. & Levicky, R. Polymer-anchored DNA gene monolayers. *Journal of the American Chemical Society* **126**, 9910-9911, doi:10.1021/ja048415y (2004).

135 Katevatis, C., Fan, A. & Klapperich, C. M. Low concentration DNA extraction and recovery using a silica solid phase. *PLOS ONE* **12**, e0176848, doi:10.1371/journal.pone.0176848 (2017).

136 Li, X., Zhang, J. & Gu, H. Adsorption and Desorption Behaviors of DNA with Magnetic Mesoporous Silica Nanoparticles. *Langmuir* **27**, 6099-6106, doi:10.1021/la104653s (2011).

137 Vandeventer, P. E., Mejia, J., Nadim, A., Johal, M. S. & Niemz, A. DNA Adsorption to and Elution from Silica Surfaces: Influence of Amino Acid Buffers. *J. Phys. Chem. B* **117**, 10742-10749, doi:10.1021/jp405753m (2013).

138 Sheehan, P. E. & Whitman, L. J. Detection limits for nanoscale biosensors. *Nano Lett.* **5**, 803-807 (2005).

139 Squires, T. M., Messinger, R. J. & Manalis, S. R. Making it stick: convection, reaction and diffusion in surface-based biosensors. *Nat. Biotechnol.* **26**, 417-426 (2008).

140 Hansen, R., Bruus, H., Callisen, T. H. & Hassager, O. Transient convection, diffusion, and adsorption in surface-based biosensors. *Langmuir* **28**, 7557-7563 (2012).

141 Deen, W. M. Analysis of transport phenomena. (1998).

142 Dan, Y. *et al.* Dramatic Reduction of Surface Recombination by in Situ Surface Passivation of Silicon Nanowires. *Nano Lett.* **11**, 2527-2532, doi:10.1021/nl201179n (2011).

143 Demichel, O. *et al.* Surface recombination velocity measurements of efficiently passivated gold-catalyzed silicon nanowires by a new optical method. *Nano Lett.* **10**, 2323-2329 (2010).

144 Grumstrup, E. M. *et al.* Ultrafast carrier dynamics in individual silicon nanowires: Characterization of diameter-dependent carrier lifetime and surface recombination with pump–probe microscopy. *The Journal of Physical Chemistry C* **118**, 8634-8640 (2014).

145 Kato, S., Yamazaki, T., Kurokawa, Y., Miyajima, S. & Konagai, M. Influence of fabrication processes and annealing treatment on the minority carrier lifetime of silicon nanowire films. *Nanoscale research letters* **12**, 242 (2017).